5-2011

Gamma-ray burst populations

Francisco J. Virgili
University of Nevada, Las Vegas

GAMMA-RAY BURST POPULATIONS

by

Francisco Javier Virgili

Bachelor of Science
Michigan State University
2004

Master of Science
University of Nevada, Las Vegas
2007

A dissertation submitted in partial fulfillment
of the requirements for the

Doctor of Philosophy in Astronomy
Department of Physics and Astronomy
College of Science

Graduate College
University of Nevada, Las Vegas
May 2011

UNLV
UNIVERSITY OF NEVADA LAS VEGAS

THE GRADUATE COLLEGE

We recommend the dissertation prepared under our supervision by

Francisco Javier Virgili

entitled

Gamma-ray Burst Populations

be accepted in partial fulfillment of the requirements for the degree of

Doctor of Philosophy in Astronomy

Bing Zhang, Committee Chair

Stephen Lepp, Committee Member

Kentaro Nagamine, Committee Member

Balakrishnan Naduvalath, Graduate Faculty Representative

Ronald Smith, Ph. D., Vice President for Research and Graduate Studies
and Dean of the Graduate College

May 2011

ABSTRACT

Gamma-ray burst populations

by

Francisco Javier Virgili

Dr. Bing Zhang, Examination Committee Chair
Professor of Physics
University of Nevada, Las Vegas

Over the last fifty years the field of gamma-ray bursts has shown incredible growth, but the amassing of data has also left observers and theorists alike wondering about some of the basic questions surrounding these phenomena. Additionally, these events show remarkable individuality and extrema, ranging in redshift throughout the observable universe and over ten orders of magnitude in energy. This work focuses on analyzing groups of bursts that are different from the general trend and trying to understand whether these bursts are from different intrinsic populations and if so, what can be said about their progenitors. This is achieved through numerical Monte Carlo simulations and statistical inference in conjunction with current GRB observations. Chapter 1 gives a general introduction of gamma-ray burst theory and observations in a semi-historical context. Chapter 2 provides an introduction to the theory and practical issues surrounding the numerical simulations and statistics. Chapters 3-5 are each dedicated to a specific problem relating to a different type of GRB population: high-luminosity v. low-luminosity bursts, constraints from high-redshift bursts, and Type I v. Type II bursts. Chapter 6 follows with concluding remarks.

TABLE OF CONTENTS

LIST OF FIGURES

LIST OF TABLES

ACKNOWLEDGMENTS

I would like to thank, first and foremost, my advisor Dr. Bing Zhang for his many years of teaching, encouragement and dedication. Your guidance and support have been invaluable in my formation as a well-rounded scientist and citizen of the world. When it is my turn to pass on my knowledge to the next generation of scientists, I will remember my experiences of friendship and professionalism with you as an example of what to strive for. I would like to also thank Dr. Enwei Liang for innumerable hours of help explaining the theory behind and debugging my earliest codes that served as a foundation for much of my later work.

In addition, I would like to thank the faculty and staff at UNLV, especially the rest of the astronomy faculty, Drs. Proga, Rhee, Lepp, Nagamine, and Smith for their willingness to collaborate and share their expertise both in and out of the classroom. My experiences would not have been the same without my fellow students at UNLV, both past and present. I thank you all for your friendship and support over the past few years.

Last, but by no means least, I would like to acknowledge the continued love and encouragement of my family and friends. Most notably the immeasurable support of my parents and siblings and loving husband (and proofreader) Chip. You are my rock and a continued source of inspiration.

CHAPTER 1

INTRODUCTION

Gamma-ray bursts have had a fascinating story since their humble discovery in the late 1960s. This introduction attempts to gather the many facets of that history in a comprehensive and overarching way, slowly focusing on three questions that are seemingly unrelated but are all connected to gamma-ray burst (GRB) populations and tied together by a similar theory and computational method.

Gamma-ray bursts

Astronomers in all subfields are proponents of touting their newest and most exciting discovery. For many years, that phenomenon has been gamma-ray bursts (GRBs), the "most energetic", "most catastrophic", "cutting edge", "farthest observed" object that astronomy has known to date. This is most clearly noted in the abundance of funding and attention that has been given these objects, especially in the form of space-based missions that capture the public's eye on a level with the beloved and famous Hubble Space Telescope.

GRBs are observed randomly in time and space and span several decades in energy. The prompt emission that gives the phenomenon its name is observed in the gamma-ray band, classically tens of keV to several MeV, but this only scratches the surface. The first GRB detected, 670702 (YYMMDD format), was detected by the United States' VELA satellites, which were placed in orbit to detect covert nuclear testing during the height of the cold war [1]. Shortly after launch, the four spacecraft began detecting gamma-rays that, after deliberation and close study, were determined to be from the direction of space and not originating from the Earth's surface. These first observations, lasting mere seconds, were the first glimpse into the world of GRBs (Figure 1). Since that time, a variety of different missions have been created for their study, each with its own objectives and specialities, spanning a range of a few keV

to several GeV gamma-rays (as compared to the 0.2-1.5 MeV range of VELA). In contrast, the later and longer-lasting afterglow components have been observed from keV to radio, lasting hours to even years after the initial burst of gamma-rays. The observation of this second component did not occur, however, until the late 1990s, leaving nearly two decades for the theory, and a bit of speculation, to grow and mature. On the extremely energetic end of the spectrum, GRBs are theorized to be sources of ultra high-energy gamma-rays and cosmic rays as well as neutrino sources. Air and water Cherenkov (Čerenkov) detectors, such as IceCube [2], VERITAS [3] and the next generation Cherenkov Telescope Array [4], have provided upper limits of detections and can provide a wealth of information on radiation processes and energetics.

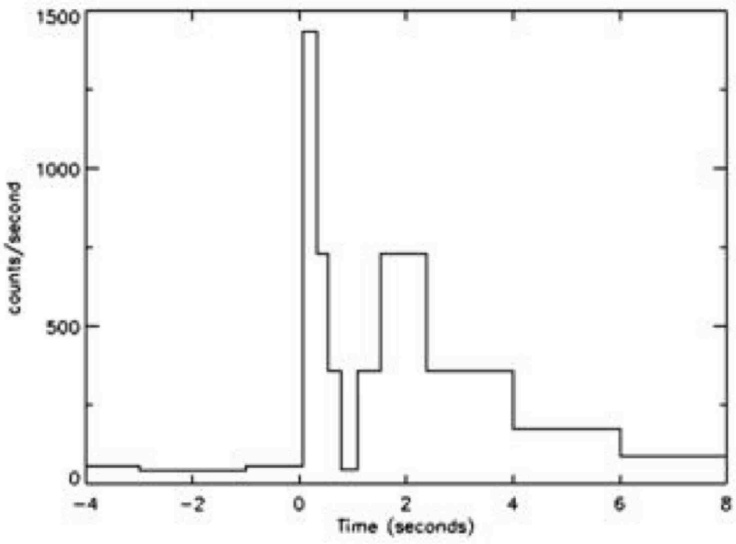

Figure 1 The lightcurve of the first observed gamma-ray burst, GRB 670702. [1]

Temporally, each burst is unique and generally highly variable, with the prompt gamma-rays lasting fractions of a second to hundreds of seconds and having variability timescales on the order of milliseconds. Note that for typical values of flux and distance observed for GRBs, the emitted energy in prompt gamma-rays is on the order

of 10^{52} erg, nearly the sun's entire rest mass energy. The peaks in burst lightcurves are also randomly distributed and of different intensities, likely giving hints to the nature of the central engine and emission properties, although this is still highly debated. Afterglow emission is generally more smooth but also unique to a particular burst. The sample of bursts follow general trends, not all of which can be fit into one comprehensive model.

Despite the paradoxical lack and overabundance of information, where more observations often lead to further questions, there have been advances in both theory and observation that allow us to form a general picture of what we think GRBs are, how they function, and how it is that we come to observe them.

Distance debate and relativity

In the early years of the GRB field, the biggest detriment to the field was the low angular resolution of the available detectors and the inability to do quick follow-up observations in other wavelengths. Regardless, many advances and debates about the underlying theory of GRBs took hold in the time before the launch of the *Compton Gamma-Ray Observatory* (*CGRO*) in 1991 (for a summary see [5]). A plethora of models were created, primarily to address two very important questions: What is the underlying mechanism that produces the observed energetics, and where are GRBs located (in the Galaxy or at cosmological distances)? These questions are obviously coupled, for as an object is placed farther from an observer, the 'inverse square law' of radiation requires that the energy radiated increase to compensate.

Addressing the first question brings to light the concept known as the compactness problem, first outlined in a general way in 1975 [6]. GRBs are observed as bursts of high energy gamma-rays, having equal or greater energy than supernovae, so it is a reasonable assumption that they occur due to a large explosion. A large amount of energy is deposited into a small area, heating and expanding the gas, causing the

radiation we see. Taking a typical flux of $F \sim 10^{-6}$ erg cm^{-2} s^{-1}, the isotropic energy can be approximated as

$$\mathrm{E_{iso}} \sim 4\pi \mathrm{d_L^2 F} \sim 10^{51} \text{ erg s}^{-1} \tag{1.1}$$

where d_L^2 is the luminosity distance and cosmological distances are assumed. This is a valid assumption using current data that the pioneers in the field were not lucky enough to have. Gamma-rays, especially at these energies, are known to create e^+/e^- pairs under certain conditions, based on the rest mass energy of the electron, $m_e c^2$ and the energy and angle of collision of the two gamma-rays (Figure 2). One can estimate the optical depth for the production of pairs from gamma-rays based on the isotropic energy and an estimate of the size of the emission region. As alluded to earlier, the emission size can be estimated through the variability timescale, δt. Information at the source cannot travel faster than light speed; therefore, a typical size can be given by the variability, since this is the timescale of change in the emission properties of the source, multiplied by the speed of light. Estimating the pair production optical depth as

$$\tau_{\gamma\gamma} \sim \sigma_T n l \tag{1.2}$$

with σ_T the Thompson cross-section, n the particle density and l the length scale, combining Equation 1.2 with the energetics information above gives

$$\tau \sim \sigma_T \frac{E_{iso}}{mc^2 (c\delta t)^3} c\delta t \sim 10^{15} \gg 1 \tag{1.3}$$

for cosmological distances. The argument holds, even for much closer distances, where the energy emitted would be on the order of 10^{33}-10^{48} erg for sources in the local neighborhood of stars out to extragalactic distances [6]. Only the closest bursts, with sufficiently low energy to not annihilate the gamma-rays and create pairs, would

be observed. The first sketching of an explosion as an explanation for GRBs was proposed by Cavallo and Rees in 1978 [7]. They discuss a variety of topics, ranging from the escaping of radiation above a photosphere where pairs are no longer created to a variety of radiation mechanisms.

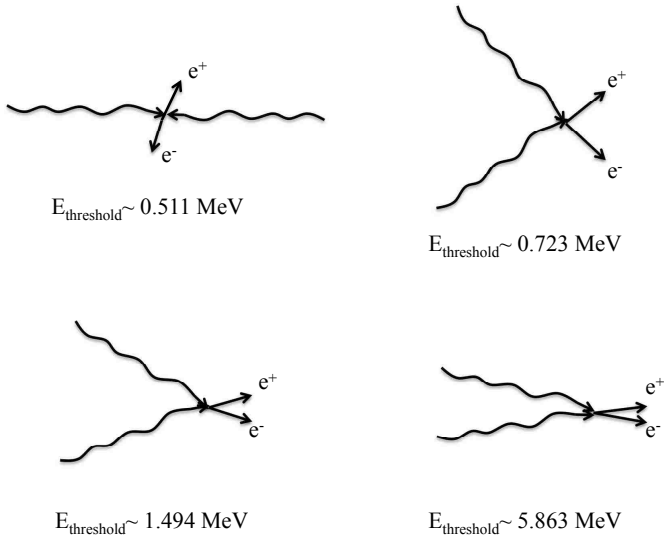

Figure 2 Differences in the threshold energy for creation of an e^+/e^- pair from two gamma-rays with different angles of collision.

The solution to the compactness is both simple and elegant. The introduction of relativistic motion solves a variety of problems caused by the compactness problem. First, the intrinsic length scale becomes constricted in the frame of the the observer by a scaling of the Lorentz factor, Γ, resulting conversely in an increase in the size of the emission region mentioned above. Second, the same process causes an overall drop in the energy of the photons, dropping their potential to breach the limit for pair production and allowing for more photons to escape. Another consequence of the relativistic motion that lowers the amount of pairs produced is the relativistic beaming and the geometry of the system. As demonstrated in Chapter 4 of Rybicki and Lightman [8], the isotropic radiation emitted from a relativistically moving object

is transformed and beamed into the direction of motion (Figure 3). If the gamma rays are moving almost parallel to one another, fewer collisions will result in pairs. These facts, coupled with the newly derived self-similar relativistic blastwave solution [9], were the building blocks of future blastwave models.

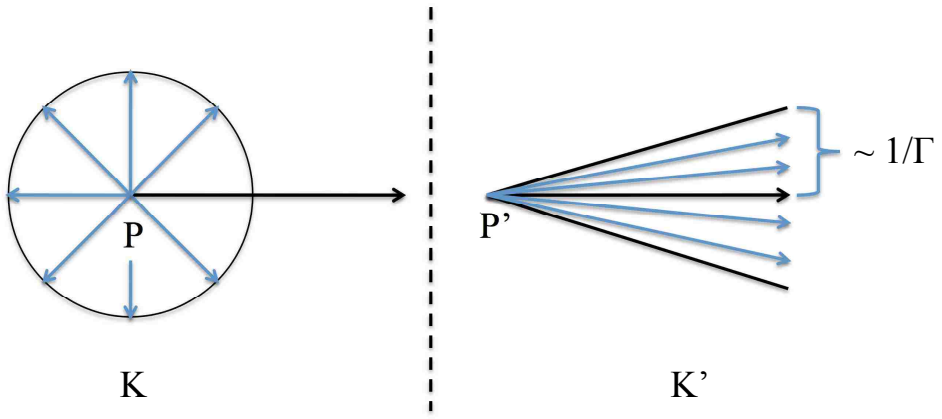

Figure 3 The beaming effect of radiation caused by an object moving at relativistic speeds. On the left, an object at P is stationary and emitting isotropically. On the right, the same object is now moving to the right at relativistic speeds and its emission is now beamed in the direction of motion into a cone with half-opening angle proportional to the inverse of its Lorentz factor, Γ. See [8] for full details and derivation.

Relativistic motion solves the compactness problem yet adds another layer of complexity. It is important to understand the relationship between what occurs at the source and what is seen by the observer, as different times and reference frames affect a variety of facets of the GRB problem. Reference frames are the more straightforward element to identify, being simply the comoving frame and the central engine/observer frame. Comoving denotes motion with the relativistic flow. Note that if the observer is a distance D away from the central engine, there is no Lorentz

transformation between the observer and where the central engine is located, but there is a propagation effect that affects the timescale, as detailed below (Figure 4). Just as with the reference frames, two of the three timescales are readily identified, corresponding to the comoving and source frame transformation. A third effect is a result of the propagation of the radiation from the central engine to the observer. Consider two photons emitted by the central engine at times t_1 and t_2. The time that it takes for the photons to travel from the source to observer is

$$t_{1r} = t_{1e} - D/c \tag{1.4}$$

and

$$t_{2r} = t_{2e} + (D/C - \beta cos\theta(t_{2e} - t_{1e}) \tag{1.5}$$

where 'r' stands for *received at observer* and 'e' for *emitted at source*. The constants β and θ are the dimensionless velocity and angle of emission with respect to the observer. The relationship between the emitted and received timescales is then

$$(t_{1r} - t_{2r}) = (1 - \beta cos\theta)(t_{1e} - t_{2e}). \tag{1.6}$$

Considering that bursts have ultra-relativistic outflows, the coefficient on the right-hand side of the equation can be expanded and is approximately $1/2\Gamma^2$, causing a constriction in the received timescale of the photons. From simple geometric arguments we have added a third timescale, demonstrating the care that must be taken in analyzing GRB data.

Two seminal papers in 1986 were the first to provide a framework for a cosmological GRB model involving a relativistic explosion, hinting at the possibility of compact stellar remnants as the progenitors [10, 11]. Paczyński [10] makes a simple argument for the likely cosmological origin of bursts based on two (non-conclusive

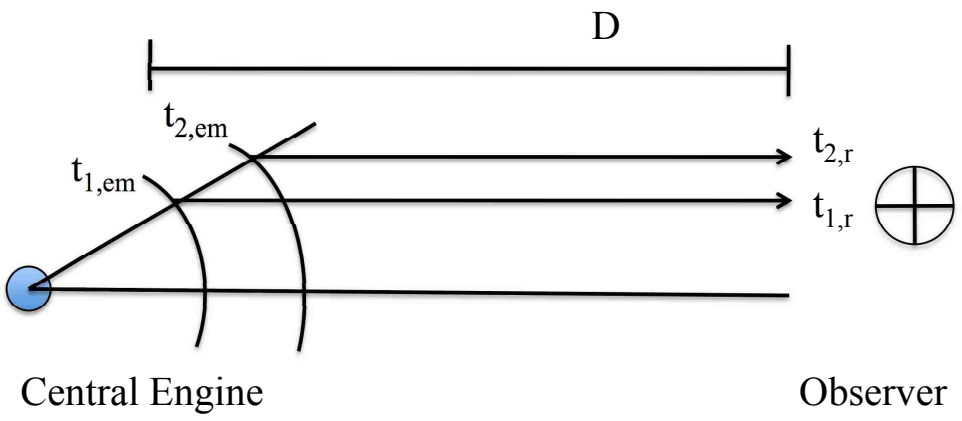

Figure 4 Diagram detailing the geometry of observing an object at a distance D from the observer. Photon 1 and Photon 2 are emitted by material moving a relativistic speeds with respect to the central engine at times $t_{1,em}$ and $t_{2,em}$. The photons are received at the observer at a time $t_{1,r}$ and $t_{2,r}$, at slightly different times. The delay due to propagation from the source to the observer corresponds to a roughly $1/2\Gamma^2$ contraction in observed signal.

but suggestive) coincidences and by calling on the work of van der Bergh [12]: first, an energetics consideration as in Equation 1.1, and secondly that the roughly 10^{51} erg s^{-1} of energy emitted would, at a moderate redshift, peak in the few MeV range, consistent with the observations at the time. Both of these references analyze the effects of a large amount of energy deposited in a small area and the ensuing relativistic expansion and photospheric radiation associated with the (non-baryonic) explosion once the expansion becomes optically thin to radiation.

Shocks and progenitors

In the next phase of the GRB story, the idea of shocks was presented to explain the mechanism for accelerating particles that then cool and radiate, and work continued on the theories of possible progenitors. Many of the ideas from this time carry

through to today, establishing the basis of the modern theory of GRBs. Contextually, this is also the time of the launch of the *Compton Gamma-Ray Observatory* (*CGRO*) with its famous instruments the "Burst And Transient Source Experiment" (BATSE) and the "Energetic Gamma-Ray Experiment Telescope" (EGRET). This mission would reinvent the field, observing over 2700 bursts in its nearly 10 years of operation. Although occurring much later, the implementation of the *Swift* [13] and *Fermi Gamma-ray Observatory* [14] telescopes are of importance to the following discussion. The work presented here is generally based on the *Swift* sample, but advances and breakthroughs from both missions will be routinely used to highlight important points in the development of both the theory and simulations presented below and in subsequent chapters.

Rees and Mészáros [15] and Mészáros and Rees [16] speculated on the energetics of a GRB fireball that would expand, with some baryons and perhaps collimation, and later interact with the interstellar medium (ISM) to produce shocks and external emission. In the simplest of cases, we can consider a shock created by a one-dimensional planar fluid colliding with a second fluid. When a gas expands into a medium faster than the local sound speed, c_s, a shock is formed (see [17]). Alternatively, we can consider the case where we transform the reference point and consider how the medium moves with respect to the shock, conveniently separating the shock region into four sections (see Fig 5). In the upstream section, a forward shock propagates into the ISM, creating a region of un-shocked (Region 1) and shocked ISM (Region 2). Similarly, in the downstream direction, a reverse shock propagates into the shell material, creating similar shocked and un-shocked regions of shell material (Regions 3 and 4). Using the conditions for conservation of mass, energy and momentum flux, all of which must be conserved across the shock, one can derive a set of shock jump conditions. These can be further simplified by considering 'strong' shocks created by materials moving at very high speeds. The conservation equations boil down to the

following relations:

$$\frac{n_2}{n_1} \simeq 4\gamma_{21} + 3 \simeq 4\gamma_{21} \tag{1.7}$$

$$\frac{e_2}{n_2} \simeq \gamma_{21} m_p c^2 \tag{1.8}$$

$$e_2 \simeq 4\gamma_{21} n_1 m_p c^2 \tag{1.9}$$

$$P \sim \frac{1}{3} e \tag{1.10}$$

where n is the number density, e the energy density, and γ the relative Lorentz factor with the subscripts designating the region. This discussion is, of course, only for a one-dimensional planar flow. A full solution of the relativistic spherical solution can be found in Blandford and McKee [9].

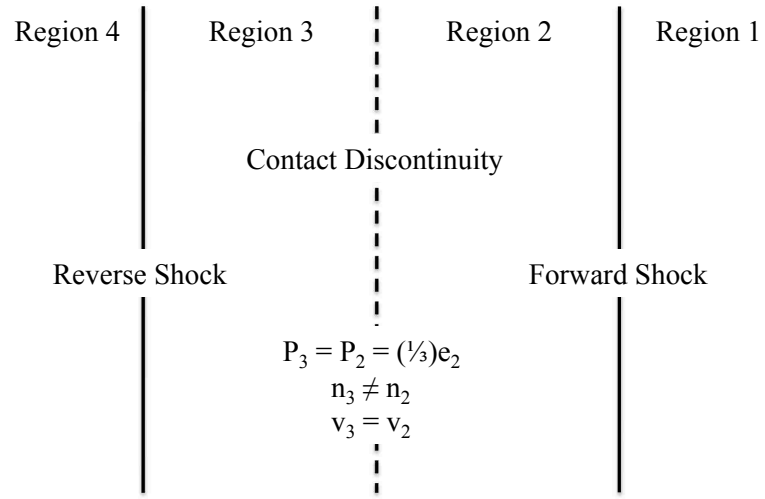

Figure 5 Different regions of a strong shock. Region 1: Un-shocked medium Region 2: Shocked medium Region 3: Shocked shell material Region 3: Un-shocked shell material.

Within the paradigm of the shock scenario, it is possible to accelerate particles to very high energies, essentially converting the kinetic energy in the flow into heat and radiation. Achterberg *et al.* [18] detail the process of diffuse shock acceleration, or first order Fermi acceleration, where magnetic fluctuations in the shock region confine baryons near the shock and cause them to gain energy, as proposed by Blandford and Eichler [19]. In the case of ultra-relativistic shocks, electrons can gain energy on the order of Γ^2 during the first crossing of the shock, while further crossings are on the order of unity. A secondary consequence of this model, which is useful when considering radiation mechanisms, is that it accelerates particles in a power-law hierarchy, naturally producing a spectrum of the form $N(E) \propto E^{-s}$. Alternative models for the acceleration of particles include magnetic reconnection and turbulence (known as the Internal Collision-induced MAgnetic Reconnection and Turbulence (ICMART) model [20]) and Poinyting flux acceleration [21], which apply for magnetically dominated flows.

Before introducing the progenitor models proposed in this time period, it is important to understand the context of the observations of GRBs at this time. *CGRO*/BATSE had been operational for two to three years, collecting roughly 100 bursts a year. As early as 1992, BATSE showed a nearly isotropic distribution of GRBs in the sky ([22]; see Figure 6) adding strong evidence supporting their cosmological origin. The distance debate was not fully put to rest until 1997 when the Italian-Dutch satellite *Beppo-SAX* [23] produced the first x-ray images of a GRB afterglow [24] that led to subsequent optical detections [25, 26] and host galaxy identification and redshift determination ([27, 28], etc.). The progenitor models presented below reflect these observations and are generally framed in a cosmological mindset amidst various debates (e.g. [29, 30]).

Simultaneous to the advances in understanding the nature of the acceleration mechanism and shocks in GRB ejecta as well as the revolutionary data collected by

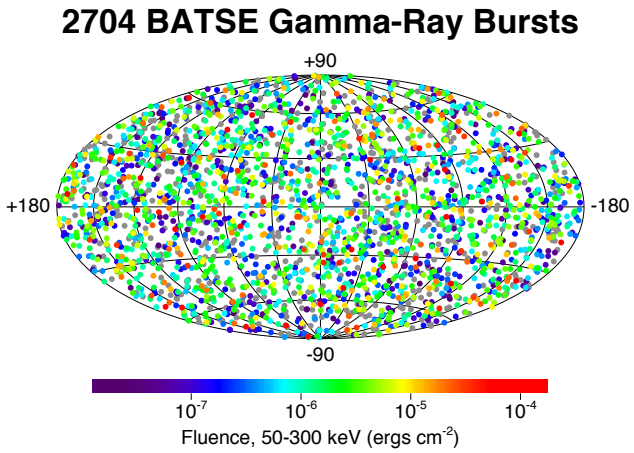

Figure 6 All-sky map detailing the positions of 2704 BATSE GRBs. This result, which shows an isotropic distribution on the sky, was crucial evidence in support of the cosmological scenario for GRBs. [31]

BATSE, various models were further developed or proposed for the progenitor that provides the driving force behind the burst. The first, which has ties to earlier works ([10, 11]), was advances in compact object merger models, more specifically neutron star-neutron star (NS-NS) mergers [32, 33]. Both studies argue for a scenario where such a merger would produce the correct energetics and source size for a fireball that would produce gamma-rays on the order of what was observed of GRBs to date. Such a coalescence should produce on the order of 10^{54} erg of released gravitation energy, which is sufficient to provide a small fraction to power the GRB. In the 'standard' merger model, the product of the merger is a black hole-accretion disk system, similar to the central-engine produced by stellar collapse. The only difference between the events would then be the accretion timescale. Merger events should have a smaller amount of material in which to create their disks, since there is no material from a massive star just $\sim 3M_{\odot}$ of TOTAL material in the system. This corresponds to about a fraction of a solar mass of material left for the accretion disk that can be accreted on a timescale of the order of 0.1 s or less. This timescale, however,

is much too short to explain the observations of bursts and may be an indication that this model may need some revision. Massive stellar collapse accretion disks have more material, which is one reason this model is called on to explain long-soft GRBs. The similarities in the central engine, however, predict similar afterglow properties as confirmed by observation [161]. Another important prediction relates to the ability to possibly observe a gravitation wave signature [34]. Observations of such a signal would be very strong evidence in support of compact object mergers as progenitors of GRBs.

The second model for the possible progenitor was a millisecond magnetar, or a rapidly spinning NS with surface magnetic field of roughly 10^{15} G [35, 36]. In this model, a very highly magnetized NS is created from, for example, an accreting WD binary system with abnormally high magnetic fields. The newly created NS then loses its rotational energy very quickly, creating an electric field from the rotating magnetic fields and producing pairs in an optically thick plasma. This plasma, in turn, powers the radiation seen as a gamma-ray burst.

The last model proposed was a 'failed supernova' model, generally known as the 'collapsar' model [37]. In this model, a massive star collapses and creates a BH-accretion disk system, similar to that of the merger model, which then creates a jet of relativistically accelerated particles. Together with 'internal and external shocks' [15, 38, 39] and/or 'internal' energy dissipation from magnetics fields [40], these models are the building blocks for the modern theory of GRBs. Each of these components naturally has its flaws but we can nonetheless obtain a general picture of what happens behind the scenes of GRBs.

Internal and external shock model

The internal shock model is considered the standard model for explaining GRBs. It contains a series of assumptions, some of which satisfy observations, and was the

first comprehensive approach to address the (still) poorly understood process(es) that produce the observed prompt and afterglow emission. It should be noted that, historically, afterglow emission was not yet observed when this theory was formally published in the early 1990s [42, 43] due to the inability to rapidly and accurately locate bursts and perform follow-up observations. The internal/external shock model does not attempt to explain the nature of the progenitor that powers GRBs, other than the basic fact that it deposits a large amount of energy, but rather aims to create a theory that explains how the radiation we see is created. It also aims to solve the problem of the most basic fireball model in which a fireball with a small amount of baryons expanding in a medium deposits most of its energy into the kinetic energy of the baryons and not into radiation. This will cause the fireball to not radiate efficiently and have a quasi-thermal spectrum as opposed to the power-law that is observed [44].

There are six basic assumptions in the internal shock model that should be kept in mind and which will be addressed in the discussion of the framework of the internal/external shock model below: (i) isotropic emission, (ii) impulsive energy injection, (iii) constant density medium, (iv) synchrotron radiation, (v) relativistic expansion, and (vi) time-independent shock acceleration parameters (e.g. p, ϵ_e and ϵ_B).

The basic dynamics of a GRB fireball occur in two parts. First, energy is deposited by a generic progenitor quickly and intermittently creating a series of shells of ejecta that expand ultra-relativistically into the ISM from the initially large radiation pressure. Assuming the source has a constant luminosity L for a time t, the fireball radius is now $r = ct \simeq 3 \times 10^{10}$cm. The Lorentz factor ($\Gamma$) initially increases linearly with radius until it reaches a constant factor Γ_0, which it will maintain until the fireball begins to decelerate [45, 46, 47]. At some point during the expansion, the fireball will be sufficiently large (therefore the photon density will drop sufficiently) for the fireball to become optically thin to pair production and Compton scattering. This is the pho-

tosphere and the first observable signal of a GRB (discounting gravitational waves or neutrinos which have yet to be observed) and the origin of the prompt emission in the most simplistic of models [10, 11, 48, 49]. The emission created by the photosphere would originate from the base of the flow where the opacity is high and thermal equilibrium can be approximated [49]. It is still unclear whether photospheric emission can be called to explain all the emission from GRBs, but a variety of recent works have detailed both sides argument. Emission from GRB 090902B shows a signature that is often attributed to a thermal component [50, 51] while some works are confident in using the thermal model to explain high energy emission. [49, 52, 53, 54, 55]. Other observations, such as those of GRB 080916C show clear non-thermal spectra for multiple order of magnitude, ruling out photospheric emission for that burst [56].

One can also imagine that at later times during the expansion, beyond the photosphere radius, material with a slightly faster Lorentz factor can overtake slower material, creating shocks that dissipate the relative kinetic energy of the shells and accelerate baryons, which then cool radiatively by synchrotron emission or other cooling processes. These 'internal' shocks produce the prompt gamma-ray emission [38] and provide a plausible solution to the millisecond or shorter variability [57]. These type of interactions, however, are likely to have a small efficiency of conversion from kinetic energy of the shell to acceleration of the particles, generally on the order of 5-10% [58, 59]. Nonetheless, this is the primary mechanism called on to explain the prompt gamma-ray emission, as it provides a mechanism to produce rapid variability in the lightcurve and non-thermal emission. Shells of this type can be created if the central engine has intermittent ejections of material caused by, for example, unsteady accretion onto a black hole.

The next phase of the theory of the GRB mechanism is the interaction of the leading shell of material, or the blastwave, with the surrounding interstellar medium (ISM). The blastwave, consisting of the ejecta from the central engine, continues

to expand into the ISM creating an 'external' shock while simultaneously collecting material causing it to slow down and eventually dissipate. This contributes to the multi-band afterglow emission [41, 42, 60]. This emission was theorized in x-ray through radio bands [61, 62, 42] and believed to have a power-law decay under the assumption of synchrotron emission. As mentioned above, afterglow emission was confirmed by observations in 1997 [25, 63] and is still being extensively studied.

Afterglow emission is based on how the fireball evolves and radiates with synchrotron emission [64, 65]. There are two basic scenarios for the evolution of the fireball: whether the fireball expands adiabatically with negligible cooling due to radiation (energy conservation) or whether it cools as it expands (momentum conservation). These cases are known as slow- and fast-cooling, respectively. In the adiabatic approximation, the dynamical timescale is shorter than the cooling timescale and the energy can be approximated as the energy contained in the accelerated baryons

$$E \sim R^3 n m_p c^2 \Gamma^2 \sim \text{constant} \tag{1.11}$$

where Γ is the bulk Lorentz factor of the shell and R the radius from the central engine. This can quickly be rearranged to show that Γ evolves as $R^{-3/2}$. Assuming relativistic motion and impulsive energy injection, the length scale can be approximated as ct, implying a dependence of Γ with *emission* time as $\Gamma \sim t_{em}^{-3/2}$. Utilizing the conversion from emitted time to observed time, $t_{em} = \Gamma^2 t_{obs}$, gives a dependence scaling as $t_{obs}^{-3/8}$. The derivation of the radius evolution can be achieved in much the same way, only assuming that the radius evolves as the emission time, giving $R \propto t_{obs}^{-1/4}$.

In the fast cooling case, a large fraction of energy is given to the electrons in the ejecta and these quickly radiate and conserve the momentum of the system. Since the momentum is proportional to $nR^3\Gamma^2$, it is possible to derive the dependencies of

the bulk Lorentz factor and radius with time:

$$\Gamma \propto R^{-3} \propto t^{-3/7}; R \propto t^{1/7}. \tag{1.12}$$

Tied into the evolution of the fireball is the assumption of synchrotron emission. Following from the discussion on particle acceleration mechanisms in the ejecta, electrons are assumed to be distributed as a power law in energy

$$N(E)dE = CE^{-p}dE \text{ or } \mathrm{N}(\gamma)\mathrm{d}\gamma = \gamma^{-\mathrm{p}}\mathrm{d}\gamma \tag{1.13}$$

where C is a constant and γ the electron Lorentz factor. The latter should not be confused with the bulk Lorentz factor of the flow, Γ. With this distribution, it is possible to calculate the total power emitted by synchrotron radiation by integrating the spectrum and power over all possible energies, or Lorentz factors, in order to find the dependencies on the frequency, ω (see [8] for a full derivation):

$$P_{total}(\omega) = C \int_{\gamma_m}^{\gamma_M} P(\omega, \gamma)\gamma^{-p}d\gamma \tag{1.14}$$

The total power and typical emission frequency for synchrotron radiation [8] are given as

$$P = (4/3)\sigma_T c\gamma_e^2(B^2/8\pi) \tag{1.15}$$

$$\nu = \Gamma\gamma_e \frac{eB}{2\pi m_e c} \tag{1.16}$$

where σ_T is the Thomson cross-section. Together, this leads to the theoretical synchrotron spectrum where the power increases as $\nu^{1/3}$, peaks, then decays as $\nu^{-(p-1)/2}$. Other effects that come into play are synchrotron self-absorption and cooling effects. Since the power of emission is dependent on γ_e^2, the highest energy electrons will cool very efficiently and quickly, as the cooling timescale depends on γ_e^{-1}. Once cooled,

these electrons will stop radiating and cause a steepening in the spectrum beyond a typical cooling frequency, ν_c. At low ($\sim$ radio) frequencies, absorption becomes important and the source becomes optically thick to synchrotron emission, causing a rising slope in the spectrum below a critical self-absorption frequency ν_a. Furthermore, the placement of the minimum electron frequency ν_m and the cooling frequency ν_c can create different spectra. The differences between slow-cooing ($\nu_m < \nu_c$) and fast-cooling ($\nu_c < \nu_m$) spectra and a comprehensive study of the expected synchrotron slopes is found in Sari *et al.* ([43]; see Figure 7). Furthermore, this type of analysis can be applied to many different scenarios, including those where the external medium is not homogenous (e.g. it is part of a wind profile [66, 67, 68] remaining from a massive star progenitor) or arises from collimated jet emission [69, 70]. A list of theorized spectral and temporal slopes for various models can be found in [71].

A variety of observations, unfortunately, disrupt the eloquent picture of synchrotron radiation as the sole radiation mechanism powering the afterglow emission. Below the peak energy, theory requires that the photon index, α, equal -1.5, since the synchrotron cooling timescale is often shorter than the dynamical timescale. Observations, however, show that this slope is closer to $\alpha \sim -1$. Enhancements to the theory, such as particle re-acceleration, adiabatic losses or rapidly varying magnetic fields have been ruled out as possible solutions to the problem [72]. Similar to the previous argument, synchrotron radiation only allows for photon indices that are softer than $\alpha = -2.5$, while observations show some bursts with harder indices [73]. Compton upscattering of low-energy photons and synchrotron self-absorption are two methods to change the model that may potentially solve this problem; however, the former would imply intrinsic differences in bursts that violate the hardness limit, and the latter could inhibit the observed radiation due to very high photon densities [73]. Other possible solutions include introducing a component from the thermal photosphere emission [48] or so-called 'jitter' radiation [74], which is radiation emitted by

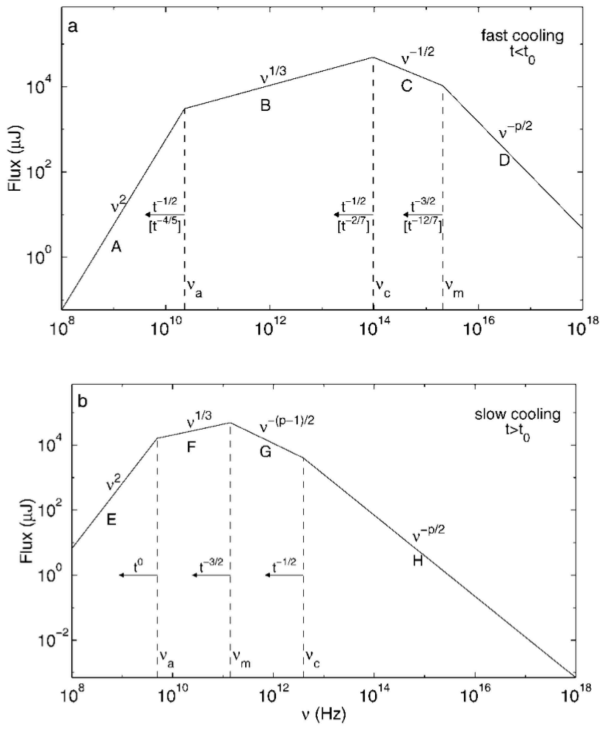

Figure 7 Theoretical synchrotron spectra based on the external shock model, showing indices and time dependencies for both fast-cooling (radiative fireball) and slow-cooling (adiabatic fireball) cases. [43]

relativistic electrons in random small-scale magnetic fields. Lastly, the observed values of the peak spectral energy, E_p, are much larger than expected, requiring that the internal shocks accelerate only a small fraction of particles [75, 76]. This problem can be solved by a highly magnetized flow [20].

If, then, one is to believe that synchrotron emission is inadequate to explain the available data, alternative radiation mechanisms must be provided. Other mechanism that naturally arise when electrons are accelerated relativistically are processes involving Compton scattering, i.e. inverse Compton scattering (ICS) and synchrotron self-Compton (SSC). Compton scattering is the process by which an electron, initially at rest, gains energy from an interaction with a highly energetic photon, namely $h\nu \geq mc^2$. ICS is the same process but occurring in the opposite direction: A highly

energetic electron interacts with a seed photon of lower energy, causing the seed photon to be upscattered [8]. The expression for the radiation power of ICS is similar to that of synchrotron radiation, simply a substitution of the photon density, U_{ph}, for the magnetic density in Equation 1.15:

$$P = (4/3)\sigma_T c \gamma_e^2 (U_{ph}^2/8\pi). \tag{1.17}$$

A natural source of seed photons for ICS in GRBs is thermal photons created from the photosphere emission [40, 49, 53]. Most models, however, have difficulty in explaining the harder-than-expected low energy photon spectral indices of many observed GRBs. Alternatively, one can imagine a scenario where highly relativistic electrons in an ordered magnetic field begin to cool via synchrotron radiation emitting photons that act as seeds for ICS. This process is known as synchrotron self-Compton (SSC). It produces a composite spectrum consisting of a classical synchrotron spectrum with with an IC bump at higher energies (assuming a power law distribution of electrons). This mechanism can be applied to GRBs if the synchrotron emission peaks at lower frequencies (x-ray and longer) so those seed photons can then be up-scattered to produce the observed gamma-ray emission [77]. Observations such as those associated with GRB 080319B (the 'naked-eye' GRB) [78] are the type of evidence needed to promote this model, although they suffer certain pitfalls when looking at the variability and lag of the gamma-ray and prompt optical emission [79] and energetics [80, 81, 82].

Constraints to the gamma-ray burst model

As the theory of GRBs was starting to take form, observations were steadily increasing and allowing for more complete observational tests. This is markedly seen in the large quantity of quality data from both *Swift* and *Fermi*, as mentioned previously. Next, I briefly address the confirmations and questions that have arisen

from afterglow observations.

X-ray emission

Although each GRB has a unique temporal and spectral profile, general trends can be identified in the form of the afterglows now that a sufficiently large sample has been accumulated. *Swift* observes roughly 100 GRBs per year, oftentimes capturing the earliest onset of x-ray emission. The observed 'cannonical' x-ray lightcurve consists of five parts, not all of which are observed in all bursts [83, 100, 84, 85] (Figure 8), lasting many orders of magnitude in time after the prompt emission. Some of the observations fit well into the internal/external shock models, and others are more perplexing. The two components that are easiest to explain are the 'normal' and 'post-jet break' slopes. The temporal slopes of these segments are of order -1 and -2, respectively, and fit well into the predictions of the synchrotron emission expected from the fireball shock model [42, 43, 66].

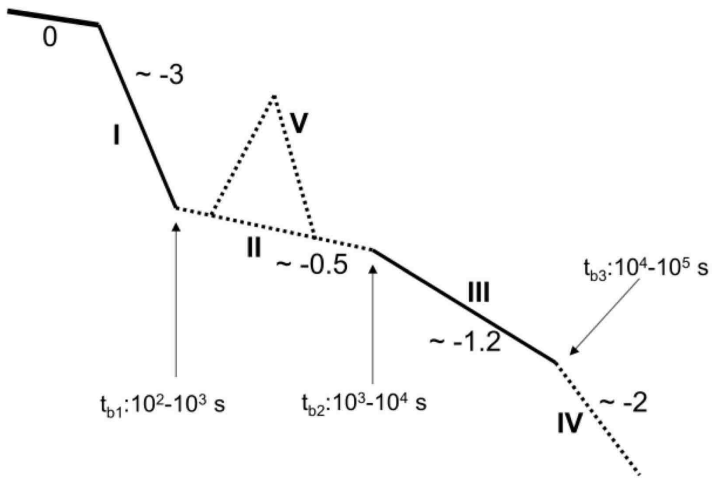

Figure 8 Details of the canonical x-ray afterglow: (0) End of the prompt emission (I) Steep decay (II) Shallow decay (III) Normal decay (IV) Post-jet break decay (V) X-ray flares. [100]

The post-break slope, however, brings to light the need to modify one of the assumptions of the original model, exemplified by breaks in some GRB afterglows [86, 87]. If the GRB emission is not isotropic but rather collimated into a jet, there are two characteristic angles that come into play: first, the constant physical half-opening angle of the jet, θ_j, and secondly, the angle of collimation of radiation from the relativistic transformation arising from the relativistic motion of the electrons that are radiating in the ejecta. The latter scales as $1/\Gamma$, the bulk Lorentz factor of the flow. As the GRB evolves, the initially very small beaming angle of the flow ($\Gamma \gtrsim 10^2 - 10^3$) begins to grow as Γ decreases, until it becomes comparable to the size of the opening angle of the jet. Beyond that size, the emission from the GRB drops very quickly, which can be translated into a steepening of the lightcurve [87, 88]. It is not unrealistic to believe that GRBs might be collimated, as are many astrophysical systems, especially those arising from processes related to the inflow of material, create jets on a variety of scales, from active galactic nuclei to planet formation. Jet production also affects the energy budget required for GRBs [71]. The beaming-corrected energy emitted by a GRB would be

$$2E_{iso}\Delta\Omega/4\pi \;=\; 2E_{iso}\frac{1-cos(\theta_j)}{2} \simeq E_{iso}\frac{\theta_j^2}{2} \tag{1.18}$$

where E_{iso} is the isotropic equivalent energy and $\Delta\Omega$ the solid angle of the emission. This significantly lowers the radiated energy to the order of 10^{50-51} ergs, as calculated from achromatic breaks in radio afterglow observations [89]. Since the underlying cause of this break is structural in nature, it is expected the break should happen achromatically, or at the same time in all bands [90, 103]. There is some evidence of this, but a complex picture of breaks and lacks thereof [92, 93, 94, 95, 96] make it difficult to pin down the ultimate cause [93]. It has also been proposed that the jets themselves might have internal structure that might further change the emission

when seen from different viewing angles [97, 98] or even have a dual-jet structure that can be used to interpret certain observations [78].

The first two segments in Figure 8 are known as the 'steep' and 'shallow' decay, respectively. The steep decay happens at roughly 100-1000 seconds after the burst trigger [99] and is named after its decay index of roughly 3-5 [99, 83, 100] that smoothly connects to the extrapolation of the prompt gamma-ray emission in the x-ray band [101, 84, 102]. The time-averaged spectral index of the steep decay phase generally differs from that of later spectra [100, 103], and in about one-third of bursts, there is evidence for strong spectral evolution within the phase [104, 105, 106]. This evidence points toward the origin of the steep decay phase as the tail end of the prompt emission. The 'curvature effect' is the effect of photons from higher latitudes compared to the line-of-sight arriving at the observer later than those lying closer to the line-of-sight [108, 109, 110, 111, 112] and is often quoted as a solution to this problem [100, 102, 113, 114, 107] and . This model has been successful in explaining the above observations in various bursts, most notably those with spectral evolution [107].

The next phase is the shallow decay phase. This segment fits well into the scenario of the of internal/external shock model under the assumption of continuous energy injection from the central engine. Without the existence of achromatic (i.e. hydrodynamical) breaks in the afterglow [90, 103] that are expected in events such as jet breaks and the lack of spectral evolution [91], the existence of plateaus point to long-lasting central engine activity [115, 116, 117, 118]. This activity is also used to interpret the last component of the x-ray afterglow: flares [119, 100, 120, 121, 122]. Roughly half of *Swift* GRBs have sharply rising and decaying flares throughout the x-ray afterglow, including at very late times [119, 123, 124] and are very difficult to explain with external shocks [125].

Optical and radio emission

Optical observations of GRBs are generally of two types: space-based observations of the prompt gamma-ray event (e.g. with *Swift* UVOT) and ground-based observations, either robotic or late-time follow-up. *Swift*'s advantage of fast slewing and localizing of events has led to many breakthroughs in optical bands to help explain the actual event as well as probing the circumburst medium and environment, host galaxies, redshifts, and many other important pieces of the complete GRB puzzle.

Optical afterglows are observed in roughly 50% of GRBs, which is surprising considering the rapid localizations of many bursts. This band is sensitive to dust extinction in the circumburst medium as well as attenuation from the host galaxy or intervening material. Substantial work has been done in calculating column densities for GRB sightlines as well as in theorizing on mechanisms for producing or explaining 'dark' bursts [126, 127]. Nonetheless, a general picture can be put together of what causes the emission that is seen. Zhang *et al.* [128] proposed a model that is a superposition of the expected t^{-1} decay of the external shock model and the complicated emission from the reverse shock (See Figure 9). This line of thinking ties in heavily to the composition of the flow. For synchrotron radiation to be plausible as a cooling mechanism, large-scale ordered magnetic fields must be present. The strength of the magnetic field affects the power of the synchrotron emission and the strength of the reverse shock emission as it propagates through the un-shocked shell emission. A balance must be achieved between the energy that is deposited in the magnetic field and that which is deposited in the baryon content of the flow, generally prescribed by the parameter $\sigma = \epsilon_B/\epsilon_{baryon} = B^2/4\pi\Gamma\rho c^2$. The largest signature of σ on the prompt emission is in the reverse shock emission seen in optical bands [128, 64, 41]. Both a highly magnetized ($\sigma > 1$) and weakly magnetized flow (low σ, e.g. $\sim 0.01 - 0.1$) will suppress the reverse shock emission. In the first case, the high magnetic field strength will partially balance the pressure from the forward shock, weakening the

reverse shock. In the second case, a very weak magnetic field will suppress the synchrotron emission since the power of the emission depends on U_B^2. Only a moderate σ will produce significant prompt optical emission [128]. Furthermore, as recent studies show, the ejecta might be completely dominated by magnetic fields with negligible baryon content, although this is difficult to determine. Other measures that would help in determining the composition of the flow would be polarization measurements from ordered magnetic fields predicted by a magnetized flow [130, 131, 132, 133]. Measurements of the polarization in GRBs has been done, although the results remain inconclusive [134, 135, 136]. Recent observations of GRB 080916C by the *Fermi* satellite might be another indication of the jet composition. It has been shown that the spectrum of that burst is largely a featureless Band function that would be very difficult to reproduce with the classical internal shock model, which predicts bright photosphere emission [137, 138].

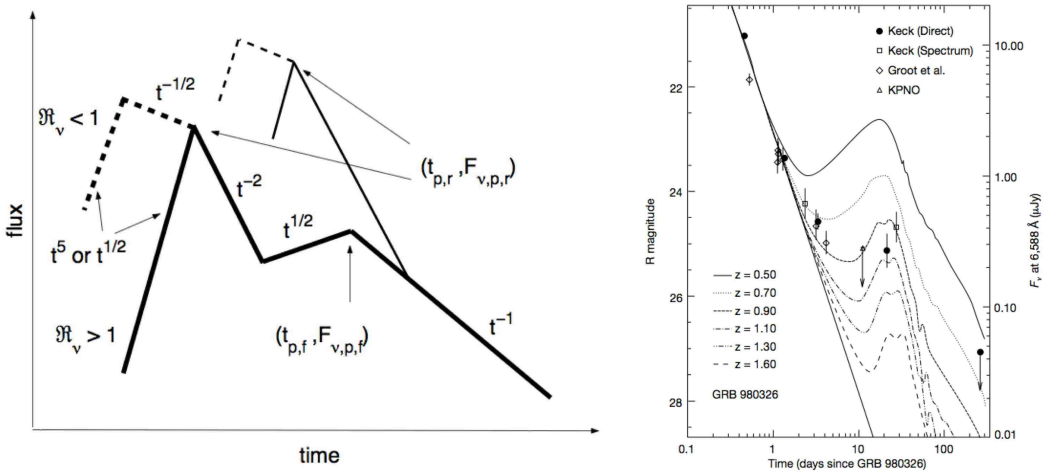

Figure 9 Left: Theoretical optical GRB afterglow [128]. Right: Observations of a late-time SN bump in the optical afterglow of GRB 980326. Superimposed are lightcurves of SN 1998bw as they would appear at various redshifts. [129]

Other landmark optical observations, apart from redshift determinations from host galaxy identifications, are the late-time observations of optical afterglows that

are the foundation of the GRB-supernova (SN) connection. If GRBs are products of the deaths of massive stars, it would be logical to expect a signature similar to a typical Type Ib-c supernova. In the observations of several bursts (most notably SN1998bw-GRB 980425 [139, 140]) a slight re-brightening and deviation of the power-law decay of the optical afterglow is seen roughly one to two weeks after the burst trigger (see Figure 9). This bump is attributed to the non-relativistic emission from a core-collapse supernova [139, 141] and has been shown to fit well in a handful of available bursts [142]. These observations are an extremely important criterion in identifying the types of progenitors that produce GRBs and will be revisited in more detail in the following sections.

Afterglow emission was also predicted in even longer wavelengths, theorized as being visible up to years after the prompt emission and provide further testing to the afterglow emission model (e.g. [61, 62]). Observations of radio afterglows were first seen in the follow up of various bursts in 1997 [24, 143, 26] and have led to the confirmation of relativistic expansion in GRB outflows from scintillation and very-long baseline interferometry (VLBI) [144, 145]. Other important confirmations deduced from radio observations are clues to the energetics of the blastwave [146, 147, 148, 149, 150, 151], especially constraints to the transition between a relativistic and newtonian blastwave as dictated by the afterglow external-shock model. Clues about collimation can also be deduced and the presence of breaks in the lightcurve and can be added to observations in harder bands to provide insight into the presence and structure of GRB jets [152, 144]. Recent works are also attempting to use radio signatures to find of GRB remnants without the aid of a gamma-ray trigger and further the understanding of the GRB-SN connection by comparing SN that seem to be powered by an 'engine' similar to GRBs and those that behave more like 'classical' SN [153]. Radio afterglows are an important piece to the GRB puzzle and a confirmation of the broad characteristics of the external-shock model. Further observations with next-

generation radio facilities will likely provide new and exciting constraints and a wealth of information on GRB energetics and environments.

CHAPTER 2

POPULATIONS AND METHODOLOGY

Overall, the breadth and magnitude of GRB observations have been remarkable but have also led to a slew of questions regarding differences between extreme or outlier events. This work is dedicated to studying three notable problems in GRBs by utilizing Monte Carlo simulations and statistical inference. Below, I briefly introduce each problem individually, leaving further context for subsequent chapters, followed by the general theoretical considerations, simulation details and statistical tests.

- High-luminosity v. low-luminosity

  The motivation for this work stems from observations of intrinsically under-luminous and low-redshift bursts that were observed in the era of *BeppoSAX* and *Swift*, GRBs 980425 and 060218. These bursts are very different when compared to the median redshift and luminosity of $< z > \sim 1 - 2$ and $< L > \sim 10^{51}$ erg s^{-1}, with (z, L) of $(0.0085, 4.7 \times 10^{46}$ erg s$^{-1})$ and $(0.033, 6.03 \times 10^{46}$ erg s$^{-1})$, respectively. Within the context of the luminosity, redshift and peak flux distribution, can these bursts be explained by an extrapolation of the luminosity function of 'classical' core-collapse GRBs?

- High-redshift

  Recent observations, most importantly optical follow-ups of *Swift* triggers, have led to an extraordinary number of GRBs detected at high-redshift. Three record high-z events have truly led the way in exploring the early universe, GRBs 050904 ($z = 6.3$ [154, 155, 156, 149]), 080913 ($z = 6.7$,[157]) and 090423 ($z = 8.2$,[158, 159]). How do these new observations affect the hypothesized rate of GRBs, and how do they compare to models of the star-formation history? What constraints can provide for the luminosity function by including these events?

- Type I v. Type II

  This now controversial issue had its beginning in the BATSE era with the seminal paper by Kouveliotou *et al.* [160] discussing the bimodal distribution of BATSE bursts when plotted in spectral hardness and duration (T_{90}; see Figure 10). It was theorized that short-hard bursts, having no lengthy emission, would be good candidates for the cleaner and smaller energy budget of compact object merger progenitors (e.g. NS-NS; [161]). Afterglow observations, in particular supernovae associations, seemed to cement the theory of massive star progenitors for long-soft bursts and mergers for short-hard. A variety of *Swift* observations, including the advent of a seemingly short burst spike followed by a long tail of soft emission complicated the clean solution to the progenitor problem. Zhang *et al.* [162, 163, 164] proposed a more in-depth classification scheme based on multiple observed properties of observed bursts, where Type I and Type II bursts are related to compact objects and massive stars, respectively. Is the compact star merger model consistent with the observations of short-hard GRBs? What are the implications for the progenitor?

With these questions in mind, I have developed a Monte Carlo code that creates a sample of simulated bursts that mimic *Swift* observations in order to test the consistency between the observed redshift, luminosity and peak flux samples from BATSE and *Swift*. The code has been developed and improved over time and modified for the goal and assumptions of each work.

The number of observed GRBs that will occur at a redshift $z \sim z + dz$ and $L \sim L + dL$ is proportional to the GRB rate, R_{GRB}, luminosity function $\Phi(L)$ and the comoving volume element, dV/dz:

$$\frac{dN}{dtdzdL} = \frac{R_{GRB}(z)}{1+z}\frac{dV(z)}{dz}\Phi(L). \tag{2.1}$$

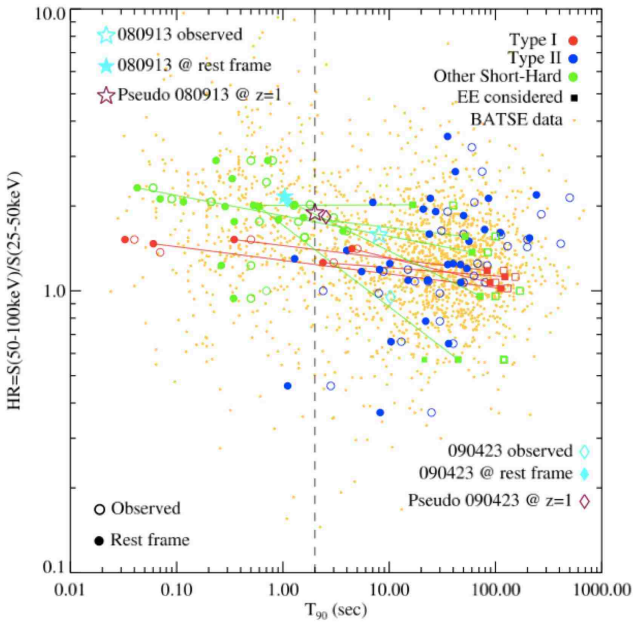

Figure 10 The relationship between the hardness ratio (in two BATSE energy channels) and T_{90} duration of BATSE (green) and some *Swift* and *HETE* bursts. The dashed line shows the typical 2-second separation between 'short' and 'long' bursts and shows the bi-modal distribution that led many to believe that bursts in different categories had different progenitors.

Here, the factor of $(1+z)$ accounts for the effects of cosmological time dilation while the comoving volume is defined as

$$\frac{dV(z)}{dz} = \frac{c}{H_0} \frac{4\pi D_L^2}{(1+z)^2[\Omega_M(1+z)^3+\Omega_\Lambda]^{1/2}}, \tag{2.2}$$

for a flat Λ cold dark matter (ΛCDM) universe. We assume the fiducial cosmological parameters $H_0 = 71$ km s^{-1}, $\Omega_m = 0.3$ and $\Omega_\Lambda = 0.7$ throughout the work. Equation 2.1 forms the basis of the analysis, with the rate and luminosity function the major points of investigation.

Each burst is defined as a random redshift-luminosity pair, (z, L) chosen from the luminosity function (LF) and redshift distribution applicable to that problem. We test two types of luminosity functions, a power-law (Equation 2.3) and a smoothed broken

power-law (Equation 2.4). Although the luminosity function is generally difficult to probe, these are not a bad place to start, as many astrophysical problems follow such distributions.

$$\Phi(L) = \Phi_0 \left(\frac{L}{L_b}\right)^{-\alpha} \tag{2.3}$$

$$\Phi(L) = \Phi_0 \left[\left(\frac{L}{L_b}\right)^{\alpha_1} + \left(\frac{L}{L_b}\right)^{\alpha_2}\right]^{-1} , \tag{2.4}$$

In both Equations 2.3 and 2.4, L_b is the break luminosity and Φ_0 the luminosity function normalization. The basic rate for GRBs in Equation 2.1 is generally assumed to follow the star-formation history, although delays from mergers or effects from metallicity, when applicable, are folded into the rate.

Once a redshift and luminosity have been simulated from their respective distributions, the simultion proceeds through a series of filters that mimic a 'detection'. Ultimately, most approximations to the very complex detection criteria are, to first order, of the form of a flux or fluence truncation. The energy flux, then, is given by

$$F = \frac{L}{4\pi D_L^2 k}. \tag{2.5}$$

Here, k is the k-correction [191] that corrects the energy flux from the bolometric band into the detector bandpass, or vice-versa. Considering a detector with bandpass (e_1, e_2), the k-correction follows as

$$k = \frac{\int_{1/(1+z)}^{10^4/(1+z)} EN(E)dE}{\int_{e_1}^{e_2} EN(E)dE} \tag{2.6}$$

where $N(E)$ is the burst photon spectrum. The photon flux is given by

$$P = \frac{F \int_{e_1}^{e_2} N(E)dE}{\int_{e_1}^{e_2} EN(E)dE}. \tag{2.7}$$

The spectrum of bursts, which is needed in both Equations 2.5 and 2.7, is well fit by a smoothed broken power-law, the so-called 'Band function', derived empirically from BATSE observations in a seminal work in 1993 ([166]; Equation 2.8). This broken power-law joins smoothly from low to high energies with slopes of α and β and has a particular energy, E_0, which is related to the peak of the $\nu F\nu$ spectrum by $E_p = E_0(1+\alpha)$. *Swift* observations generally show power-law or cutoff power-law spectra, but this is usually attributed to the very narrow detector bandpass of the BAT instrument (15-150 keV), which peaks below the median peak spectral energy (E_p) values of BATSE. Extrapolations of such a spectrum would undoubtably produce an excess in high-energy emission [167]. Recent *Fermi* observations of GRB 080916C [56] show support for this model with a Band function fit to the spectrum over six to seven orders of magnitude.

$$N_E(E) = \begin{cases} A(\frac{E}{100keV})^{\alpha} exp(-\frac{E}{E_{peak}}), & (\alpha-\beta)E_{peak} \geq E \\ A[\frac{(\alpha-\beta)E_{peak}}{100keV}]^{(\alpha-\beta)} exp(\beta-\alpha)(\frac{E}{100kev})^{\beta}, & (\alpha-\beta)E_{peak} \leq E \end{cases} \tag{2.8}$$

We assume a Band spectrum with typical pre-break and post-break spectral parameters $\alpha = -1$ and $\beta = -2.3$ unless otherwise specified. The peak of the spectrum is highly uncertain, especially with the *Swift* sample following the arguments presented above. The best scenario for constraining E_p involves spectral fits from detectors, such as *HETE-2* or *BeppoSax*, that probe both the pre- and post-peak energy ranges allowing for a fit with the Band function and a derivation of the peak of the distribution. Most bursts in the *Swift* sample, however, are not detected on multiple instruments. The second method is to attempt to relate E_p to observed quantities, such as the spectral power-law slope [169], or an observationally derived quantity, such as the luminosity [170]. Both methods have intrinsic scatter involved but allow for the estimation of E_p. We utilize the luminosity estimation for all works

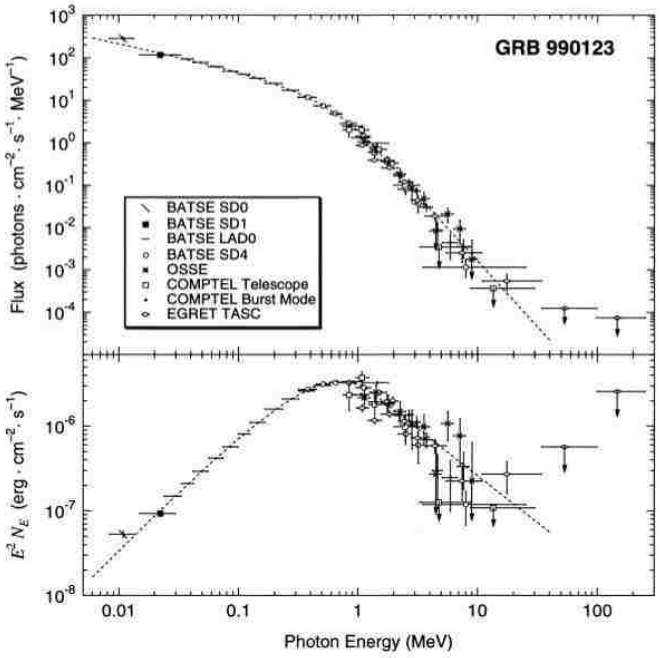

Figure 11 Band function fit to the spectrum of GRB 990123 [168].

([170]; Equation 2.9).

$$E_p/200\text{keV} = C^{-1}(L/10^{52}\text{erg s}^{-1})^{1/2} \tag{2.9}$$

With the spectral parameters chosen, the energy and photon fluxes can be calculated and then used with the detector threshold detailed in subsequent chapters. The final step is to test the consistency of the simulated samples with the available observations with a variety of statistical tests. The distributions tested are as follows:

- 1-dimensional redshift distribution
- 1-dimensional peak luminosity distribution
- Combined luminosity and redshift distribution
- Peak flux or $\log N - \log P$

CHAPTER 3

HIGH-LUMINOSITY V. LOW LUMINOSITY

The observations of GRBs 980425 and 060218 complicated the simple picture of the redshift and luminosity distributions of core-collapse (Type II) GRBs. It was generally believed that these types of bursts were related to the deaths of massive stars [171, 37, 172, 173, 174], and the observations of GRB980425-SN 1998bw [175, 139, 140] were the smoking gun for such an association. The complication, however, came with the outlier nature of the bursts. With only two detections, it is difficult to discern if the differences are caused by a natural extension of the higher-luminosity observations or if there is an intrinsic difference in the central engine, such as black hole versus a magnetar [176, 151, 177]. This section assumes all Type II, or core-collapse GRBs, and is based on the work presented in [178].

A variety of works have attempted to address this issue from the standpoint of the luminosity function of bursts, with two scenarios dominating. First, that the luminosity function of bursts is consistent with a single component and that the observations of low-luminosity (LL) GRBs are consistent with the remaining high-luminosity (HL) population [179, 180, 181, 182]. Second, that a second component to the luminosity function is necessary to explain the detection rate and distribution of LL-GRBs [183, 184, 185, 178]. Exploring these possibilities and understanding the physical implications is the aim of this study.

Prior works test both power law (PL, Equation 2.3) and broken power law (BPL, Equation 2.4) forms of the LF, as well as rates for GRBs that are proportional to the star-formation history (SFH). The method generally involves analyzing and inverting an equation similar to Equation 2.1 (or its integrated form) and creating a cumulative distribution function for luminosity, redshift and peak photon flux that is then fit and compared to the available observations. Specifying the form of the LF and SFH is necessary and easily comparable to computational methods. The most popular

versions of the SFH used are the functional forms of Robinson-Rowan and Porciani and Madau ([186, 187]; Equations 3.1 and 3.2).

$$\mathrm{SFH} = \begin{cases} 10^{0.75z} & z < 1 \\ 10^{0.75z_{peak}} & z > 1, \end{cases} \tag{3.1}$$

$$\mathrm{SFH} = 23\frac{\mathrm{e}^{3.4\mathrm{z}}}{\mathrm{e}^{3.4\mathrm{z}} + 22.0} \tag{3.2}$$

These SFH models rise quickly at low redshift and flatten off after peaking around a $z \sim 1$. Recent observations show that this is not likely the case and that the rate likely drops with increasing redshift, but to first order these models are sufficient for testing the problem at hand. Constraints to the form of the SFH and its relations to the cosmic metal enrichment history and the rate of GRBs will be further studied in Chapter 4.

Instrument threshold and detection biases also play a part in the simulations of our GRB sample. Once the flux is calculated from the method described in Chapter 2, it is necessary to adopt a threshold for detection. For the redshift and luminosity analyses, we adopt a flux threshold, F_{th}, for *Swift* events from [188]:

$$F_{th} \sim (5.3 \times 10^{-9} \text{ erg cm}^{-2} \text{ s}^{-1}) f^{-1} T_{90}^{-0.5}. \tag{3.3}$$

where f is the partial coded fraction of the BAT detector and T_{90} the duration of the burst. Generally, the peak flux (and therefore peak luminosity) is the given indicator for the brightness of a burst, and these are about five times larger than the average fluxes [189]. To compensate for this effect, we take a value five times larger than that given by Equation 3.3. In addition, Type II bursts average about 20 seconds in duration, which is what we assign the value of T_{90}. Together, these effects give an F_{th} of 1.2×10^{-8} erg cm^{-2} s^{-1}. LL-GRBs tend to have longer pulse durations [190], and

we use various discrete values for the durations, not exceeding 500 s (or $\sim 4.7 \times 10^{-10}$ erg cm^{-2} s^{-1}), when screening this component of the luminosity function. The last component of the threshold deals with the bias in detecting redshifts, as we consider solely this subset of bursts. This problem is very complicated and difficult to model and involves many variables, such as the availability of ground-based facilities to observe bursts quickly, line detections, weather considerations and a variety of other events that cannot be boiled down to one expression [191, 192]. Nonetheless, we approximate this effect in the form of a probability for detection of redshift (Equation 3.4) that is proportional to the flux level of flux above the flux threshold for a particular redshift which is in turn folded into the threshold condition.

$$p(F) = (1 - \frac{F_{th}}{F})^{\kappa} \tag{3.4}$$

Our analyses show that a value of κ of approximately 7 is needed to accommodate the observations.

For the analyses with the peak flux distribution (i.e. $\log N - \log P$, or LNLP), we do not consider such a detection probability. It is seen that a large fraction of bursts do no trigger the detector, especially if they are near the detection threshold. This was seen in the BATSE sample after an offline scan of the catalogue yielded many non-triggered GRBs [193]. The LNLP sample contains information of bursts independent of the redshift, and thus the sample is much larger than just the redshift-known sample, with about 2000 bursts in the BATSE 4B catalogue [194] and roughly 300 bursts during *Swift*'s first three years of operation, discounting any un-triggered events [195]. The LNLP distribution has a turnover at low photon flux due to the detector threshold, and we perform our statistics on only the bursts above this turnover, roughly 0.2 and 1 ph cm^{-2} s^{-1} for BATSE and *Swift*, respectively. By not adopting the previously mentioned flux threshold, these simulations have the advantage of

predicting the shape of the LNLP below current detection levels and add constraints to future missions that may probe the dim end of the GRB distribution.

The z-known sample (at the time of the original analysis) consists of roughly 100 GRBs, and we compare the redshifts and luminosities of these bursts with a set of 150 simulated bursts following the theoretical framework presented with the Kolmogorov-Smirnov (K-S test). The K-S test is a non-parametric test that compares the difference in the cumulative distribution of two distributions. In one form it can be used to test a distribution for normality, while in another it can be used to test the null hypothesis that two distributions are sampled from the same, yet unknown, underlying distribution [196]. The second form of the test is taken, utilizing the code found in [196], to assign a probability of consistency with the redshift ($P_{KS,z}$) and luminosity ($P_{KS,L}$). After considering the L and z samples separately, a value for the overlap of the areas of consistency between these tests can be given by $P_{KS,z} \times P_{KS,L}$, and this diagnostic is used to evaluate consistency in both parameters. The larger the value of the probability, the higher the likelihood of consistency with the null hypothesis.

The last test utilized is a test of the relative number of detected HL- to LL-GRBs. A model that claims to match observations should be able to reproduce the relative number of HL- to LL-GRBs seen by *Swift*. This ratio includes all triggered *Swift* bursts, not just the z-known subset, and is about 150 HL:1 LL.

Single-component model

The simplest assumption for the luminosity function (LF) of Type II GRBs is a single power law (Equation 2.3) component that accounts for all bursts (as adopted by [179] [180] (hereafter 'G04') [181] ('G05'), [182] ('G07')) and is the first type of LF tested with the developed Monte Carlo code. These works cite a variety of models as best fits to the observed distributions, as summarized in Table 1. G04 utilizes

Model	G04	G04(2)	G05 (P&M)[k]	G05 (RR)	G07	G07 (2)	G07(3)
Type	SPL	BPL	BPL	BPL	SPL	SPL	SPL
α^b	-0.7	-0.1	-0.1	-0.1	-1.6	-1.6	-1.6
β^c	-	-0.7	-2.0	-2.0	-	-	-
L_b^d	-	0.5	71	71	-	-	-
L_1^e	0.5	0.005	$71/\Delta_1^h$	$71/\Delta_1$	0.5	0.005	$5e^-4$
L_2^f	500	500	$71\Delta_2$	$71\Delta_2$	500	500	500
ρ_0	1.1	10	0.1	0.1	1.1	200	200-1800[j]
$p_{KS,z}$	0.00234	0.00018	$< 10^{-6}$	$< 10^{-10}$	$< 10^{-10}$	N/A	N/A
$p_{KS,L}$	0.00403	0.00022	$< 10^{-7}$	$< 10^{-9}$	$< 10^{-10}$	N/A	N/A
$p_{KS,t}$	$9.4e^{-6}$	0.00022	$< 10^{-7}$	$< 10^{-10}$	$< 10^{-10}$	N/A	N/A

Table 1 Various models of the luminosity function for high-luminosity 'long-soft' GRBs presented in the literature. Notes: a) SPL = simple power law, BPL = broken power law b) power law index c) For BPL models, power law index after the break luminosity d) break luminosity for broken power law e) lower luminosity cutoff in units of 10^{50} erg s^{-1} f) high luminosity cutoff in units of 10^{50} erg s^{-1} g) local GRB rate in units of Gpc^{-3} yr-1 h) $\Delta_1 = 30, \Delta_2 = 10$, See Guetta et al. (2005), j) Estimation from BATSE data, corrected to 110-1200 Gpc^{-3} yr-1 for BAT constraints (See [182]) k) Star forming rate model, Porciani and Madau (P&M) or Rowan-Robinson (RR).

the single power law without considerations for LL bursts, while G07 provides an updated analysis in lieu of the discovery of GRB 060218. Depending on the value of the lower luminosity cutoff, the observations allowed for local rates of 1.1, 200 or (200-800) Gpc^{-3} yr^{-1} combined with a LF slope of $\alpha = 1.6$.

A series of simulations were run using the parameters in Table 1, with the LNLP results summarized in Figure 12, L and z histograms in Figure 13 and 14, and 2D L-z scatter plots in Figure 15. In general, all the models suffer deficiencies in most tests. The G04 models are able to reproduce the shape and slope of the observed (HL) LNLP distribution and the general trends of the luminosity and redshift distributions, although the K-S probability is low (< 0.01). The model parameters available in G07 fare much worse, clearly deviating in both the LNLP and the L and z samples, causing a severe overproduction of bursts at low luminosities and redshifts. In the final test, no models were able to produce an observable LL-GRB with a single PL model LF, the earlier models due to a lower-bound luminosity greater than the luminosities of the observed LL-GRBs and the latter because of the very steep slope of the luminosity

function.

The next logical step for a single component model is a broken power-law (BPL, Equation 2.4) model. This distribution is more realistic, as it allows for a steepening at higher luminosities where fewer burst are expected. This model is also studied in the literature (G04, G05) and we once again test these distributions with the same method as the single PL model and summarize the results in Figures 12 - 15. These models have many of the same deficiencies as the single PL model, prompting us to consider the possibility that perhaps LL-GRBs require a more complex LF.

Two-component model

As seen above, a single component luminosity function has difficulties in simultaneously reproducing all aspects of the observed populations of Type II GRBs. Coward [183] and Liang *et al.* [185] instead propose a model where the observations are explained by a two component LF whose superposition accounts for the extrema in luminosity. Constraints from the number of detections are also an important argument in favor of two components. The detection of two bursts in less than a decade implies that the local rate of LL-GRBs ($\rho_{0,\mathrm{LL}}$) must be significantly higher than that of HL-GRBs, the literature quoting values ranging from $\rho_{0,\mathrm{LL}} = 100-1000\ \mathrm{Gpc}^{-3}\ \mathrm{yr}^{-1}$ [183, 197, 198, 151, 199, 185]. Liang *et al.* [185] calculate the Poisson probability of two detections within the volume of $z < 0.0331$, the redshift of GRB 060218, as less than 10^{-3}. Here we extend the work of Liang *et al.* [185] by introducing constraints from both the BATSE and *Swift* LNLP distributions as well as testing a wide range of parameter space.

To test this hypothesis, we run a set of simulations similar to those for the single component model, with the exception of the change in luminosity function. In order to save computational time, we simulate the two luminosity functions separately, with

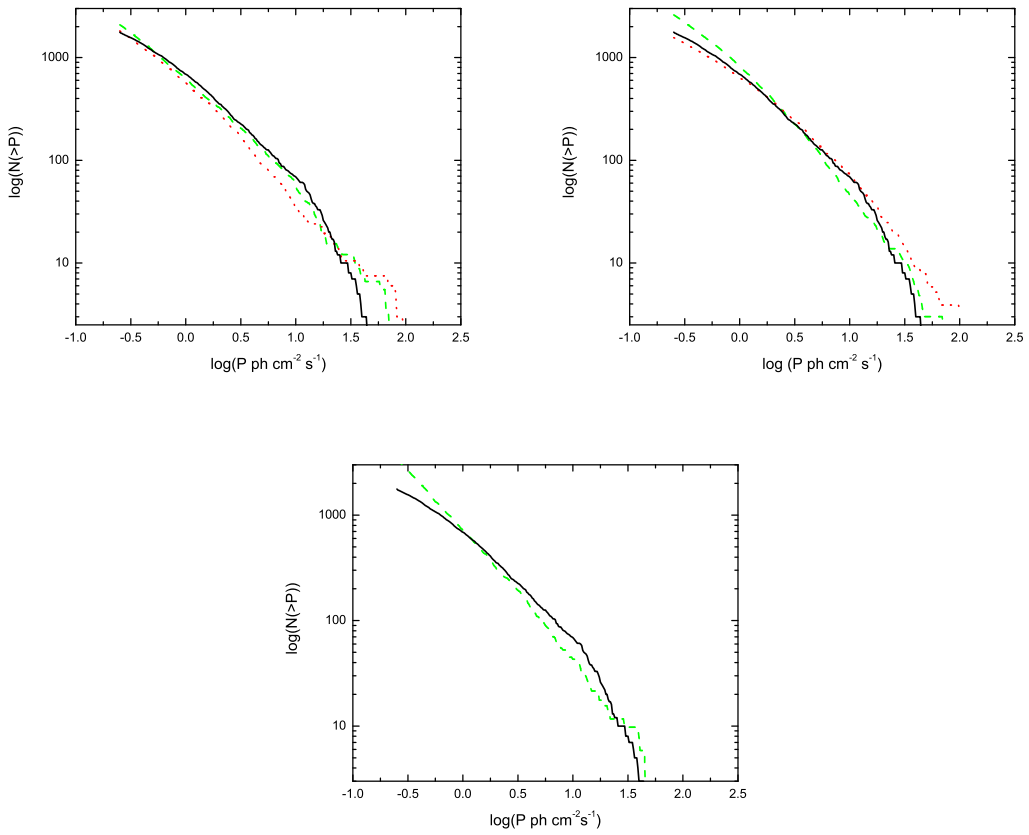

Figure 12 Single component LF model fits to BATSE $\log N - \log P$ distribution. The solid line (black) denotes the observed BATSE $\log N - \log P$ distribution in each panel. From left to right (a-c), we have the models from G04 (G04 (green, dash); G04(2),(red, dotted)) G05 (P&M (green, dash); RR(red, dotted), and G07 with the largest L_{min}. The first two models (G04, G05) can roughly reproduce the observation, while the last model (G07) is ruled out by the data. The observed BATSE distribution is the solid black curve in all panels. Model parameters can be found in Table 1.

the number of bursts in each category proportional to the ratio of the local rates, i.e.

$$N_{LL} = N_{HL} \frac{\rho_{0,\mathrm{LL}}}{\rho_{0,\mathrm{HL}}}. \tag{3.5}$$

Since there are such few detections of LL bursts, it is difficult to attain constraints to the variety of parameters for the LF. We assume the median values of the luminosity

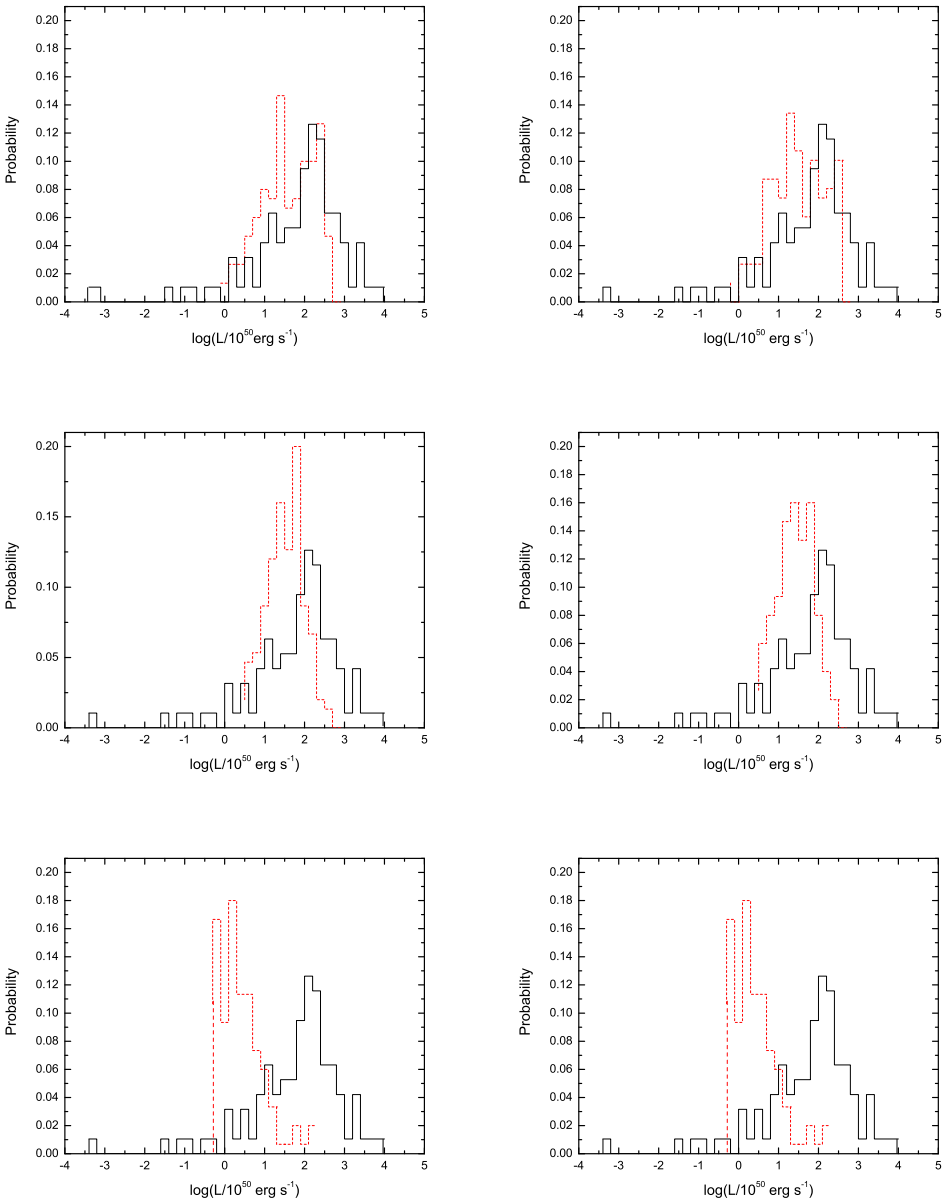

Figure 13 The 1-D luminosity distributions of various single-component LF models. The dashed curves (red) are the simulated results, while the solid curves (black) are the observed results for the redshift-known sample. Model parameters can be found in Table 1. The LF forms are, from left to right, G04, G04(2), G05 (P&M), G05 (RR), G07, G07(2).

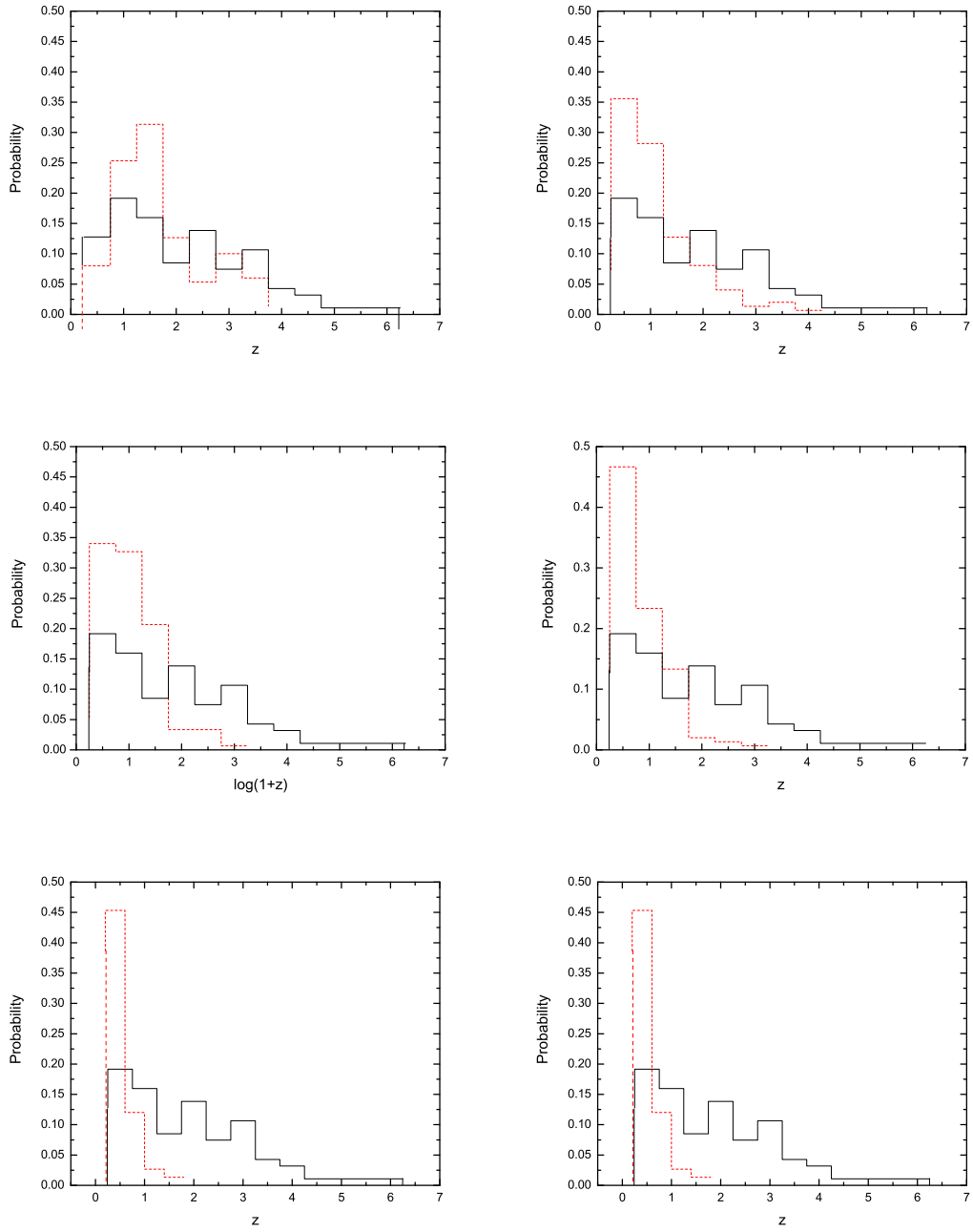

Figure 14 The 1-D redshift distributions of various single-component LF models. The dashed curves (red) indicate simulated results, while the solid curves (black) indicate the observed results for the redshift-known sample. The LF forms are, from left to right, G04, G04(2), G05 (P&M), G05 (RR), G07, G07(2). Model parameters can be found in Table 1.

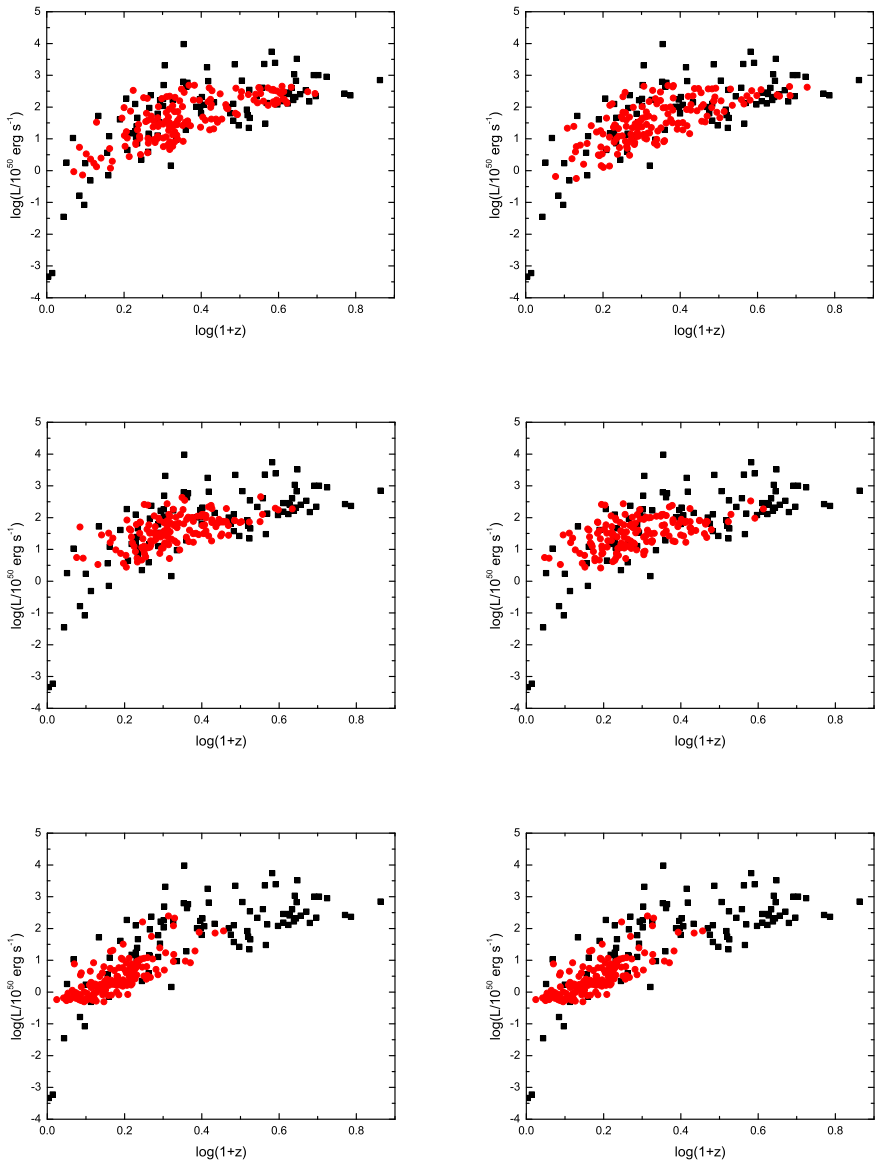

Figure 15 Two-dimensional luminosity-redshift distributions of various single-component LF models. The filled squares (black) are the observed redshift-known sample in the $z - L$ plane, while the filled circles (red) are the simulation results for various models. The LF forms are, from left to right, G04, G04(2), G05 (P&M), G05 (RR), G07, and G07(2). None of these models are able to reproduce the observed distribution satisfactorily.

function constraints from Liang *et al.* [185] and freeze these parameters in order to explore the constraints to the HL-GRB population. In addition, the post-break slope, $\alpha_{2,HL}$ is not highly dependent on the choice of parameters and we choose, once again, values from the literature for this slope, namely $\alpha_{2,HL} = 2.5$. Running the simulations gives, then, contours of consistency in $\alpha_{1,HL} - L_b$ space (e.g. Figure 16) whose peaks in consistency correspond to likely LF parameters that we use to create LNLP (Figure 17) and one- and two-dimensional L and z distributions (Figures 18 and 19).

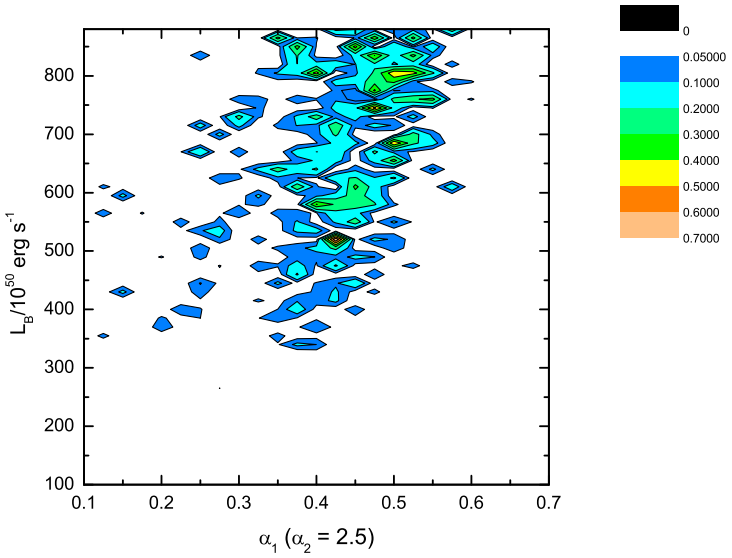

Figure 16 2-D $p_{KS,t}$ contour as a function of $\alpha_{1,\mathrm{HL}}$ and L_b at $\alpha_2 = 2.5$.

The results from these simulations are promising and provide constraints to the LF slopes and rates of LL- and HL-GRBs. Parameters corresponding to a variety of peaks in the K-S probability contour for $\alpha_{1,HL}$ and L_b are summarized in Table 2 and shown graphically in Figure 16, showing acceptable fits to the L, z and LNLP constraints. The L and z samples show small deviations from the observed sample

α_1^{LL}	α_2^{LL}	$L_B^{LL})^a$	ρ_0^{LLb}	α_1^{HL}	α_2^{HL}	L_B^{HL}	ρ_0^{HL}	$p_{KS,t}{}^c$
0.0	3.5	10^{47}	100	0.425	2.5	5.2×10^{52}	1	0.69
0.0	3.5	10^{47}	100	0.5	2.5	8.1×10^{52}	1	0.474
0.0	3.5	10^{47}	100	0.45	2.5	7.5×10^{52}	1	0.167

Table 2 Constrained luminosity function parameters for a two broken power-law luminosity function model. Notes: a) erg s^{-1} b) Gpc^{-3} yr^{-1} c) Total K-S probability, $p_{KS,t} = p_{KS,L} \times p_{KS,z}$

.

above a $z \sim 5$ and at luminosities below the peak of roughly 10^{52} erg s^{-1} which, although showing consistency with the null hypothesis, might be an indication of the effects of evolution or metallicity effects [200, 201, 202, 203, 204, 205, 206]. These are addressed in subsequent chapters. Other effects include the redshift detection bias modeling and detector threshold condition assumed for a detection. Further modeling is needed (see [205]), but to first order we believe this analysis is sufficiently robust to differentiate between models. In addition, the LNLP shows a small excess at the high photon flux end. Since most of these very high bursts are a small fraction of the total observed sample, the effect does not largely affect the rest of the fit to the distribution (see also [207]). Most importantly, this model is both consistent with the observed distributions of HL-GRBs and is able to produce LL-GRBs, unlike the previous models, as demonstrated in the figures.

The last criterion, the number test, also shows consistency with the observations but also highlights some of the uncertainty in this analysis. The acceptable parameter spaces have a range of ratios from 40:1 to 1000:1 depending on the local rates and durations (T_{90}) chosen for the bursts. For example, a value of $\rho_{0,LL}$ of 100 Gpc^{-3} yr^{-1} and a duration of 300 seconds gives a ratio of 218:1, generally consistent with the observations. If instead the rate is increased to 200 or 400 Gpc^{-3} yr^{-1} the durations that give reasonable ratios drops to 120 and 20 seconds, respectively. Small changes to the luminosity parameters (e.g. $L_b = 6.85 \times 10^{52}$ erg s^{-1} modified to 9.85×10^{52}

erg s^{-1}), however, does not significantly affect the ratio. The small number of LL bursts detected does not give a clear picture as to the distribution of durations of these bursts and further studies would benefit from new missions and detectors sensitive to these luminosities as well as sufficiently responsive so as to allow for quick ground-based follow-ups.

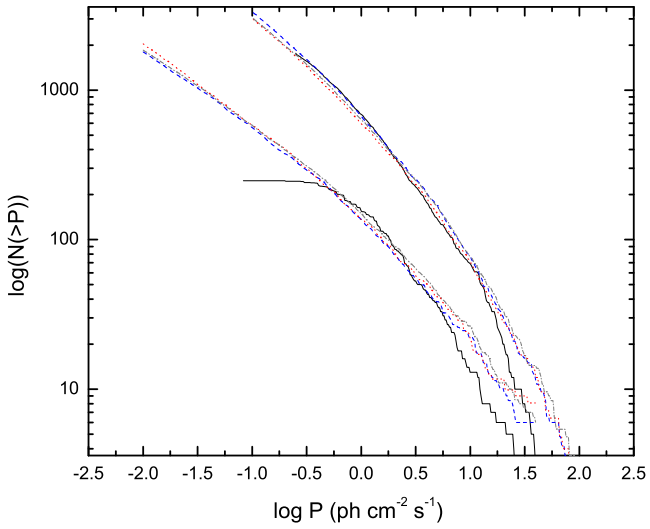

Figure 17 Two-component LF model fits to BATSE (top curves) and *Swift*/BAT (lower curves) $\log N - \log P$ distributions. The solid (black) curves are the observations, the dashed (blue) curves are the best fit parameters from the two-dimensional contour, the dotted (red) curves second peak in the probability distribution, and the dash-dot (gray) curves represent the middle parameters in the maximum of the $p_{KS,t}$ space (see Table 2 for details).

Observations such as the very low-luminosity x-ray transient x-ray flash (XRF) 080109 [208], with a peak luminosity of 6.1×10^{43} erg s^{-1}, might further imply very high event rates for LL-GRBs. It is unclear whether this burst is of a different class of low-luminosity x-ray objects where the observer is observing, for example, the breakout emission from the relativistic jet from the stellar cocoon [208] or whether the observer is seeing the jetted emission from a very low-luminosity GRB [209, 210].

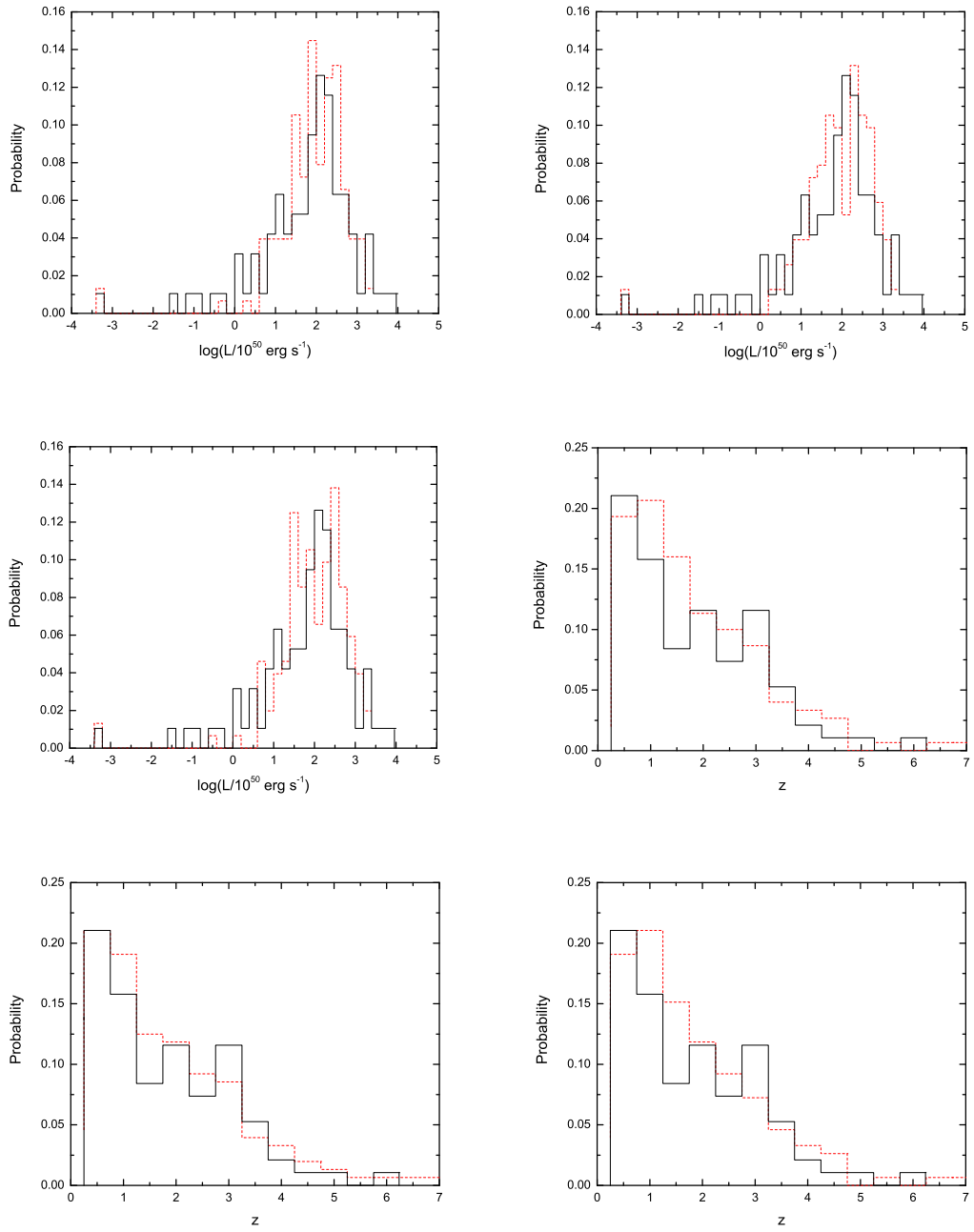

Figure 18 1-D luminosity and redshift distributions of simulated GRBs (dashed) generated from the 2-component LF model compared to the observed GRBs (solid). The panels correspond to best, intermediate, and center K-S probability fits, respectively.

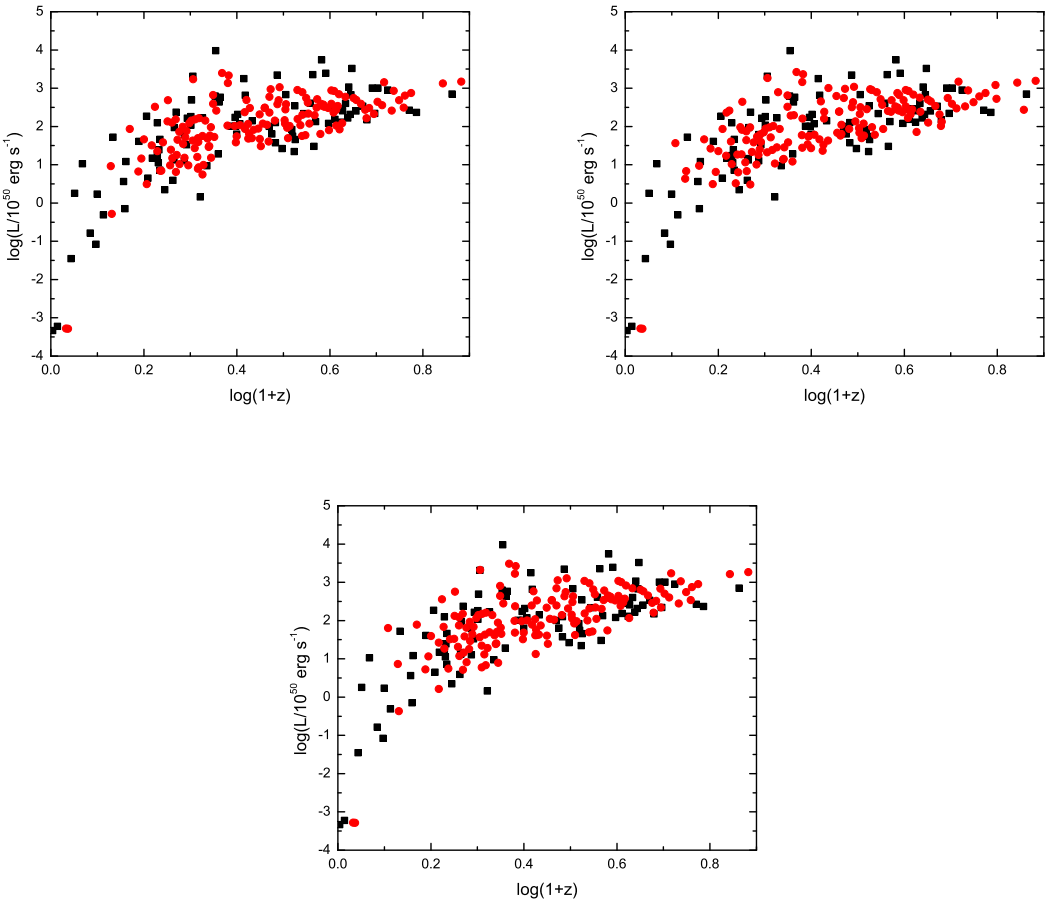

Figure 19 2-D $(z-L)$ graph of simulated bursts from the 2-component LF model (red, circles) as compared to the observed GRBs (black, squares). The panels correspond to best, intermediate, and center K-S probability fits, respectively.

Analyzing the x-ray spectrum shows that this event has a spectrum consistent with non-thermal emission, differing from the shock breakout candidate XRF 060218 [174]. If XRF 080109 is a very LL-GRB, then the high implied event rate [208, 210] would be consistent with and strengthen the conclusion that LL-GRBs are from a separate population from HL-GRBs.

Although the sample of LL-GRBs is still relatively small, we have performed a robust analysis of the various LF models with numerical simulations. We come to

the conclusion that the previously analyzed single component models are insufficient in simultaneously reproducing the variety of observations of the redshift, luminosity and peak flux distributions of the observed HL and LL-GRB samples. We have further analyzed a two-component model as proposed by Coward [183] and Liang *et al.* [185], showing that this model is able to produce bursts not only consistent with all the distributions mentioned previously, but also with the general number of observed bursts. Further effects, such as metallicity and evolution of the luminosity function, will affect only the HL population and are studied in greater detail in the next chapter. Further observations of LL events are most certainly needed and will provide information about the detection rate, typical durations and possible clues as to the internal processes of these bursts from a variety of empirical relations (e.g. Amati relation [211], lag-luminosity [190], etc.) and their temporal and spectral characteristics.

CHAPTER 4

HIGH-Z BURSTS AND CONSTRAINTS TO THE RATE OF TYPE II GRBS

As opposed to the previous study of under-luminous and very local GRBs, the newest frontier involves gaining insight from the most distant observed bursts at very high redshifts. Since the end of the distance debate that firmly established the cosmological origin of GRBs (see Chapter 1), largely due to the first afterglows and redshift determinations [27, 25], there have been great advances in rapid localizations and optical spectroscopy and fitting that have allowed for the discovery of bursts up to a redshift of 8.3 (GRB 090423; [158, 159]). To put this into scale, the age of the Universe at that time was a mere 650 million years, more than 13.5 *billion* years in the past. Theoretical estimates place the detection limit for GRBs in the area of $z \sim 20$ ([212, 213]), although the mechanics of such a detection are extremely difficult and require very long exposures in progressively longer (far-IR and IR) bands in order to create spectra with sufficient signal-to-noise ratio to be fit. With the introduction of these new high-z bursts, it is necessary to perform analyses to see how their addition affects our understand of the population of stellar collapse (Type II) GRBs and what, if any, differences exist within the entire population.

Theory and simulations

This analysis deals strictly with 'long-soft', or Type II, GRBs. The differences between Type I and Type II bursts are highlighted in full detail in the next chapter. It is generally believed that Type II GRBs are the product of the catastrophic core-collapse of massive stars, with the strongest evidence coming from the association of some bursts with Type Ib-c supernovae [173, 172]. A natural consequence of this association is that the rate of GRBs would be expected to follow the rate of their progenitors, the cosmic star-forming history (SFH) [214, 215, 216, 217, 187]. A variety of studies, however, have shown that the rate of GRBs does not strictly follow the SFH

but rather is enhanced at high redshift [200, 184, 218, 204, 202, 203, 158, 205, 206]. Pioneering analyses deduced that the rate should increase with redshift from Monte Carlo analyses [200], fits to jet opening angle and redshift distributions [184] and luminosity function and redshift distribution fits [218]. Further studies suggested that the increase could be the product of the decreasing cosmic metallicity with increasing redshift [219, 202, 203, 158, 205, 206], selection effects or the increase in the number of progenitors [202, 203].

Here, we combine and expand various elements from these works to further analyze possible GRB rate enhancements with redshift in order to study the underlying causes and forms of these possible evolutions. This is achieved with Monte Carlo simulations and comparisons with the current observational sample. Specifically, we look at the form of the star-formation history since association with massive stars is a fundamental assumption of many works. We also include a model of the SFH derived from cosmological smooth-particle hydrodynamics (SPH) simulations of Choi and Nagamine [220] and address the issues of metallicity enhancement and evolution of the GRB rate and luminosity function.

Similar to the analysis in [178] and Chapter 3, the goal is to test a variety of *intrinsic* distributions from the available *observed* quantities. The theoretical framework remains the same as the previous analysis with the removal of the LL-GRBs, a larger sample including more high-z detections, and a few improvements to the code.

The first improvement is the addition of a variety of subroutines from the GNU Scientific Library [221] as well as a more robust (pseudo) random number generator created specifically for scientific Monte Carlo simulations [222]. Improvements were also made to the handling of the simulated trigger threshold and simulated spectra. The new trigger threshold is based on the probability of triggering *Swift*, as derived

empirically by Qin *et al.* [205]

$$\eta_t = \begin{cases} 5.0P^{3.85}, & P < 0.45 \\ 0.67(1.0 - 0.40/P)^{0.52}, & P \geq 0.45 \end{cases} \quad (4.1)$$

where P is the photon flux of the burst in the 15-150 keV band. Although Qin *et al.* [205] do not find a significant difference between samples, they also include an empirical expression for the redshift detection probability, given by

$$\eta_z = 0.26 + 0.032e^{1.61 \log P}. \quad (4.2)$$

The redshift detection probability is only included for the L and z constraints. This detection threshold is based on the similarities of the peak photon flux distributions observed by *Swift* and BATSE and show similar final results to Equation 3.3 with the added benefit of not assuming a form for the T_{90} distribution. Both these constraints and the LNLP analysis rely on the photon flux, which is calculated as presented above with the exception of the Band function parameters. The peak energy of the νF_ν spectrum is again derived from Equation 2.9 [170], but the indices are chosen randomly from the observed limits of $-0.83 < \alpha < -1.2$ and $-2.1 < \beta < -2.5$.

Other improvements include an updated observed sample and statistical tests for comparison with the simulated sample. The observed sample consists of 166 *Swift*- and *HETE*-era GRBs with known redshifts detected through September 2009. We remove LL and Type I GRBs from the sample as well as those with non-secure redshift detections and incomplete observations that do not enable the derivation of a luminosity. The luminosities are derived from the observed one-second peak fluxes and observed spectral parameters. In addition, a Band function spectrum is assumed with post-E_{peak} slope of -2.5 when not observed. This quantity is often not observed in *Swift* bursts due to its narrow energy band [188], which makes the determination

of E_{peak} difficult. Values presented in the literature are used when available, and the remaining bursts are assigned an E_{peak} from the catalog of Butler et al. [223]. In order to compare this sample to the observations, we utilize the k-sample Anderson-Darling (AD) test [224] which tests the null hypothesis that k (in this case 2) distributions are sampled from the same unknown underlying distribution. By testing the luminosity and redshift samples, we are able to find areas of luminosity function parameter space where the probability of accepting the null hypothesis is highest, creating figures similar to Figure 16. Once again, the post-break slope of the luminosity function is kept constant ($\alpha_2 = 2.2$ or 2.5), as the results are generally insensitive to this quantity [185, 178, 205]. From the maxima of the joint probability contour, we test the LNLP distributions from the acceptable parameters with the AD test. For this distribution, the redshift probability is removed and all bursts that would trigger *Swift* are tested. In order to have the most complete and unbiased sample from each, the distributions are truncated at 0.4 [50-300 keV] and 1 [15-150 keV] ph cm^{-2} s^{-1}, respectively (see [225, 226]), leaving 1143 and 380 BATSE and *Swift* bursts. Results from statistical tests are summarized in Tables 4-8 found at the end of this chapter.

Star-formation history

In addition to the luminosity function the most important modeling in this analysis is related to the GRB rate found in Equation 2.1, how this rate relates to the cosmic star-formation history and what, if any, constraints are provided by the expanded redshift distribution. This is achieved by considering a variety of SFH models and enhancements at high-z.

- Cosmic star-formation history

  A variety of forms of the SFH are found in the literature, derived from galactic surveys and Type Ia SN observations. In general, the rate increases very rapidly as redshift increases, peaking around a $z \sim$ 1-2. The high-z region is the

most difficult to constrain, and most models consider a plateau to high redshift or, more realistically, a decreasing trend. We consider several SFH models, most empirical fits to the data and one calculated from cosmological smooth-particle hydrodynamical (SPH) simulations. As a control, a few models are tested with the SF2 model of Porciani and Madau ([187]; henceforth 'PM') shown in Equation 3.2. More realistically, we consider models that fall off after a peak at lower redshifts. Two models used extensively are those by Hopkins and Beacom ([227]; 'HB') and Bromm and Loeb ([228]; 'BL'):

$$\dot{\rho}_{\rm SFH}(z) \propto \begin{array}{lcl} (1+z)^{3.44} & : & z < 0.97 \\ (1+z)^{-0.26} & : & 0.97 < z < 4.48 \\ (1+z)^{-7.8} & : & 4.48 < z \end{array} \tag{4.3}$$

The HB model (Equation 4.3) drops very quickly with redshift after its peak, with a very steep power of -7.8 above a redshift of about 4.5. The BL model, shown in Figure 20 with the other SFH models, was extracted from the 2006 work of Bromm and Loeb [228] and shows two broad peaks in the SFR, one for Population II stars and a higher-redshift peak corresponding to the contribution from primordial Population III stars (Figure 20). This model is already disfavored by the observations of GRBs since, to date, all GRBs are consistent with higher metallicity Population II stars.

In addition, we utilize a model derived from cosmological SPH simulations from Choi and Nagamine ([220], or 'CN'). They have developed a modified version of GADGET-3 code (originally described in [229]), including radiative cooling by H, He, and metals [230], heating by a uniform UV background of a modified [231] spectrum [232, 233], a sub-resolution model of multiphase ISM [234], the "Pressure" star formation model [235, 220], and the "Multicomponent Variable Velocity" galactic wind model [236]. The adopted cosmological parameters

are consistent with the WMAP best-fit values [237]: $\Omega_m = 0.26$, $\Omega_\Lambda = 0.74$, $\Omega_b = 0.044$, $h = 0.72$, $n_s = 0.96$, and $\sigma_8 = 0.80$.

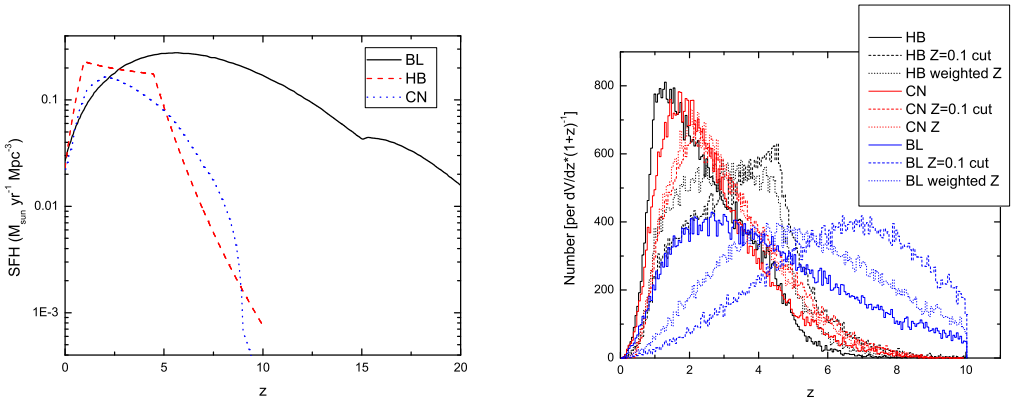

Figure 20 (a) Star-formation history models utilized in the analysis (b) Relative number of GRBs per unit comoving volume$\times(1+z)^{-1}$. This panel shows the output from the code without a threshold, so as to check the underlying distribution and see the relative affects of the metallicity relations on the base SFH.

- Metallicity

  One of the possible explanations for the possible enhancement of the GRB rate with redshift, as argued in various works [200, 184, 218, 204, 202, 203, 158, 205, 206] is the lower overall cosmic metal enrichment at high redshifts [219, 204, 205]. If GRBs prefer lower-metallicity environments, then the decrease of metallicity with decreasing age of the Universe could be a cause for an increased rate of GRBs. Langer and Norman([219], 'LN') propose an analytical form for the enhancement of the GRB rate caused by metals, based on the galactic initial mass function (IMF)

$$\Phi(M) = \Phi_\star (M/M_\star)^\alpha e^{(-M/M_\star)} \tag{4.4}$$

  where LN have constrained the slope as $\alpha = -1.16$ and the normalization to

$\Phi_\star = 7.8 \times 10^{-3} h^3$ Mpc^{-3}. From here, the mass density of galaxies with mass $m < M$ can be expressed as

$$\Psi(M) = \frac{\int_0^M M\Psi(M)dM}{\int_0^\infty M\Psi(M)dM} = \frac{\Psi_\star \int_0^M M(M/M_\star)^\alpha e^{(-M/M_\star)}dM}{\Psi_\star \int_0^\infty M(M/M_\star)^\alpha e^{(-M/M_\star)}dM}. \tag{4.5}$$

The last expression in Equation 4.5 is very similar to the expressions for the complete and incomplete gamma functions:

$$\Gamma(s) = \int_x^\infty t^{s-1}e^{-t}dt \quad \text{and} \quad \hat{\Gamma}(\mathrm{s,t}) = \int_0^\mathrm{x} \mathrm{t}^{\mathrm{s}-1}\mathrm{e}^{-\mathrm{t}}\mathrm{dt}. \tag{4.6}$$

Substituting $t = M/M_\star$ and $\alpha = s - 1$ and rearranging the integrals, the expression for Ψ becomes

$$\Psi(M) = \frac{\int_0^M t^{\alpha+2}e^{-t}dt}{\int_0^\infty t^{\alpha+2}e^{-t}dt} = \frac{\hat{\Gamma}(\alpha+2, M/M_\star)}{\alpha+2}. \tag{4.7}$$

This expression, however, is for the galaxy mass fraction and not the metallicity, which is the ultimate goal. In order to take this next step, LN [219] utilize galaxy survey observations that show a correlation between the mass of a galaxy and its metallicity, known as the mass-metallicity relation [238, 239]. This is generally taken in the form

$$M/M_\star = K(Z/Z_\odot)^\beta \tag{4.8}$$

where K and β are constants that are constrained from observation. In addition, the overall cosmic metallicity decreases with increased redshift and LN utilize $d[Z]/dz = -0.15$ dex per unit redshift to reflect this reduction [240]. Combining the mass-metallicity relation with the expression for the mass fraction they arrive at

$$\Psi(\frac{Z}{Z_\odot}) = \frac{\hat{\Gamma}[\alpha+2, (Z/Z_\odot)^\beta 10^{0.15\beta z}]}{\Gamma[\alpha+2]} \tag{4.9}$$

to express the metallicity scaling with redshift. Here, β is the fit to the observed mass-metallicity relation, α the slope of the observed galactic IMF and ϵ the cutoff metallicity in units of solar metallicities $Z/Z_{\odot}$. Please note the often confusing convention of abbreviating the metallicity as a capital 'Z' and the redshift as a lower-case 'z'. Equation 4.9 shows the net effect of metallicity on the GRB rate. Initially, we work with the assumed parameters in the literature, $(\alpha = -1.16, \beta = -2, \epsilon = (Z/Z_{\odot}) = 0.1)$ and then enhance the analysis by considering a model with weighted metallicity from $\epsilon = 0.1 - 0.4$ to reflect the metallicities of observed GRBs. This function also contains many assumptions about the underlying galactic IMF and mass-metallicity relation, which are discussed below. A comparison of the different expressions used is shown in Figure 21, and the relative effects of this expression on the SFH are summarized in Figure 20b.

The cosmological simulations derive star formation rates for populations of stars from various metallicities without the need of an external expression. In the simulation, at every time step, star particles are created in high-density regions that exceed threshold density according to the star formation law that is matched to the locally observed Kennicutt law [241]. Once a star particle is created, instantaneous recycling is assumed, and the metals are ejected with a yield of $Y = 0.02$ and distributed to the nearby environment by the galactic wind. Niino *et al.* [242] have used similar simulations to examine the metallicity of GRB host galaxies and found good agreement with observations.

- Rate evolution with redshift

  Another solution to the increased rate is the evolution of the rate of the GRBs with redshift, occurring due to an unknown process. This model does not have a physical basis but is considered often in the literature (e.g. [202, 203, 205])

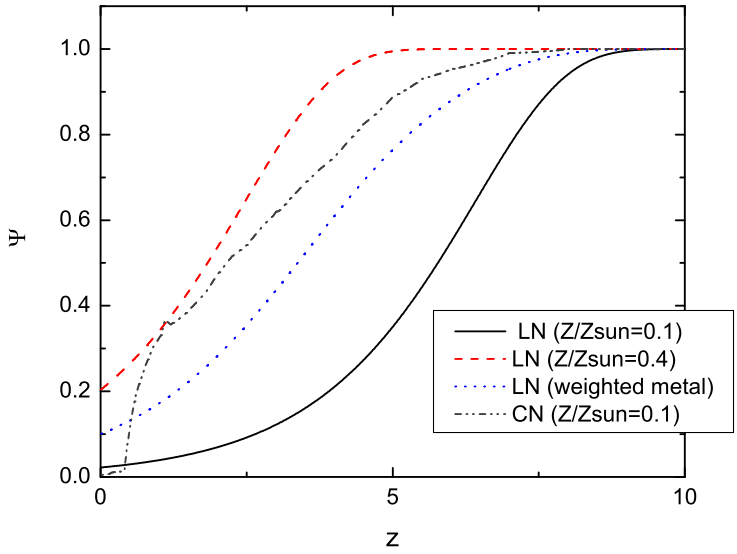

Figure 21 Expression from [219] (LN) including different metal cuts ($Z/Z_{\odot} = 0.1, 0.4$) and modifications from weighting. The expression derived from the star-formation history of CN with a metal cut of 0.1 is included for comparison.

and simply has the rate of GRBs evolving with redshift as $(1+z)^{\delta}$, where δ is a free parameter.

- Luminosity function break evolution with redshift

  This form of evolution tests if the GRB rate is enhanced to do a systematic brightening of bursts with higher redshift. It assumes that the break luminosity of the GRB luminosity function, L_b in Equation 2.4, increases with redshift by a factor of $(1+z)^{\gamma}$, where γ is a free parameter.

Results

Here, we present the simulation results organized by star-formation history or rate enhancement.

GRB rate $\propto$ SFH

This is the simplest scenario possible for the GRB rate, and simulations show little consistency with the current observations. Of the four models considered [187, 228, 227, 220] the only favored model is that of Bromm and Loeb [228]. This model implies a shallow pre-break slope to the luminosity function, on the order of or shallower than $\alpha_1 = 0.2$. This model also has a significantly higher rate out to larger redshifts compared to the others, indicating that some sort of rate increase is needed, and determining the form of that enhancement is a major goal of this analysis. The model of Bromm and Loeb [228], however, attributes this high-z contribution to the rate to first-generation (Population III) stars that developed in the Universe around $z \gtrsim 15$. Current observations of GRBs do not show evidence that the highest-redshift GRBs are significantly different from those occurring at lower redshifts, implying that they are most likely from a later round of star formation (Population II). We caution drawing an association to Population III stars solely on the form of the star-formation history and therefore do not prefer this model.

GRB rate $\propto$ SFH + metallicity

The next step is to consider the addition of a term that accounts for an increase in the GRB rate due to the decrease in the cosmic metallicity at high redshift. Utilizing the formalism derived above ([219]; See also [204, 205]) we run a set of simulations similar to the previous section, utilizing Equation 4.9 with parameters from the literature ($\alpha = -1.16$, $\beta = 2$, $\epsilon = Z/Z_{\odot} = 0.1$). Like previous analyses, we do not consider further effects such as the evolution of the galactic IMF nor changes to the the normalization of the mass-metallicity relation (K). K is modified to some extent, as it is absorbed into the $10^{0.15\beta z}$ term in Equation 4.9. Results from the simulation show that the BL model can accommodate the L and z constraints to the 2σ level. Utilizing the SFH derived from cosmological simulations with a strict metal cut of

$\epsilon = 0.1$ shows similar results, namely that this form of enhancement is insufficient to explain the observations. The same Population III star argument holds here as well.

GRB rate $\propto$ SFH+weighted metallicity

A more realistic scenario would be to include contributions to metallicity effects from a variety of metallicities, not just a simple cut. This is motivated by observations of GRBs that happen in environments with metallicities greater than $Z/Z_{\odot} = 0.1$. Taking metallicities below $Z/Z_{\odot} = 0.4$, we weight the contribution of the metallicities in each redshift bin, creating an 'effective' Ψ. The contribution from higher metals peaks at low redshift and falls off exponentially, creating the intermediate curve in Figure 21, with all solutions converging to 1 (no effect to the GRB rate) at high redshift.

Using this formulation we re-run the simulations and find that the HB [227] is the only model that passes all the observed constrains, giving luminosity function parameters in the range of $(\alpha_1, \alpha_2, L_b) = (0.11 - 0.19, 2.2, 6 - 10 \times 10^{52}$ erg s$^{-1})$.

Further metallicity considerations

An interesting comparison, which until this point has been ignored, is the differences between Equation 4.9 and the equivalent relation derived from the star-formation rate from cosmological simulations. Inspection of Figures 20b and 21 clearly show the non-negligible differences between the the metallicity effects on the various models. Why would the CN and HB models, whose rates are not significantly different, vary so notably when adding in the metallicity expression? The relation presented in Langar and Norman [219] is an approximation to a very complex problem in galaxy evolution. The cosmological simulations by Choi and Nagamine [220] address a variety of effects that contribute to the metallicity and allow for calculating the star-formation rate for a variety of metallicities. From those values, a realistic view of

how the total rate is affected by the reduction in metallicity can be calculated, which is just what Equation 4.9 shows: the net effect to the total star-formation rate by a metallicity cut at $Z/Z_{\odot}$. The curves for various values of $Z/Z_{\odot}$ are shown together with the equivalent expression from the CN (Figure 21 and 22).

Motivated by these differences, we analyze the assumptions that go into formulation Equation 4.9 and attempt to find ways to improve the formulation to more fully accommodate the underlying physical processes. The most outstanding assumption in Equation 4.9 is the constant value for the galactic IMF slope, α. Bouwens *et al.* ([243]; and references therein) observe an evolution of this slope with its value decreasing with increasing redshift, reflecting the increase in typical galaxy size with the evolution of the Universe. Bouwens *et al.* detail several observations of galaxies at $z \sim 7-8$ and summarize the luminosity function of galaxies. From their Figure 15 we were able to extract the slopes of the IMF for various redshifts and utilize these values with our code. Using a spline fit and cubic interpolation, we are able to approximate the behavior of α as well the behavior of the maximum and minimum error bars. The results are summarized in Figure 22a. As shown, the values of α range from $-1 > \alpha > -2$ from $z = 0-8$. For this analysis, we consider only values of $\alpha > -2$ (which only affects the minimum error solution). as the metallicity relation is undefined at the values $\alpha + 2 = 0$. For this case, as well as redshifts greater than ~ 8, we assume α becomes a constant at the value of the last data point (or error bar value). The effects of this addition are summarized in Figure 22b. This approach, although more realistic, also showed little consistency with the observations. The HB model shows no consistency in all tests (to 2σ), while the BL model shows some areas of consistency in L and z but large deviations with the BATSE and *Swift* LNLP distributions. Relaxing the constraint to 3σ, the HB model fares better, showing consistency in all tests, implying a generally shallow luminosity when paired with the distributions of the central and maximal values of α. The lower amount of agreement

is attributed to the general overproduction of bursts around a $z \sim 1-2$ inconsistent with the observed z sample. Shallow slopes of the luminosity function, however, are generally consistent with the L sample alone. Figure 23 shows various contours for the HB SFH model with both central and maximal distributions of α evolution.

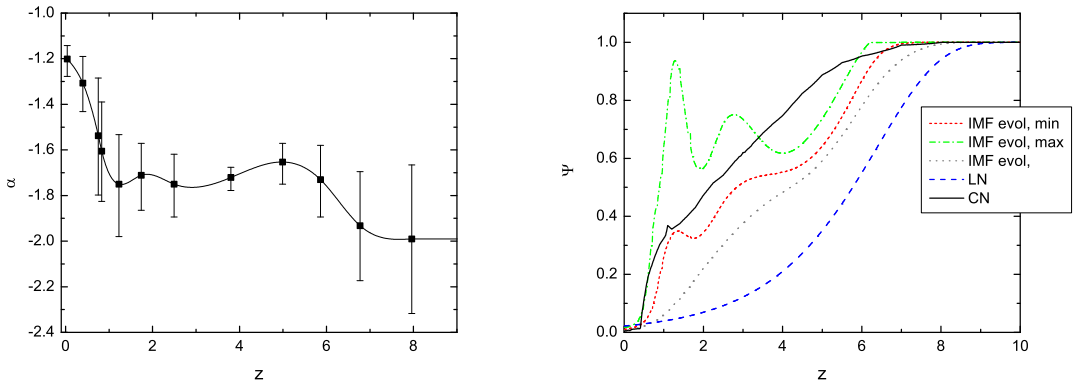

Figure 22 (a) Galactic IMF slope, α, evolution with redshift, including error bars [243]. (b) Effect of the evolution of α on the expression from LN. The $Z/Z_{\odot} = 0.1$ cut expression from LN and CN are included for comparison.

$$\text{GRB rate} \propto \text{SFH} \times (1+z)^{\delta}$$

As detailed in the literature (e.g. [202, 203, 205]), we also consider an increase in the GRB rate parametrized as $(1+z)^{\delta}$, where $\delta = 0.2, 0.5, 0.8$. We also combine this evolution with the star-formation history with and without metallicity formulations, with the exception of models with galactic IMF slope evolution. Some of these models are able to pass the L and z constraints, but all fail to pass the BATSE, and in some cases *Swift*, LNLP constraints.

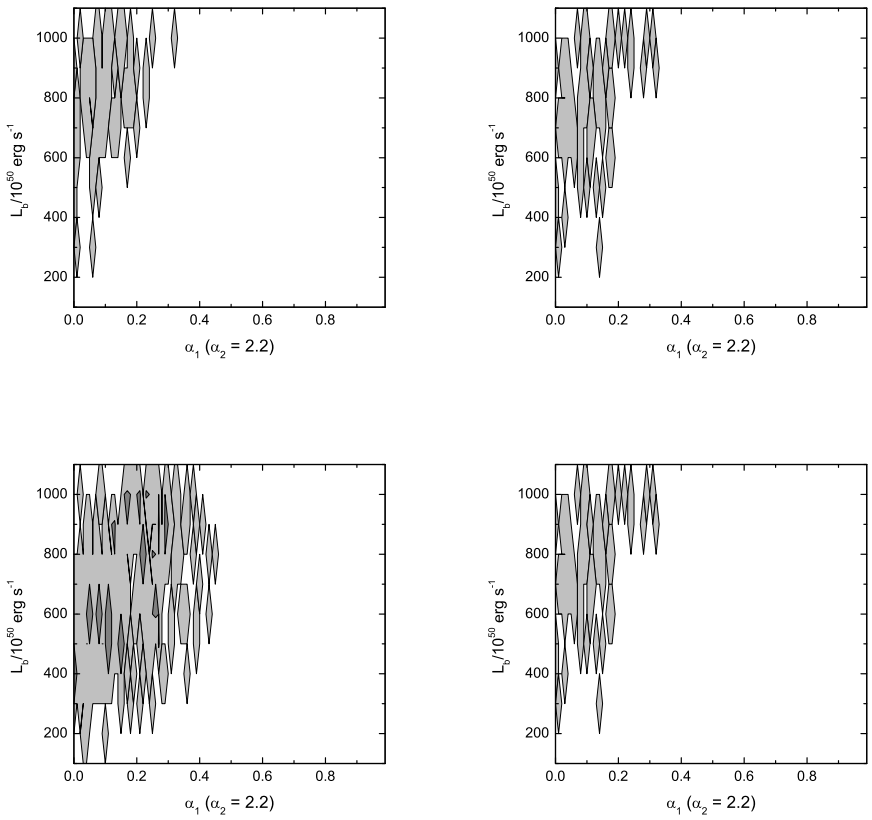

Figure 23 Contours of consistency with BOTH L and z constraints for a variety of models with the HB SFH and evolving galactic IMF slope, α. Dark grey = 2σ contour and light grey 3σ contour. (a) α evolution and $\epsilon = 0.1$ metallicity cut (b) α evolution and weighted metallicity (c) maximum α values and $\epsilon = 0.1$ metal cut (d) maximum α values and weighted metallicity.

Luminosity function break evolution $\propto (1+z)^{\gamma}$

Finally, we consider evolution of the luminosity function break luminosity, L_b, with redshift. Simulations with the CN SFH model (derived from cosmological simulations) show broad areas of consistency when paired with this type of evolution and $\gamma \sim 0.5 - 1.5$, with some models showing patches of 2σ consistency ($\gamma = 1.0, 1.3$; See Figure 25). Once again, the general trend is shallow luminosity function slopes, the best models occurring in the area of $(\alpha_1, \alpha_2, L_b, \gamma) = (0.5, 2.2, 3 \times 10^{52}$ erg s^{-1}, 1.0).

The HB model also shows some consistency to 3σ, although not as broadly as the CN model.

Discussion

Above are details of a numerical and statistical approach aimed at understanding the properties of the GRB rate in the context of the cosmic star-formation history, including constraints from newly discovered high-z bursts and possible metallicity and evolutionary effects. Similar recent analyses agree with the necessity for an increase in the rate although differ in the type of evolution necessary. Qin *et al.* [205] and Wanderman and Piran [206] both find that the luminosity function can be fit with a BPL model but require that the rate evolve strongly with redshift, proportional to $(1+z)^{0.6-2}$, which we do not find. Such a rate evolution was disfavored by the LNLP constraints. Furthermore, our analysis has the added benefit of a variety of SFH models, including one derived from cosmological simulations [220] as well as further analysis of the underlying assumptions of the metallicity relation utilized in a variety of works [219, 204, 205]. Although a simplistic model of the metallicity shows consistency with the observation (i.e. HB SFH and weighted metallicity relation) we show that a more realistic consideration, including evolution of the galactic IMF slope, shows promise in addressing the increased rate but may not be the sole cause of the increase. Additional observational evidence of this evolution comes from the observation of GRB host galaxies, where Laskar *et al.* [244] show that the mass-metallicity relation evolves between redshifts of 3-5.

Another model that shows promise is an evolution of the LF break luminosity with redshift, $\propto L_b \times (1+z)^{\sim 0.8-1.2}$. Butler *et al.* [223] do not favor models with luminosity function evolution, but their parametrization is generally much stronger, following as $L \times (1+z)^{\gamma}$ instead of L_b. Their metallicity models also include the relation from LN without considering the effects of the evolution of the IMF slope, although they

relax the metallicity cut to $\epsilon = 0.2 - 0.5$ to depict a more realistic constraint. These differences might be the origin of the discrepancies seen in our analyses.

In general, we provide constraints on the form of the evolution of the GRB rate with redshift. Further work is needed in fully dissecting and understanding the assumptions behind metallicity enhancements and how the galactic and stellar IMFs and other effects work together to affect the GRB rate. In addition, the evolution may be of multiple origins and additional work on superpositions of these effects may yield further constraints.

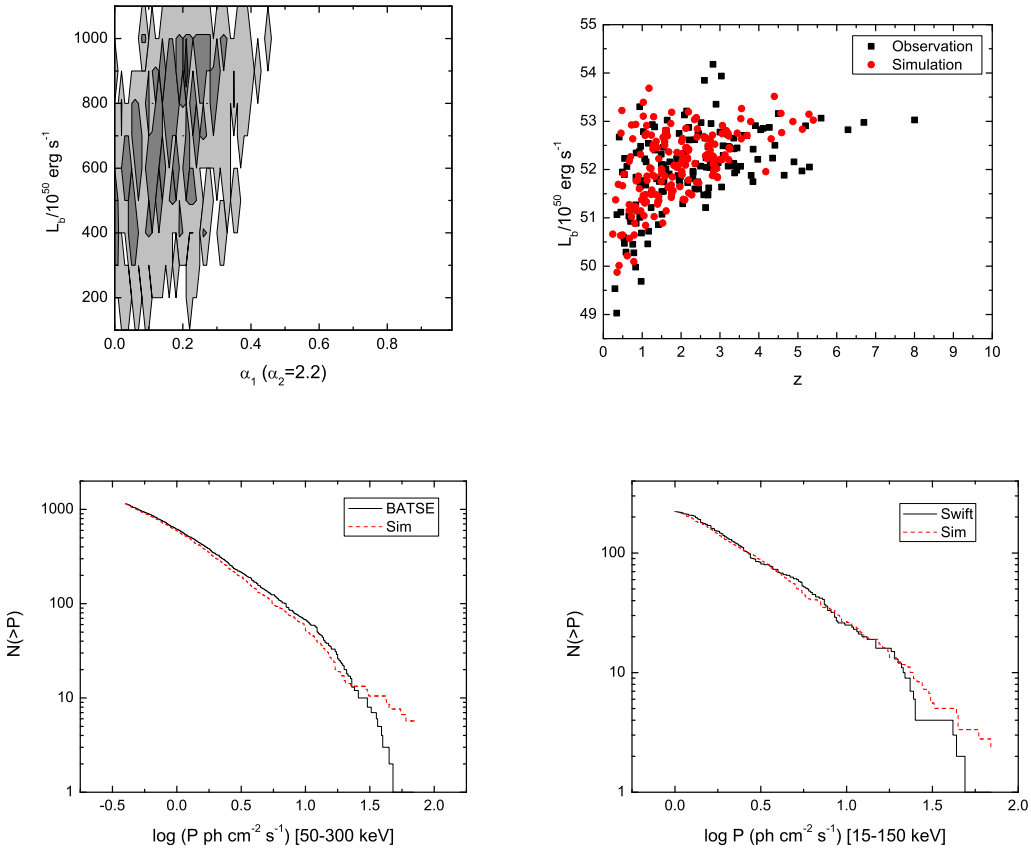

Figure 24 HB SFH model with the weighted LN expression (a) Contours for consistency in BOTH L and z. Dark grey = 2σ contour and light grey 3σ contour. (b) Sample 2D distribution from area of consistency in 2σ region $(\alpha_1, \alpha_2, L_b) = (0.15, 2.2, 8 \times 10^{52}$ erg s$^{-1})$. (c) and (d) BATSE and *Swift* LNLP for same parameters as (b).

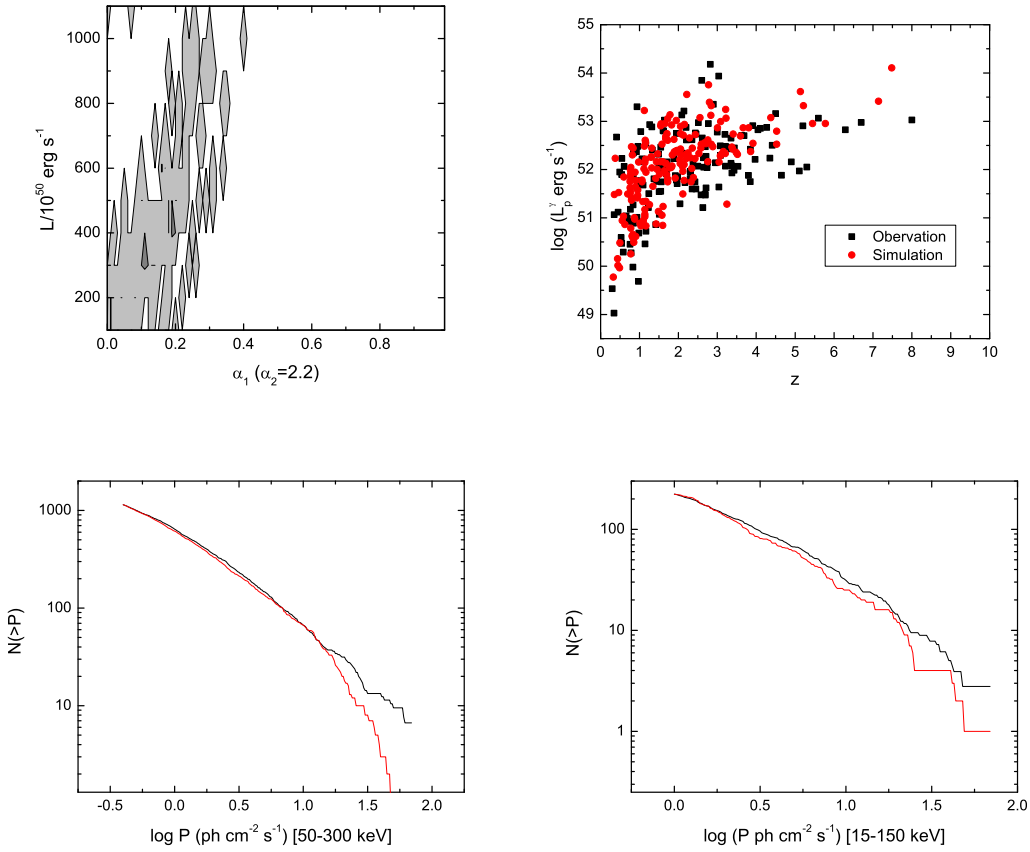

Figure 25 CN SFH model with luminosity break evolution $\propto (1+z)^{1.0}$. (a) Contours for consistency in BOTH L and z. Dark grey = 2σ contour and light grey 3σ contour. (b) Sample 2D distribution from area of consistency in 2σ region. $(\alpha_1, \alpha_2, L_b, \gamma) = (0.05, 2.2, 3\times10^{52}$ erg s^{-1}, 1.0) (c) and (d) BATSE and *Swift* LNLP for same parameters as (b).

Model	L-z? Y/N	LF parameters $(\alpha_1, L_B, \alpha_2)$	z T stat, P-value	L T stat, P-value	Significance z/L	BATSE LNLP T stat, P-value	Sig	*Swift* LNLP T stat, P-value	Sig
GRB rate $\propto$ SFH									
α_2 =2.2									
HB	N	-	-	-	-	-	-	-	-
BL	Y	(0.01,500,2.2)	-0.63727 , 0.51955	1.49613, 0.07869	$1\sigma/2\sigma$	0.92194, 0.13939	2σ	0.18829 0.28273	2σ
	Y	(0.11,600, 2.2)	1.16638, 0.10932	-0.34006, 0.42921	$2\sigma/1\sigma$	0.42551, 0.22537	2σ	0.97859, 0.13178	2σ
	Y	(0.2,900,2.2)	1.4281, 0.0842	-0.33604, 0.428	$2\sigma/1\sigma$	3.72049, 0.01036	3σ	0.95844 0.13444	2σ
CN	N	-	-	-	-	-	-	-	-
PM	N	-	-	-	-	-	-	-	-
GRB rate $\propto$ SFH + Metallicity									
α_2 =2.2									
HB+LN	N	-	-	-	-	-	-	-	-
BL+LN	N	-	-	-	-	-	-	-	-
CN 0.1 cut	N	-	-	-	-	-	-	-	-
HB+LN weighted	Y	(0.11,600,2.2)	0.88134, 0.14509	-0.08952, 0.35632	$2\sigma/1\sigma$	1.973, 0.04921	3σ	0.17974, 0.28485	2σ
	Y	(0.19,1000,2.2)	0.24896, 0.26793	-0.80114, 0.5692	$2\sigma/1\sigma$	0.3929, 0.23235	2σ	0.48579, 0.21293	2σ
	Y	(0.15,800,2.2)	0.29743, 0.25647	-0.4227, 0.45411	$2\sigma/1\sigma$	1.07391, 0.11987	2σ	-0.21968, 0.39359	1σ
BL+LN weighted	N	-	-	-	-	-	-	-	-
CN weighted	N	-	-	-	-	-	-	-	-

Table 3 SFH models and test statistics for a variety of simulations. If consistency is found with the L and z samples, then LF parameters are listed with the outcomes of the LNLP analysis. Later models include the addition of metallicity in the form of the expression from LN, but with a $Z/Z_{\odot} = 0.1$ cut as well as the weighted expression. An 'N' in the significance column indicates that test fails to beyond a 3σ level.

Model	L-z? Y/N	LF parameters $(\alpha_1, L_B, \alpha_2)$	z T stat, P-value	L T stat, P-value	Significance z/L	BATSE LNLP T stat, P-value	Sig	*Swift* LNLP T stat, P-value	Sig
GRB rate $\propto$ SFH									
α_2 = 2.5									
HB	N	-	-	-	-	-	-	-	-
BL	Y	(0.2,1000,2.5)	1.10898, 0.11575	-0.64039, 0.5205	$2\sigma/1\sigma$	1.60564, 0.07058	2σ	2.31001, 0.03562	3σ
	Y	(0.11,600,2.5)	1.16638, 0.10932	-0.09277, 0.35723	$2\sigma/1\sigma$	0.42516, 0.22544	2σ	0.57922, 0.19478	2σ
	Y	(0.09,500,2.5)	1.8598, 0.05495	0.50674, 0.20874	$2\sigma/2\sigma$	0.67752, 0.17715	2σ	0.59479, 0.19189	2σ
	Y	(0.01,600,2.5),	-0.50462, 0.47903	1.62913, 0.06896	$1\sigma/2\sigma$	-0.07208, 0.35145	1σ	-0.02698, 0.33899	1σ
CN	N	-	-	-	-	-	-	-	-
PM	N	-	-	-	-	-	-	-	-
GRB rate $\propto$ SFH + Metallicity									
α_2 =2.5									
HB+LN	N	-	-	-	-	-	-	-	-
BL+LN	N	-	-	-	-	-	-	-	-
CN 0.1 cut	N	-	-	-	-	-	-	-	-
HB+LN weighted	Y	(0.21,600,2.5)	1.55983, 0.07386	-0.17045, 0.37932	$2\sigma/1\sigma$	11.23178, 2.00E-05	N	2.04829, 0.04575	3σ
	Y	(0.29,700,2.5)	1.84368, 0.05582	-0.49454, 0.47596	$2\sigma/1\sigma$	9.747, 8.00E-05	N	0.35612, 0.24042	2σ
	Y	(0.19,1000,2.5)	0.22553, 0.27359	-0.82349, 0.57588	$2\sigma/1\sigma$	0.67135, 0.17822	2σ	0.41201, 0.22824	2σ
	Y	(0.14,800,2.5)	0.35749, 0.24011	-0.23546, 0.3982,	$2\sigma/1\sigma$	2.06092, 0.04519	3σ	-0.42692, 0.45539	1σ
BL+LN weighted	Y	(0.42,800,2.5)	-0.59403, 0.50635	0.01934, 0.32642	$1\sigma/1\sigma$	51.30131, 0	N	5.18583, 0.00318	3σ
	Y	(0.23,400,2.5),	-0.08653, 0.35548	1.13401, 0.1129	$1\sigma/2\sigma$	56.32389, 0	N	6.52096 , 0.00109	N
	Y	(0.5,1000,2.5)	-0.84891, 0.58345	1.22475, 0.10313	$1\sigma/2\sigma$	50.29342, 0	N	11.05363, 3.00E-05	N
	Y	(0.41,600,2.5)	-0.79911, 0.56859	0.57224, 0.19609	$1\sigma/2\sigma$	57.95978, 0	N	7.31417, 0.0005	N
CN weighted	N	-	-	-	-	-	-	-	-

Table 4 SFH models and test statistics for a variety of simulations. If consistency is found with the L and z samples, then LF parameters are listed with the outcomes of the LNLP analysis. Later models include the addition of metallicity in the form of the expression from LN, but with a $Z/Z_{\odot} = 0.1$ cut as well as the weighted expression. An 'N' in the significance column indicates that test fails to beyond a 3σ level.

Model	L-z? Y/N	LF parameters $(\alpha_1, L_B, \alpha_2)$	z T stat, P-value	L T stat, P-value	Significance z/L	BATSE LNLP T stat, P-value	Sig	*Swift* LNLP T stat, P-value	Sig
Models including α evolution (central values)									
HB+LN+α evol	Y	(0.1,800,2.2)	2.85189, 0.02164	-0.61141, 0.51165	$3\sigma/1\sigma$	0.21195, 0.2769	2σ	0.84384, 0.15056	2σ
HB+LN+α evol+weighting (sml scatter)	N	-	-	-	-	-	-	-	-
HB+LN+α evol+weighting (lrg scatter)	N	-	-	-	-	-	-	-	-
BL+LN+α evol	Y	(0.41,900,2.2)	0.19157, 0.28191	-0.37904, 0.44092	$2\sigma/1\sigma$	18.10581, 0	N	1.49981, 0.0784	2σ
BL+LN+α evol+weighting (sml scatter)	Y	(0.39,800,2.2)	1.6878, 0.06507	-0.07309, 0.35173	$2\sigma/1\sigma$	35.23425, 0	N	2.73904, 0.02395	3σ
BL+LN+α evol+weighting (lrg scatter)	Y	(0.39,900,2.2)	0.84106, 0.15097	-0.70235, 0.53937	$2\sigma/1\sigma$			0.74228, 0.16633	2σ
Models including α evolution (upper limit)									
HB+LN+α evol	Y	(0.05,600,2.2)	2.5823, 0.02763	-0.17585, 0.38088	$2\sigma/1\sigma$	4.42284, 0.00585	3σ	0.04375, 0.31989	2σ
HB+LN+α evol+weighting (sml scatter)	N	-	-	-	-	-	-	-	-
HB+LN+α evol+weighting (lrg scatter)	N	-	-	-	-	-	-	-	-
BL+LN+α evol	N	-	-	-	-	-	-	-	-
BL+LN+α evol+weighting (sml scatter)	N	-	-	-	-	-	-	-	-
BL+LN+α evol+weighting (lrg scatter)	N	-	-	-	-	-	-	-	-

Table 5 SFH models and test statistics for models with evolving galactic IMF slope, α, in the metallicity equation of LN. 'sml scatter' and 'lrg scatter' indicate the amount of scatter in the weighting of the metallicity relation. 'central values' and 'upper limits' indicate what set of α values were used in the analysis, those corresponding to the data point value or the upper limits in Figure 22a. An 'N' in the significance column indicates that test fails to beyond a 3σ level.

Model	L-z? Y/N	LF parameters $(\alpha_1, L_B, \alpha_2)$	z T stat, P-value	L T stat, P-value	Significance z/L	BATSE LNLP T stat, P-value	Sig	*Swift* LNLP T stat, P-value	Sig
Rate evolution with z									
GRB rate $\propto$ SFH*$(1+z)^{\delta}$									
δ =0.2									
BL	Y	(0.05,400)	-	-	-	-	N	-	2σ
	Y	(0.18,500)	-	-	-	-	N	-	2σ
	Y	(0.24,800)	-	-	-	-	N	-	2σ
	Y	(0.29,800)	-	-	-	-	N	-	2σ
HB	N	-	-	-	-	-	-	-	-
CN	N	-	-	-	-	-	-	-	-
PM	N	-	-	-	-	-	-	-	-
BL+LN	N	-	-	-	-	-	-	-	-
HB+LN	N	-	-	-	-	-	-	-	-
CN 0.1 cut	N	-	-	-	-	-	-	-	-
BL+LN weighted	Y	(0.54,900,2.2)	-	-	-	-	-N	-	N
	Y	(0.46,700,2.2)	-	-	-	-	N	-	N
	Y	(0.4,500,2.2)	-	-	-	-	N	-	N
	Y	(0.24,400,2.2)	-	-	-	-	N	-	N
HB+LN weighted	Y	(0.54,900,2.2)	-	-	-	-	N	-	3σ
	Y	(0.54,900,2.2)	-	-	-	-	N	-	3σ
CN weighted	N	-	-	-	-	-	-	-	-
δ =0.5									
BL	Y	(0.05,300,2.2)	-	-	-	-	N	-	2σ
	Y	(0.21,600,2.2)	-	-	-	-	N	-	2σ
	Y	(0.33,900,2.2)	-	-	-	-	N	-	2σ
HB	N	-	-	-	-	-	-	-	-
CN	N	-	-	-	-	-	-	-	-
PM	Y	(0.1,500,2.2)	-	-	-	-	N	-	N
	Y	(0.18,800,2.2)	-	-	-	-	N	-	1σ
BL+LN	N	-	-	-	-	-	-	-	-
HB+LN	N	-	-	-	-	-	-	-	-
CN 0.1 cut	N	-	-	-	-	-	-	-	-
BL+LN weighted	Y	(0.33,300,2.2)	-	-	-	-	N	-	N
	Y	(0.43,500,2.2)	-	-	-	-	N	-	N
	Y	(0.51,700,2.2)	-	-	-	-	N	-	N
	Y	(0.59,900,2.2)	-	-	-	-	N	-	N
HB+LN weighted	Y	(0.1,500,2.2)	-	-	-	-	N	-	N
	Y	(0.2,500,2.2)	-	-	-	-	N	-	N
	Y	(0.27,700,2.2)	-	-	-	-	N	-	N
	Y	(0.38,800,2.2)	-	-	-	-	N	-	N
CN weighted	N	-	-	-	-	-	-	-	-

Table 6 SFH models and test statistics for models with rate evolution proportional to $(1+z)^{\delta}$. An 'N' in the significance column indicates that test fails to beyond a 3σ level. These models are not favored by the BATSE, and in some cases *Swift*, LNLP data.

Model	L-z? Y/N	LF parameters $(\alpha_1, L_B, \alpha_2)$	z Stat, P-value	L Stat, P-value	Significance z/L	BATSE LNLP T stat, P-value	Sig	*Swift* LNLP T stat, P-value	Sig
Rate evolution with z GRB rate $\propto$ SFH$*(1+z)^{\delta}$ δ =0.8									
BL	Y	(0.04,300,2.2)	-	-	-	-	N	-	2σ
	Y	(0.09,400,2.2)	-	-	-	-	N	-	2σ
	Y	(0.28,600,2.2)	-	-	-	-	N	-	2σ
	Y	(0.4,800,2.2)	-	-	-	-	N	-	N
HB	N	-	-	-	-	-	-	-	-
CN	N	-	-	-	-	-	-	-	-
PM	Y	(0.24,700,2.2)	-	-	-	-	N	-	N
	Y	(0.36,1000,2.2)	-	-	-	-	N	-	N
BL+LN	N	-	-	-	-	-	-	-	-
HB+LN	N	-	-	-	-	-	-	-	-
CN 0.1 cut	N	-	-	-	-	-	-	-	-
BL+LN weighted	Y	(0.43,300,2.2)	-	-	-	-	N	-	N
	Y	(0.52,500,2.2)	-	-	-	-	N	-	N
	Y	(0.61,600,2.2)	-	-	-	-	N	-	N
HB+LN weighted	Y	(0.14,400,2.2)	-	-	-	-	N	-	N
	Y	(0.25,600,2.2)	-	-	-	-	N	-	N
	Y	(0.32,700,2.2)	-	-	-	-	N	-	N
	Y	(0.39,900,2.2)	-	-	-	-	N	-	N
	Y	(0.44,900,2.2)	-	-	-	-	N	-	N
CN weighted	N	-	-	-	-	-	-	-	-

Table 7 SFH models and test statistics for models with rate evolution proportional to $(1+z)^{\delta}$ (continued). An 'N' in the significance column indicates that test fails to beyond a 3σ level. These models are not favored by the BATSE, and in some cases *Swift*, LNLP data.

Model	L-z? Y/N	LF parameters $(\alpha_1, L_B, \alpha_2)$	z T stat, P-value	L T stat, P-value	Significance z/L	BATSE LNLP T stat, P-value	Sig	*Swift* LNLP T stat, P-value	Sig
LF break evolution									
$L_B \propto L_B * (1+z)^\gamma$									
γ =1.0									
HB	Y	(0.15,500)	2.77368 , 0.02321	-0.37816, 0.44065	3σ/ 1σ	8.98113, 0.00015	N	2.04678, 0.04582	3σ
CN	Y	(0.05,300)	0.9696, 0.13296	-0.66268, 0.5273	2σ/ 1σ	0.13296, 0.29664	2σ	-0.00699, 0.33353	1σ
	Y	(0.09,400)	1.33265, 0.0926	-0.49987, 0.47758	2σ/ 1σ	2.86931, 0.0213	3σ	0.64614, 0.18262	2σ
	Y	(0.23,500)	2.99502, 0.01906	0.24022, 0.27003	3σ/ 1σ	-0.59966, 0.50807	1σ	0.50419, 0.20924	2σ
	Y	(0.23,800)	1.94944, 0.05035	1.81983, 0.05714	2σ/ 2σ	9.08464, 1.40E-04	N	1.49638, 0.07867	2σ
	Y	(0.16,600)	0.97282, 0.13253	-0.03763, 0.34191	2σ/ 1σ	6.35583, 0.00124	N	2.12331, 0.04256	3σ
γ =1.1									
CN	Y	(0.13,300)	1.1944, 0.1063	-0.60168, 0.50868	2σ/ 1σ	-0.10903, 0.36181	1σ	0.31854, 0.25158	2σ
γ =1.2									
HB	Y	(0.12,300)	3.43185, 0.01311	-0.86134, 0.58714	3σ/ 1σ	5.13402, 0.00331	3σ	0.90169, 0.14221	2σ
CN	Y	(0.23,500)	1.63419, 0.06861	1.25677, 0.09989	2σ/ 2σ	3.68355, 0.01067	3σ	0.32701, 0.24697	2σ
	Y	(0.08,200)	1.66239, 0.06672	-1.02453, 0.63452	2σ/ 1σ	-0.58847, 0.50465	1σ	1.26917, 0.09866	2σ
γ =1.3									
CN	Y	(0.12,200)	1.33772, 0.09214	-0.33412, 0.42743	2σ/ 1σ	-0.65832, 0.52597	1σ	0.1113, 0.3022	2σ
γ =1.4									
CN	Y	(0.17,300)	1.61382, 0.07001	0.82904, 0.15277	2σ/ 2σ	1.65549, 0.06718	2σ	1.00256, 0.12868	2σ
γ =1.5									
CN	Y	(0.23,200)	1.73898, 0.06187	0.60585, 0.18986	2σ/ 2σ	-0.82308, 0.57576	1σ	0.14452, 0.2937	2σ

Table 8 SFH models and test statistics for models with evolution of the luminosity function break luminosity, L_b. An 'N' in the significance column indicates that test fails to beyond a 3σ level.

CHAPTER 5

TYPE I V. TYPE II

Early observations began hinting at the possibly dual nature of the observed sample of GRBs [245, 246], culminating in the study of over 200 BATSE bursts in 1993 [160] that clearly demonstrated the (at least) bimodal distribution in hardness and duration (see Figure 10). The goal of connecting the observational properties of GRBs to the type of intrinsic progenitor that powers the central engine has had a long history and is still hotly debated and not fully understood. This ties deeply with to classification of bursts and has implications in understanding the properties of different progenitors. Classification is the context in which I frame the contribution of this portion of the work, testing whether the merger model for GRB progenitors is consistent with the observations of short-hard GRBs. This chapter is based on the analysis presented in [247].

Classification

Before the advent of afterglow observations of short-hard bursts, the clean picture of long-soft GRB = collapse of massive star and short-hard GRB = merger of two compact stellar objects was widely accepted and generally taken as fact. One of the bases for this argument was the bimodal distribution in the hardness and duration space [160], which shows broad distributions loosely separated at ~ 2 seconds, possibly indicating different progenitors. The scatter in the distribution, however, might cause contamination between populations. Something must be causing the observed dual nature, but perhaps the direct correlation between duration-hardness and intrinsic progenitor is too simplistic. Some studies even consider the possibility of a third population of intermediate bursts [248, 249, 250]. Other observations, such as host galaxy associations (e.g. [251, 252, 253, 254, 101, 255, 256, 258]), 'short' bursts with long tails of extended emission [253, 101, 259, 260] and especially the short rest-

frame duration of some GRBs (e.g. GRB 060614B; [261, 262]) prompted Zhang *et al.* [163, 164] to look deeper into the issue of classification and attempt to find a connection between the observations and progenitors of GRBs. By looking into a variety of observational properties, they propose a scheme that separates bursts into Type I or Type II, with the former related to compact stellar objects (e.g. mergers) and the latter related to the collapse of massive stars (e.g. collapsar). Below, I summarize key results from these papers relating to the observational properties of GRBs and how they fit into the picture of classification. Another possible scheme that is not covered here can be found in Bloom *et al.* [263].

- Duration

  If the duration of the burst, T_{90}, is related or proportional to the duration of the central engine, as is assumed in most works, this value would give information about the type of progenitor that powers the GRB. In the paradigm of the collapsar model [264], the BH-torus system that is created has abundant material from the stellar envelope for accretion. The timescale for such a process is considered to be the fallback timescale of the collapsing envelope, which is on the order of 10s of seconds. In NS-NS and NS-BH mergers, there is much less material available for the ensuing BH-torus system. In the case of two NS, this value is just about 3 $M_{\odot}$, since both objects must be below the Chandrasekhar limit and are fully evolved, having ejected their stellar envelopes through stellar winds and in a likely SN explosion. The explosion is also thought to impart kicks to the system that further removed them from their natal material [265]. The timescale for accretion of the latter model is on the order of $\sim$ 0.01-0.1 seconds, shorter than any observations of any short GRB. Additional aspects are needed to increase the timescale, perhaps of the form of an intermediate NS phase [266].

  Accretion timescales are based on the activity of the central engine, and the

estimates above are for one and only one episode of central engine activity. *Swift* observations of a variety of bursts show randomly placed flares in the x-ray lightcurves (see §'X-ray emission') which likely indicate continued activity from the central engine, occurring in both long and short bursts. In addition, some short bursts, including strong Type I candidates, have been observed with long lasting and softer 'extended emission' [253, 101, 259], making these often described 'short' bursts not short at all.

- Hardness

  The hardness of a GRB spectrum is not as clearly tied to the properties of the progenitor but rather has more to do with the dissipation and radiation processes that are generally unknown. For a Band function spectrum [166], the critical values are likely the placement of the peak spectral energy and perhaps, to a lesser extent, the lower energy spectral index, which changes depending on the model assumptions (e.g. internal shocks, photosphere emission [267]). Different constraints are derived in Zhang *et al.* [164] but a clear connection remains elusive.

- Supernova association

  A supernova association with a GRB is confirmation of its connection with a massive stellar collapse and of the Type II class. A handful of bursts have been observed to have supernova associations, most notably GRB 980425-SN 1998bw [139, 140], but there are of course exceptions. Detection of a SN (Figure 9) component requires ground-based optical follow-up which can be hampered by a multitude of factors. Considering that GRBs occur at cosmological distances, it is possible that a supernova with a redshift of $z \gtrsim 1$ will not be detectable. It has also been argued that GRBs may not have the capacity to create a sufficient amount of ^{56}Ni required to produce the observed optical emission

[37, 268, 269, 270] seen in SN. Even with these potential problems, strict upper-limits on the optical flux from a variety of short GRBs (see [271] and references therein) were taken as further evidence that short GRBs are different from their long counterparts. Once again, additional observations led to a challenge of this view, specifically with GRBs 060614 and 060505, very local (i.e. a SN signature should be easily detected if it is there) long bursts ($\sim$ 100 seconds; [272]) *without* a SN detection. A SN association clearly demonstrates that a burst is part of the Type II category, but likewise a non-detection can often mean that the progenitor is likely of Type I origin, especially if this is combined with other supporting evidence of the class.

- Host galaxy observations

  Properties of the associated host galaxies of GRBs can also lead to inference about the type of progenitors. Bursts associated with massive stars should reside in star-forming galaxies or in star-forming regions within a galaxy. The star-forming rate, or star forming rate per unit mass, should be a telling sign of association with this class. Type I bursts, on the other hand, can be associated with any type of galaxy [273, 274], since many models argue for a long-lived progenitor system that would outlive the original star-forming episode that gave rise to the progenitor or possibly live long enough to see a subsequent round of star-formation in the galaxy. One could also observe a Type I GRB in a star-forming region if one considers a significant fraction of short delay merger events [273, 274, 275]. Only two bursts (GRB 050509 [251] and 050724 [101, 255]) show a clear association with an early-type elliptical host, indicating that these associations are not very common. Studies (e.g. [258, 276]) show that most short GRBs occur in galaxies with ongoing star formation. Energetics issues also provide evidence that perhaps some short GRBs at higher redshifts are actually Type II GRBs [164]. Some merger models predict natal 'kick' velocity associated

with some compact object mergers, which, over the lifetime of the system, could produce significant offset from the host galaxy [265]. This property has been observed and analyzed in a variety of short GRBs [251, 252, 255, 101, 256, 260, 277]. This argument ties in to the difficulties of accurately determining the host galaxy associated with the GRB, especially if multiple galaxies exists within the error circle of the detector or the GRB location is significantly offset from a galaxy where one could argue a fainter, higher-z galaxy is the actual host [257, 258].

- Spectral lag

  Spectral lag is a characteristic of GRB spectra where harder photons arrive at the detector faster than softer emission. This has been observed in various long GRBs [278, 261, 91] but is generally negligible for short GRBs [259, 279]. This phenomenon has been attributed to the differences in observational times of photons from higher latitudes from the line of sight [280, 281, 282, 259, 283]. It is unclear as to how much information about the progenitor is actually given in the spectral lag, although it is more likely that the lag is related to the pulse width rather than any real connection to the type of progenitor.

- Redshift distribution and luminosity function

  This is the main focus and contribution of this work and will be detailed in the following section.

Utilizing these and a few additional criteria, Zhang *et al.* [164] tailored a general classification scheme that aims at identifying the intrinsic progenitor of a GRB, coming to the conclusion that previous definitions (i.e. < 2 seconds vs. > 2 seconds) are insufficient and likely misidentify bursts. A schematic of the classification system can be found in Figure 26. The scheme is complicated and allows for a variety of channels between secure Type I and Type II bursts as well as Type I and Type II

candidates. In addition, Zhang *et al.* [164] is meant to highlight the entangled nature of the observations and is not meant to be an 'end all and be all' in terms of classification. In general, the work was motivated by two high-z bursts, GRBs 080913 (z=6.7 [157]) and 090423 (z=8.3 [159, 158]) which they believe, after considering the various observational constraints, are intrinsically short hard GRBs that are of Type II, or massive star, origin. A robust analysis can be found in Zhang *et al.* [164], while a detailed follow-up analyzing all the short GRBs and their likely progenitors as derived from this classification scheme can be found in Kann [271].

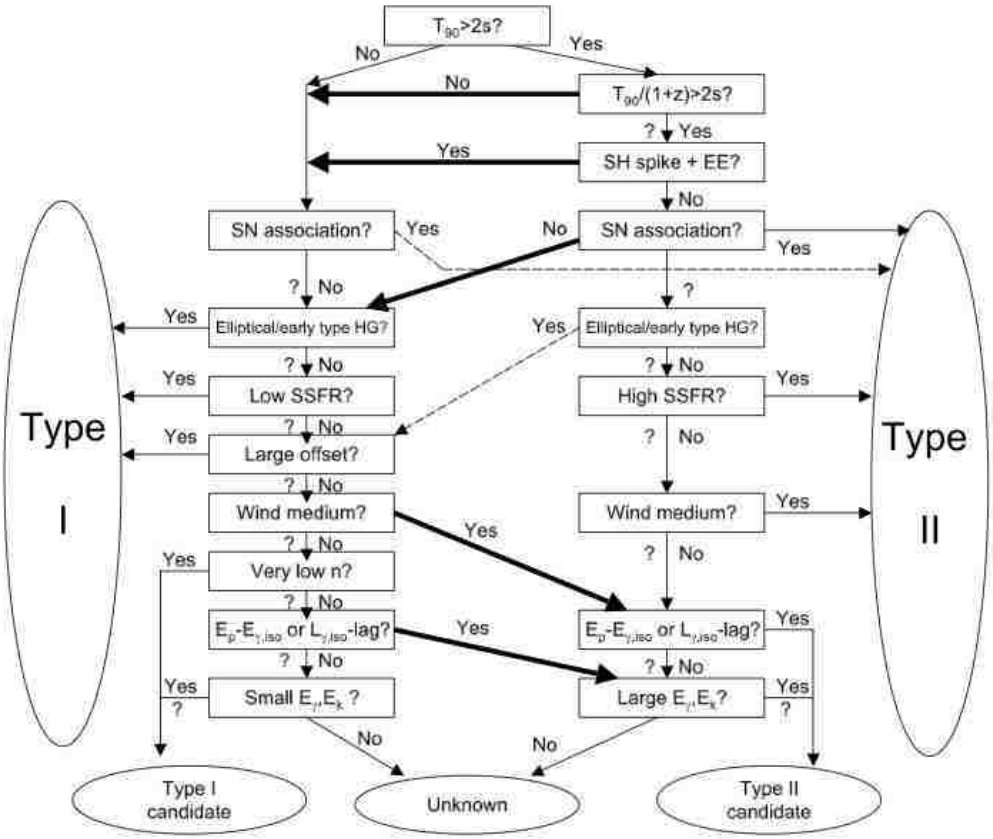

Figure 26 Classification scheme proposed by Zhang *et al.* [164] that attempts to predict the intrinsic progenitor from multiple observational criteria.

The issues highlighted above are the context in which this work is based, with the explicit goal of determining *if all short GRBs are of Type I origin*. Note that 'short GRBs' alludes to the observational properties of those bursts that are believed to be of merger origin, while 'Type I' gives information about the intrinsic progenitor. Specifically, I endeavor to answer the question of whether the merger model can stand up to the observations of short GRBs and what the implications of these constraints are to the nature of the progenitor that powers them.

Testing the merger model

A variety of works have been conducted that focus on constraining merger models with the available observations of short GRBs utilizing a variety of methods [284, 285, 286, 287] (see [161] for a review). Even with these studies, the specifics of Type I bursts are loosely constrained, largely due to the small sample of short GRBs. The most important distributions are the luminosity function and the merger delay timescale, τ, which is defined as the time elapsed between the epoch of star-formation that gave rise to the binary system and the eventual coalescence of the compact stellar remnants (e.g. NS-NS, NS-BH) via gravitational radiation. Most values for τ in the literature are a long delay from star formation, on the order of $1 - 6$ Gyr or a distribution that is proportional to a power γ of the merger time delay τ [284, 285, 286, 287]. Suggestions by Nakar *et al.* [286] include a constant merger time delay, with moderate scatter, of approximately 4 Gyr or a distribution that follows $\tau^{-0.5}$ or shallower, while Guetta *et al.* [287] claim a constant delay on the order of a few Gyr or a logarithmic delay based on assumptions of the initial separations of the orbits of the two objects. Observations of short GRBs at higher redshift [257, 288] are difficult to reconcile within this framework.

A potential solution to the problem lies in population synthesis studies, such as [289, 290, 273, 291, 292, 293, 294]. Their argument suggests that merger timescales

are not solely restricted to 'classical' timescales [295] but may include channels for the formation of ultra-compact binary systems that merge promptly (e.g. a few 10s Myr). The established method for creating binary systems of compact objects is summarized as follows (see also Figure 27 and [291]). If one begins with a binary system composed of two massive stars of masses M_1 and M_2 (with $M_1 > M_2$), the more massive star will, within a few Myr, begin to evolve off the main sequence, expanding to fill its Roche lobe before it begins to fuse helium in its core. Once the Roche lobe is filled, the first episode of mass transfer, from star 1 to star 2 will begin through the shared Lagrangian point. Eventually, the massive star will begin fusing He, leaving a He-star and massive main sequence star system. This is quickly followed by a Type Ib-c supernova of the He star resulting in the first compact stellar object. Next, the less massive star begins to evolve off the main sequence, also going through a giant phase and providing the mechanism for the second mass transfer event, this time onto the stellar remnant. This episode removes the envelope of the second star, causing a loss of angular momentum in the system. At this point, we are left with a He star orbiting a compact remnant, and this is where the theory for 'classical' and 'new' formation channels diverge. In the classical model, the 2^{nd} He star undergoes a Type Ib-c SN explosion, leaving two compact stellar objects in a relatively wide orbits that merge in times greater than 100 Myr. If instead we have a relatively low-mass (roughly 2-3 $M_{\odot}$) He star, it will proceed to fill its Roche lobe for a third episode of mass transfer, and possible common envelope phase before the SN explosion, leaving an ultra-compact orbit of the final system. This physical mechanism leads to the differences in merger timescales and provides a large population of short merger timescales that might be the solution to the observed high-z short GRBs.

The luminosity function of Type I GRBs is only loosely constrained, generally considered to be of the form of a power-law or broken power-law [286, 285, 287]. Nakar *et al.* [286] claim a very steep power law luminosity function fit, with index of roughly

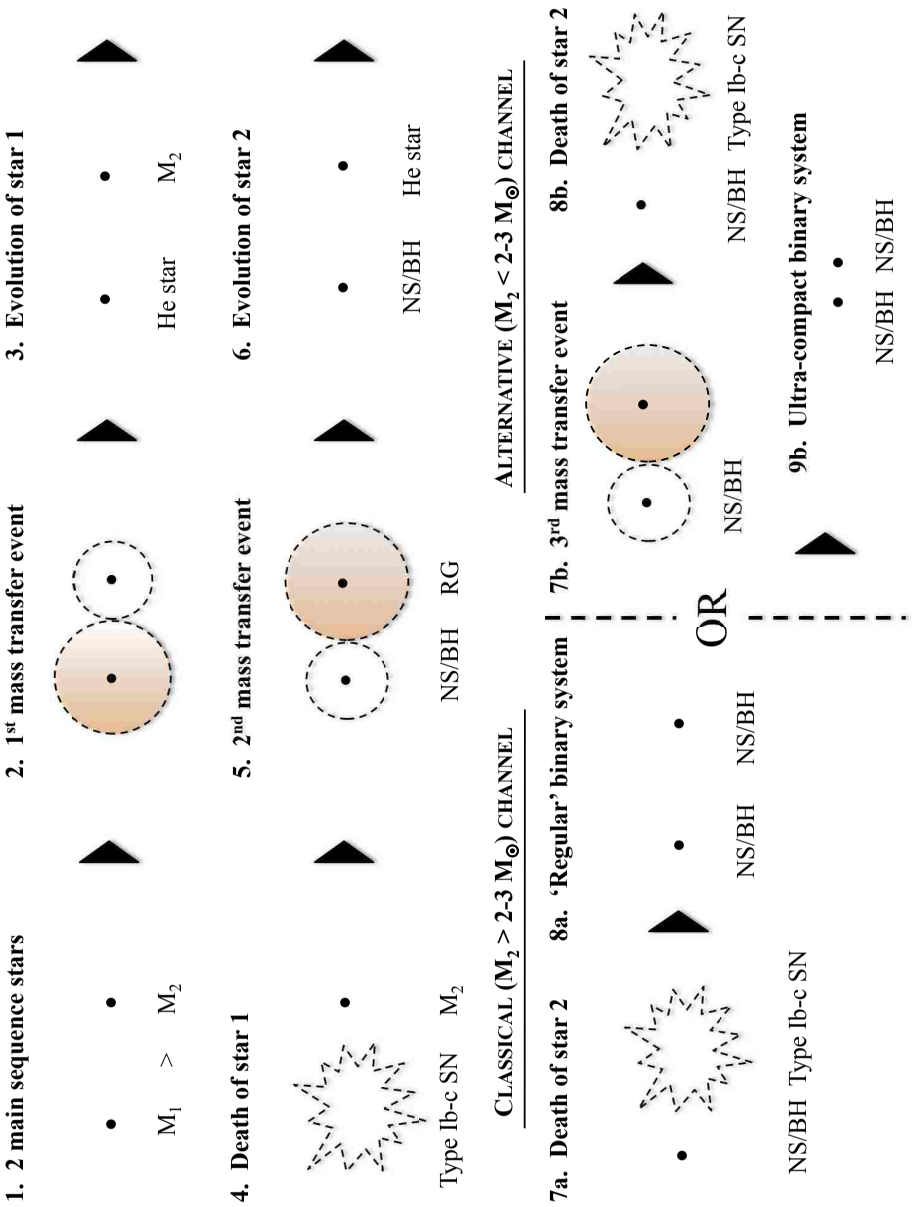

Figure 27 Diagram detailing the process of creating regular and ultra-compact binary systems of compact stellar remnants. Dashed circles designate the Roche lobes for the objects.

-2, while Guetta *et al.* [287] argue for a broken PL with pre-break slope ~ -0.5 and post-break slopes ranging from -1 to -2. Both works stress that the sample of bursts is small and that they allow for flexibility in assigning rates, delay distributions and luminosity function models. The current sample of short bursts is now larger, although only about 18 bursts, depending on how the sample is defined. Other types of LF models have been proposed, such as a dual-peak luminosity function to account for soft gamma-ray repeater (SGR) giant flares [297, 298] or contributions to Type I GRBs from events occurring in globular clusters [296, 299]. These associations and contributions are considered to be either negligible [300] or without substantial evidence for their existence, therefore, we do not consider these types of models in our analysis.

Simulations

As in the analysis of HL and LL bursts, we conduct several sets of simulations with a similar method described in Chapter 2. The major differences include the treatment of the merger time delay, which was unnecessary in the previous work, and updated statistics as used in the high-z analysis of Chapter 4.

We first assume that the Type I GRB luminosity function is a broken PL (Equation 2.4), similar to that of Type II bursts as well as the models presented in the literature. Using the observed samples, we attempt to constrain the slopes and break in this distribution. The GRB rate, on the other hand, is a convolution of the SFH and the distribution of merger time delays, τ. We address several models:

- Constant merger time delay with dispersion

  A constant delay from the SFH for all bursts, ranging from 1-5 Gyr with a Gaussian scatter with standard deviation σ of 0.3 or 1.0. This type of delay is likely not related to the true delay of compact object mergers but is frequently discussed in the literature and may indicate different types of progenitors.

- Logarithmic delay

  An empirical form proposed by Guetta *et al.* and Nakar *et al.* [287, 286] with $P(\log\tau)d\log(\tau) \sim$ const, which implies $P(\tau) \sim 1/\tau$.

- Delay distribution from standard population synthesis

  A distribution given by the predications of the population synthesis codes of Belczynski *et al.* [292] including both NS-NS and NS-BH mergers. Utilizing data provided by the authors, we fit the distribution by a 5^{th} order polynomial and use the model in our numerical simulations. This model has a long tail of merger time delays up to near the Hubble time as well as a significant fraction of prompt ($\lesssim$ 100 Myr) merger events. (see Figure 28)

- 'Twin' model from population synthesis

  A second population synthesis model from Belczynski *et al.* [291]. These simulations incorporate the effects of twin binaries, defined as binaries with objects of roughly equal mass. This model is similar to the standard population synthesis model with the exception that this model predicts nearly 70% prompt (shorter than 100 Myr) merger events whereas the latter predicts roughly 40%. We extract the data from the reference and fit it similarly to the standard population synthesis model.

We also consider two further models that imply an association with Type II GRBs since, as presented below, we find it difficult to reconcile the observed data with the previous models.

- No delay - Type II

  In this model, short GRBs are assumed to follow the cosmic SFH. Two variations on this model are considered. (i) All bursts are assumed to be the same population as regular, high-luminosity GRBs. Therefore, we sample from that

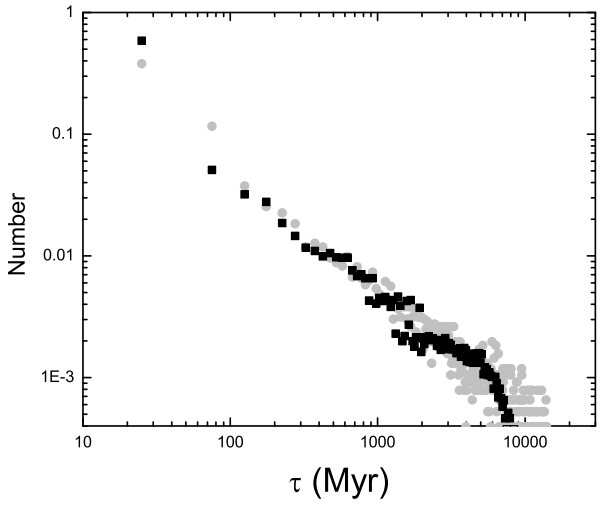

Figure 28 A comparison of the simulated merger delay time distributions between the standard population synthesis model (Belczynski et al. 2010 [292], grey) and the "twin" population synthesis model (Belczynski et al. 2007 [291], black). Note the higher fraction of prompt mergers in the twin model.

luminosity function (as constrained above and in Liang *et al.* and Virgili *et al.* [185, 178]) with a rate proportional to the SFH. (ii) The luminosity function of short GRBs is unknown and we constrain the parameter space akin to the other models, once again assuming a rate proportional to the SFH.

- Mixed Type I/Type II distribution

  This model assumes that the distribution of short GRBs is sampled from a superposition of Type I bursts, whose luminosity function we wish to constrain, and classical HL GRBs. For the merger events, the time delay distribution is sampled from the population synthesis models [291, 292]. The fraction of bursts from each type is a free parameter that can be constrained from the data.

The value of the merger time delay is given in units of Myr and must be related to the redshift of a burst. In the simulations, every iteration begins with a luminosity

and redshift pair, (L, z). In this study, this redshift is the redshift of the epoch of star formation that gave birth to the binary system, $z_{creation}$, and is given by Equation 3.2. The time delay must be added to this value to give the redshift of the GRB, z_{GRB}, and is incorporated by use of the look-back time equation for a flat universe

$$\int_0^{z_{creation}} t(z)dz = \int_0^{z_{creation}} \frac{1}{H_0} \frac{1}{(1+z)(\Omega_m(1+z)^3 + \Omega_\Lambda)^{0.5}}. \tag{5.1}$$

Using this equation, the look-back time of $z_{creation}$, or the time that has elapsed since that redshift, is calculated, and the merger time delay is subtracted. The new look-back time, corresponding to the time when the GRB actually occurred, is then converted back to a redshift via the same equation. Bursts that have a negative look-back time (i.e. those that have not yet occurred) are discarded. Figure 29 shows how the redshift distribution, including the effects of the comoving volume and cosmological time dilation, are affected by the merger time delay for a variety of models. These figures show the relative changes in these distributions. The last deviation from the theory presented in Chapter 2 deals with the detector trigger threshold. The threshold still follows from Equation 3.3 but the T_{90} distribution is sampled randomly from the normal distribution based on BATSE statistics of short GRBs, namely $T_{90}^{short} = 0.33 \pm 0.21$ s.

The observed sample of GRBs consists of 18 GRBs that, according to the multiple criteria summarized by the classification scheme of [164], are the best Type I candidates. Their redshifts and luminosities are summarized in Table 9 and shown graphically in Figure 30. We assume that the presented redshift values are correct, although there is the possibility for chance coincidences [301]. In addition, some studies [257, 258] indicate the possibility of more short GRBs at higher redshifts. This would only strengthen the conclusions presented here, namely that a significant fraction of Type I GRBs should trace the star-formation history.

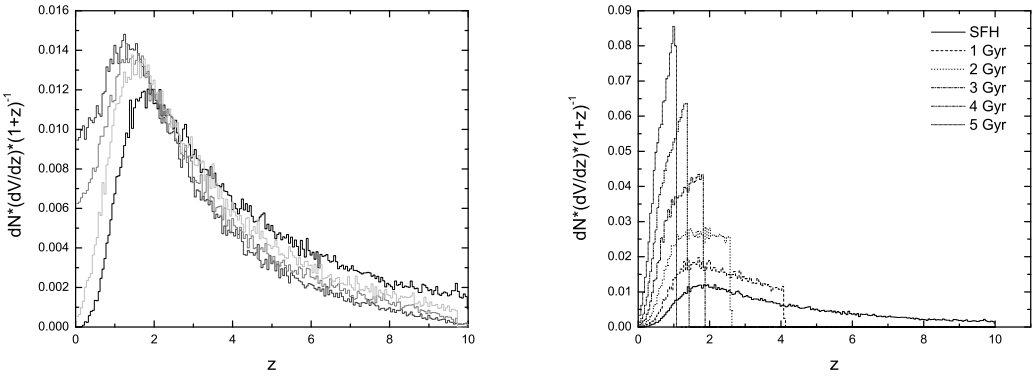

Figure 29 Modified GRB redshift distributions (Equation 2.1 integrated over L) including the effects of cosmological time dilation and the comoving volume element, dV/dz. Different curves correspond to different models, invoking different merger delay timescale distributions. The left panel shows a model that follows the star formation history (i.e. no merger time delay; black) as well as the population synthesis (standard, gray; twin, light gray) and logarithmic (dark gray) models. The right panel shows various constant delay models as compared with the no delay model. All histograms contain the same number of bursts and show the relative effects across models.

We utilize the K-S test to test for consistency with the luminosity and redshift distributions, creating contours similar to those of Chapter 3, which indicate the overlap in regions of the $L_b - \alpha_1$ parameter space that show significant consistency in both the L and z samples. The k-sample Anderson-Darling test is utilized for both the *Swift* and BATSE LNLP distributions with many of the same assumptions as detailed in Chapter 4, with the only difference being the selection of bursts below the 2 second delimiter for short bursts versus long bursts [224]. Table 10 presents a summary of the model parameters and test statistics (with P-values) for all the models tested.

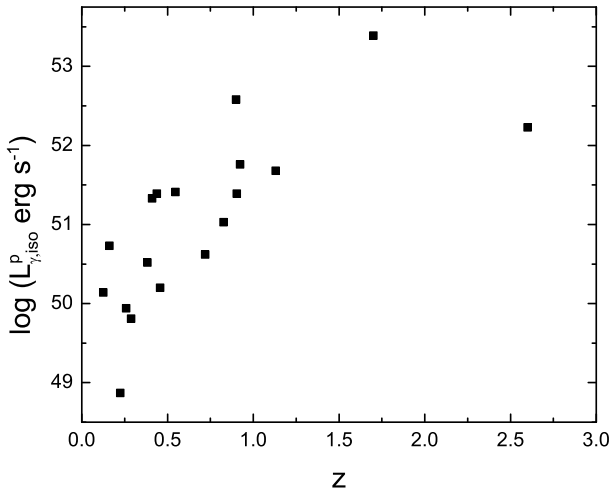

Figure 30 Sample of the z-known short-hard GRBs detected in the *Swift* era. The redshifts are plotted against peak isotropic gamma-ray energy, L. This distribution is used to constrain luminosity function of various redshift distribution models.

Results

Utilizing the theoretical framework above, we summarize our results organized by merger timescale model.

Constant merger time delay (with dispersion)

This set of simulations includes tests of merger time delays with values $\tau = 1, 2, 3, 4, 5$ Gyr, each with a Gaussian scatter of either $\sigma = 0.3$ or 1.0 around this central value. Most NS-NS models are based, at least in part, on observations of Galactic NS-NS binaries, all of which imply a merger time on the order of, or larger than, the Hubble timescale. A realistic model should include a distribution including a tail that allows for such long-lived events. These models are likely not realistic in this framework but are an important facet of the literature as well as having potential implications to the type of progenitor.

GRB name	z redshift	$L_{\gamma,iso}^{peak}$ 10^{50} erg s^{-1}
050509B	0.2248	$0.07^{+0.10}_{-0.05}$
050709	0.1606	$5.4^{+0.67}_{-0.69}$
050724	0.2576	$0.99^{+0.23}_{-0.10}$
060614	0.1254	$1.39^{+0.13}_{-0.07}$
061006	0.4377	$24.60^{+1.22}_{-0.77}$
050813	0.72	4.13 ± 2.02
051221A	0.5464	25.8 ± 0.9
060121[a]	1.7	2445 ± 162
060121	4.6	33574 ± 2226
060502B[b]	0.287	0.65 ± 0.09
060801	1.131	$47.6^{+6.2}_{-1.6}$
061210	0.4095	21.5 ± 1.4
061217	0.8270	10.8 ± 1.8
070429B	0.9023	24.6 ± 3.8
070714B	0.9225	57.3 ± 3.6
070724A	0.457	$1.58^{+0.34}_{-0.14}$
071227	0.3940	3.34 ± 0.49
090426	2.6	171^{+24}_{-44}
090510	0.9	376^{+186}_{-172}

Table 9 Type I sample. Luminosities derived by author unless otherwise specified. References for redshift measurements: **GRB 050509B**: [251], [256], [302]; **GRB 050709**: [252],[303],[304]; **GRB050724**: [305], [304]; **GRB 060614**: [306]; **GRB 061006**: [257]; **GRB061006**: [257]; **GRB 050813**: [304]; **GRB 051221A**: [307]; **GRB 060121**: z=1.7: [308], [257], z=4.6: [309]; **GRB 060502B**: [310]; **GRB 060801**: [311], [257]; **GRB 061210**: [257]; **GRB 061217**: [257]; **GRB 070429B**: [312]; **GRB 070714B**: [288], [312]; **GRB 070724A**: [313], [258], [314]; **GRB 071227**: [315],[258]; **GRB 090426**: [316]; **GRB 090510**: [317], [318]; [a] We chose z=1.7 for this analysis; [b] Derived from $\frac{E_{\gamma,iso}}{T_{90}}$. T_{90}: [319], $E_{\gamma,iso}$: [320]

Except for the 1-2 Gyr models, all other merger time-delays demand a very shallow pre-break slope (α_1) of the luminosity function to account for the $L - z$ constraints. When all the distributions are folded, together this makes the BATSE LNLP very shallow and inconsistent with the data. This is largely due to the effect of long merger time delays that push the redshift distribution to very recent redshifts (Figure 29), causing the shape of the luminosity function to have a large effect on the LNLP (Figures 31 and 32). Type II bursts do not have this problem, as their redshift distribution is spread out over a large span of redshift, in effect washing out the effects of the LF. The *Swift* constraints to the LNLP are more forgiving, showing consistency for models with 1-4 Gyr delays. Combining constraints from all the tests, we conclude that only the 2 Gyr model is consistent with the data. A breakdown of the tests is shown in Figure 33 and statistical results summarized in Table 10.

Logarithmic and population synthesis

Population synthesis models [291, 292] allow for a more realistic picture of merger time delays since they include a variety of delays, including a tail to very long time delays as expected from observations of Galactic NS-NS binary systems. The logarithmic and standard population synthesis models have similar results and are addressed together.

The implied luminosity function slopes are very shallow, on the order of -0.2 or larger, and are needed so as to not overproduce low-z low-L GRBs (Figure 34). These slopes, however, severely overproduce high-photon flux bursts and therefore cause the LNLP to also be very shallow (Figures 31 and 32). Both of these models are not favored by either the BATSE or *Swift* short GRB data.

The 'twin' population model is an alternative model that allows for an even larger fraction (70% as compared to 40% of the standard populations synthesis model) of prompt mergers from binaries with similar sized stars. By removing a fraction of

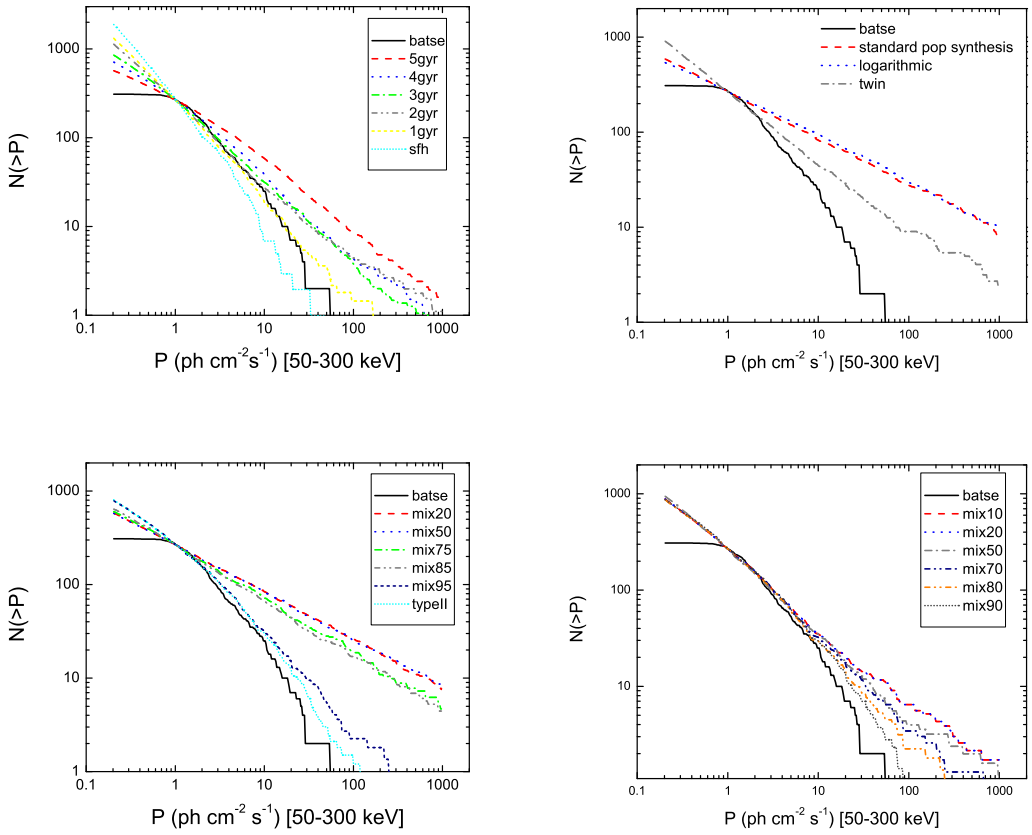

Figure 31 Comparison of the $\log N - \log P$ distributions for the various models with the observed BATSE curve. (a) various constant delay merger models ($\sigma = 0.3$ are shown. Curves for $\sigma = 1.0$ are similar and therefore not included in the figure); (b) the standard population synthesis, logarithmic and twin models. (c) mixed models with classical Type II's (with long Type II luminosity function) and Type I's with standard population synthesis time delay distribution; (d) mixed models with classical Type II's and Type I's with time delay distribution predicted by the "twin" population synthesis model. The notation "mix20" stands for 20% Type II (and 80% Type I) for both panels (c) and (d). Few models pass the BATSE constraints, with the exception of: (1) the 2 Gyr model (both $\sigma = 0.3$ and 1.0); and (2) the 30% and 40% Type II-twin mix models. See Table 10 for test statistics and P-values for various models.

the long delays, this model is expected to perform better in the tests. The $L - z$ constraints show consistency with slightly steeper LF slopes, which implies a steeper LNLP slope. The improvement is sufficient to show consistency with the *Swift* sample but is not enough to show consistency with the BATSE sample. This implies that

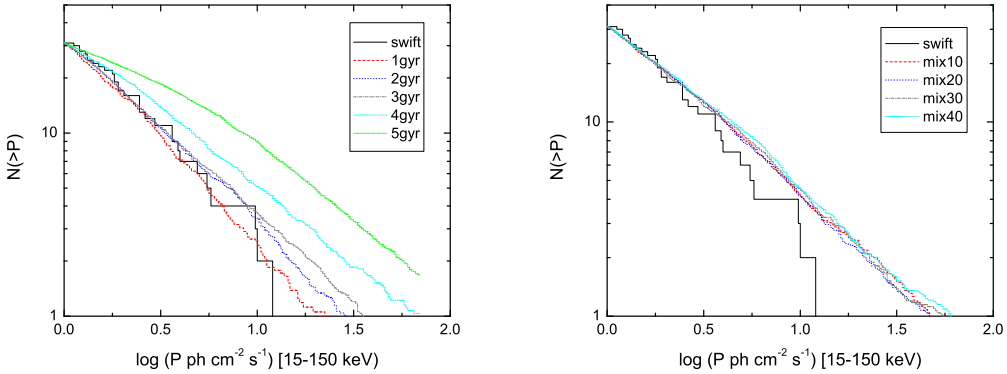

Figure 32 $\log N - \log P$ distributions for the observed *Swift* sample and the simulated bursts in the *Swift* (15-150 keV) band. Unlike the BATSE constraints, this test gives consistency for many more models, and we present the most relevant ones here. The first panel shows constant merger models ($\sigma = 0.3$), and the second shows various mixed models with the "twin" population synthesis time delay model.

alone, this model also cannot adequately reproduce the observations.

No delay (Type II)

As demonstrated in the analysis above, the hypothesis that "all short GRBs detected by BATSE and *Swift* are of merger origin" is clearly not justified, and the data demands the serious consideration of alternative models. In the most extreme case, it is possible that the observed short GRB population is just a subpopulation of Type II bursts and can manifest itself in two forms. First, the bursts follow the same redshift distribution that is proportional to the SFH but have a different luminosity function. This approach to testing this model is similar to previous models where the luminosity function parameter space is tested for consistency with the L and z sample (Figure 34). The slope implied by the observations is very steep ($\alpha_1 \sim 1.42$) and shows consistency with the observations, albeit at a very low level ($\sim 20\%$). The LNLP is too steep compared to the observations and inconsistent with both the BATSE and *Swift*

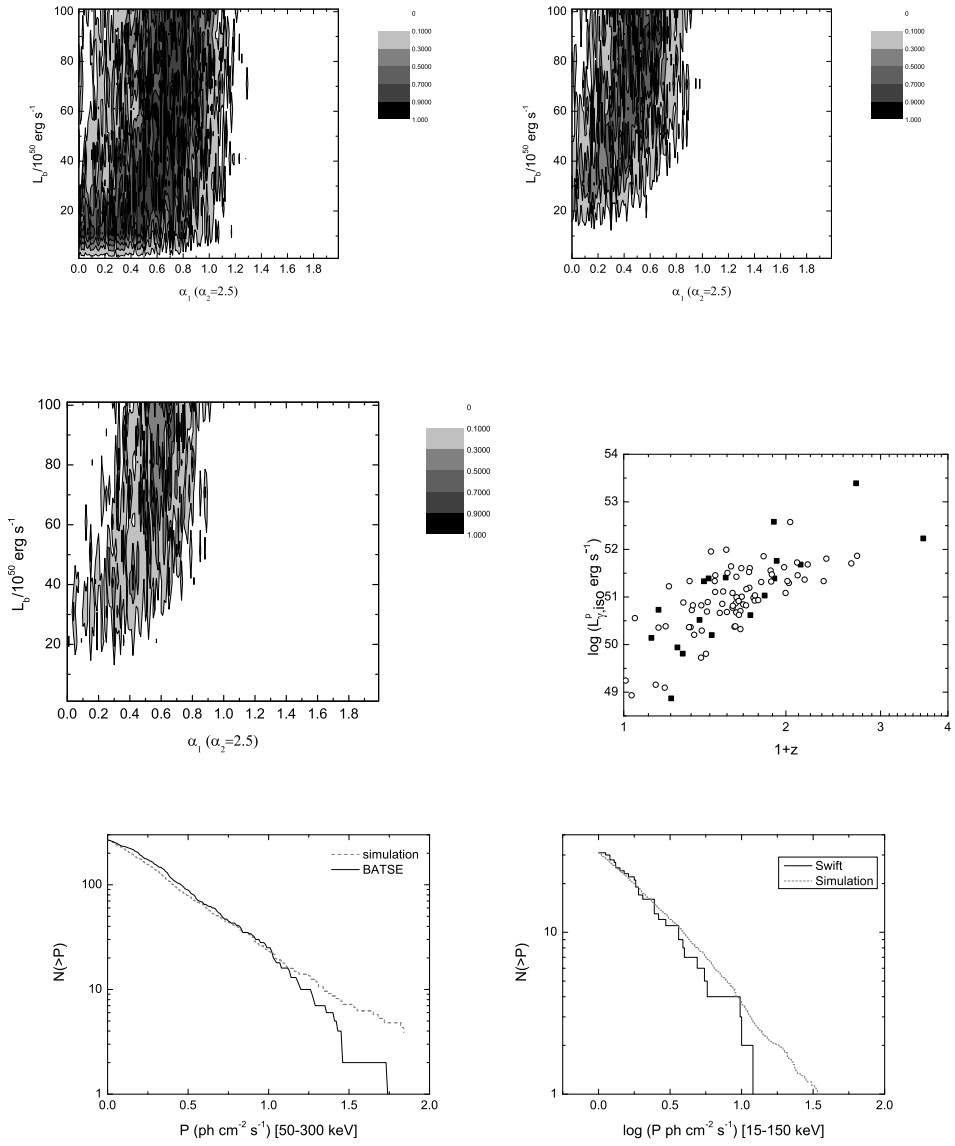

Figure 33 Simulation results showing a distribution of short bursts that has a merger delay timescale of 2 Gyr (σ = 1.0 Gyr), with luminosity function constrained by the $L - z$ data. The first three panels (a-c) are the $P_{KS,z}$, $P_{KS,L}$, $P_{KS,t}$ contours (darker indicates higher KS probability). Panel (d) presents the simulated GRBs (open circles) with the best fit luminosity function as compared with the data (solid dots) in the $L - z$ plane. Panel (e) and (f) show the simulated $\log N - \log P$ (dashed line) as compared with the BATSE (solid line) and *Swift* data, respectively. Darker indicates higher KS probability and consistency with the observed L and z samples.

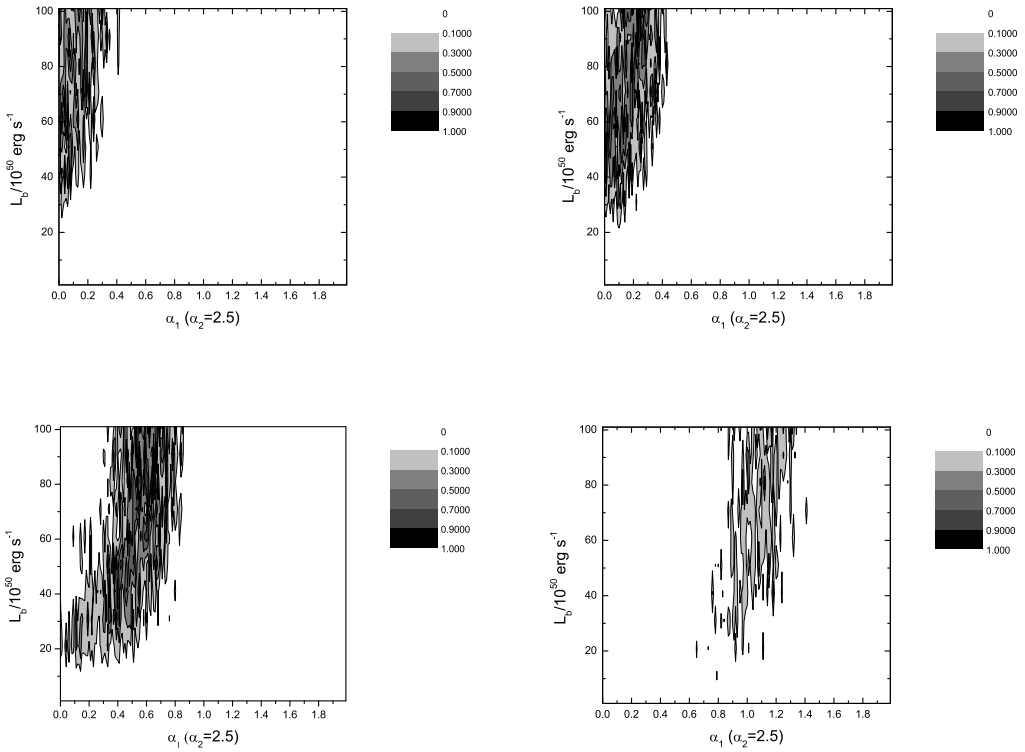

Figure 34 A series of contours displaying the total KS probability, $P_{KS,t}$, of varying luminosity function parameters (break luminosity, L_b and pre-break power-law slope α_1) derived from the $L-z$ constraints for a sample of redshift distribution models. (a) the logarithmic model, (b) the standard population synthesis model, (c) the "twin" population synthesis model, and (d) the no delay model. Darker indicates higher KS probabilities for consistency with the observed $L-z$ distribution.

samples (Figure 31). Second, the burst rate follows the SFH, but the luminosities are sampled from the same LF as 'classical' Type II GRBs (e.g. [185, 178]). In this case, the luminosity function parameters are fixed to those found in Chapter 3 and Virgili *et al.* [178] (excluding LL bursts) and compared to the observations. As expected, this model is securely ruled out by the L and z constraints, while the LNLP shows slopes that are similar with observations. Both of these models imply that at least some short GRBs should originate from a progenitor that has some type of delay from the SFH. These models are also disfavored by host galaxy observations of some short

GRBs [321].

Mixed population model

Since models considering only mergers are not able to account for the available observations of short-hard bursts, the next logical step is to consider models that are a superposition of both events that have a delay from the SFH (Type I) and those that do not (Type II). This possibility is implied by observations of high-redshift bursts and is the basis for the classification analysis of Zhang *et al.* [164]. With this motivation, we test a variety of models, constraining the luminosity function parameters and redshift distribution that has been adjusted to reflect the superposition of burst types. Type I bursts are sampled from a broken power law LF and a redshift distribution that follows the population synthesis studies of Belczynski *et al.* [291, 292]. We do not consider the logarithmic model separately, as the results are similar to those of the standard population synthesis model. Type II bursts are sampled from the luminosity function for 'classical' high-luminosity GRBs [185, 178] and a rate that follows the SFH. We consider various mixing percentages, ranging from 10-95%. The percentage of mixing reported, e.g. '20% mix', indicates a distribution of bursts consisting of 20% Type II bursts and 80% Type I. The most extreme case, where all GRBs are of Type II origin, was discussed in the previous section and shown to be ruled out by the observations.

First, we consider Type I bursts that follow the standard population synthesis model [292]. The L and z constraints peak roughly at 75% mixing and fall off quickly thereafter with only a few patches of consistency around 90% Type II bursts. The corresponding LNLP distributions (Figures 31 and 32) are generally too shallow or have less transparent inconsistencies that are picked up by the AD test to be consistent with the observations. This is expected, as the standard population synthesis model LNLP slopes were also very shallow. The *Swift* constraints also show no consistency

at low mixing, with burgeoning consistency above 75% mixing.

Next, we perform a similar analysis with the 'twin' population synthesis model, which deviates less significantly from the completely Type II model. As expected, the added prompt mergers help to steepen the LNLP and show consistency with the L and z samples. The peak of the consistency is about 20-30% mixing, with mixing greater than 60% securely ruled out by the observations. The BATSE LNLP distribution is too shallow up to about 30% mixing, while the *Swift* sample allows for consistency anywhere from 10-40%. Together, we find consistency with all tests in the range of 30-40% Type II mixing. A breakdown of the various simulated and observed distributions for the 30% mix model is shown in Figure 35.

Discussion

Thanks in part to the rapid localizations of *Swift* and rapid afterglow followup, the sample of short GRBs has increased sufficiently to allow constraints to be placed on their intrinsic distributions. Using Monte Carlo simulations, we have been able to test the underlying assumptions of the compact star merger model for the observed short GRBs and conclude that the hypothesis that "all short GRBs are of merger origin" is disfavored by the data.

In general, population synthesis distributions [273, 291, 292] and empirical relations (i.e. logarithmic model) all demand a very shallow LF in order to satisfy the L and z constraints. This, in turn, has a dramatic effect on the LNLP, causing it also to be very shallow, which is inconsistent with the BATSE LNLP distribution. Many of the constant merger models are also disfavored for the same reasons, the cause of the shallow slopes being the dramatic shifting of the redshift distribution to low redshift caused by very long (> 3 Gyr) delays. The 2 Gyr model, however, is able to satisfy all of the constraints (Figure 33). This model, however, is not realistic, as observations of Galactic NS-NS systems imply a distribution of delays that extends to very long

merger time delays. This result is also fairly consistent with short GRB host galaxy observations [321, 322] and stellar population studies, although these studies are also consistent with the result that implies mixing of Type I and Type II bursts.

A model that invokes a population entirely sampled from Type II bursts, both with an unknown LF and one with values derived from the literature, are also incompatible with the current data. Our simulations imply that some delay from the SFH is needed to explain the observations, as the LNLP distribution is too steep to be consistent.

With these deficiencies as motivation, it is not unreasonable or unrealistic to consider that the observed short GRB sample is actually a superposition of both Type I and Type II bursts. This argument is also consistent with those presented in Zhang *et al.* [164] where it is concluded that the short GRB sample is not a fair representation of the BATSE short/hard GRB sample. Mixing of Type II bursts with the standard population synthesis model does not show significant consistency with the observations, while mixing with the more extreme 'twin' model shows consistency in all tests around a 30-40% Type II-Type I mix (See Figure 35). Analyses of possible 'kicks' given to NS-NS binary systems also give figures in this ballpark [277].

Other analyses also support the claim for some short GRBs being of Type II origin. Numerical hydrodynamical simulations of GRB jets [323] show that observations of short GRBs can be explained by viewing the expanding jet of a GRB near breakout at large viewing angles. Afterglow modeling [324] also shows that a generally accepted short burst, GRB 090510, can be constrained by a burst in a wind medium, which would imply a massive star progenitor, since a wind profile would be absent in a developed compact star binary system.

Detailed models for short GRBs as well as more observations of both bursts and host galaxies would be the greatest asset to further studies in this area, but we show that important and robust conclusions about merger progenitors can be drawn from the available short GRB data.

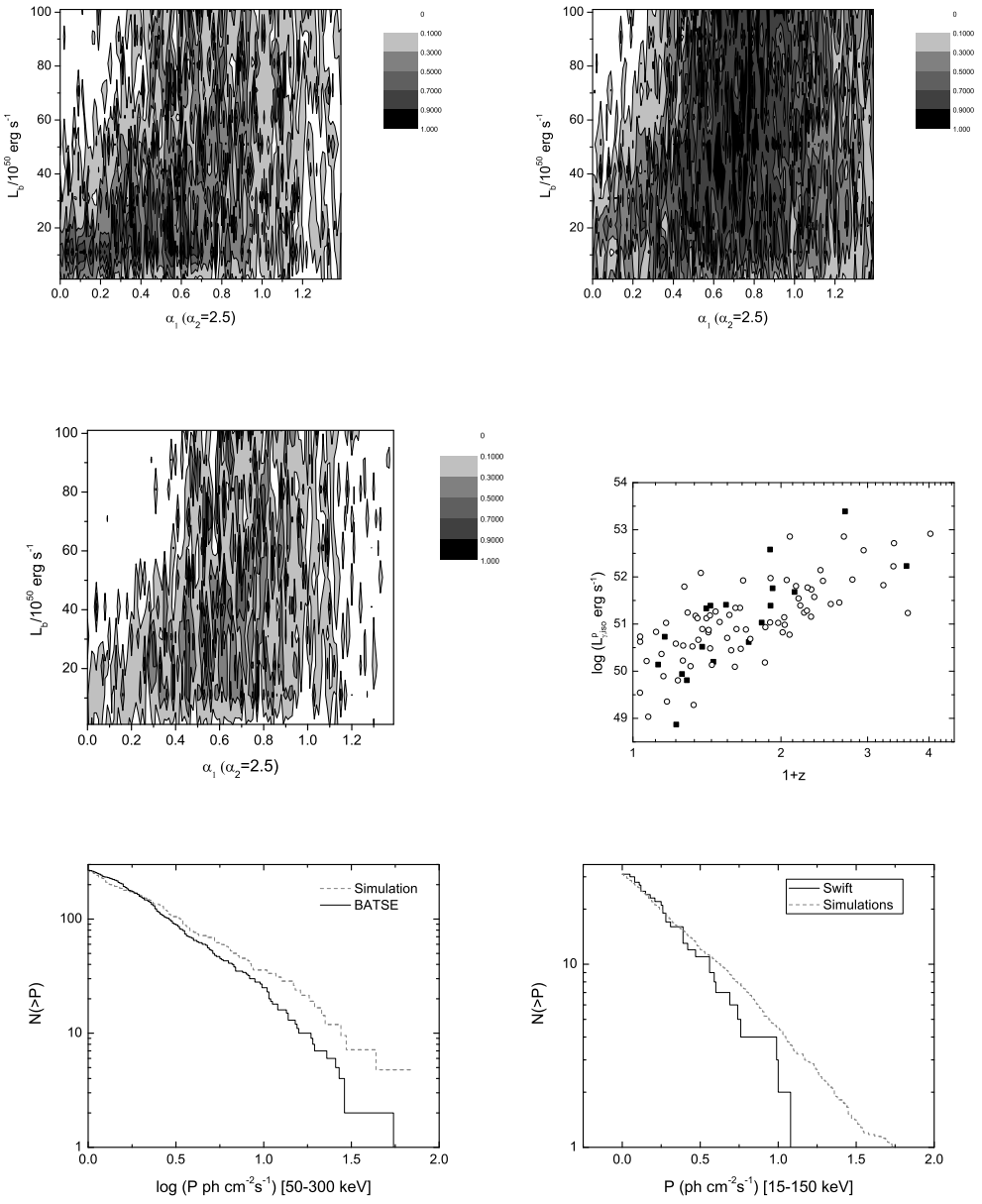

Figure 35 A series of contours displaying the total KS probability, $P_{KS,t}$, for a model with a mix of 30% of bursts following the star formation history and the Type II luminosity function and 70% from the 'twin' population synthesis model. The first three panels (a-c) are the $P_{KS,z}$, $P_{KS,L}$, $P_{KS,t}$ contours (darker indicates higher KS probability). Panel (d) presents the simulated GRBs (open circles) with the best fit luminosity function as compared with the data (solid squares) in the $L - z$ plane. Panel (e) and (f) shows the simulated $\log N - \log P$ (dashed line) as compared with the BATSE (solid line) and *Swift* data, respectively. Darker indicates higher KS probability and consistency with the observed L and z samples.

Model	LF parameters $(\alpha_1, L_B, \alpha_2)$	KS_z D-stat, Prob	KS_L D-stat, Prob	KS_t Prob	BATSE LNLP T stat, P-value	Swift LNLP[a] T stat, P-value
1 Gyr ($\sigma = 1.0$)	(0.7,60,2.5)	0.18, 0.69017	0.14, 0.91849	0.6339	2.12591, 0.04245	-0.50769, 0.47997
2 Gyr ($\sigma = 1.0$)	(0.42,40,2.5)	0.14222, 0.90913	0.18, 0.69017	0.6275	1.57805, 0.07254	-0.55567, 0.49462
3 Gyr ($\sigma = 1.0$)	(0.48,80,2.5)	0.11333, 0.98782	0.12667, 0.96301	0.9513	2.60683, 0.02702	0.41429, 0.22775
4 Gyr ($\sigma = 1.0$)	(0.19,40,2.5)	0.15333, 0.85484	0.15778, 0.8301	0.7096	7.75112, 0.00041	1.25399, 0.10017
5 Gyr ($\sigma = 1.0$)	(0.23,80,2.5)	0.17556, 0.71954	0.18, 0.69017	0.4966	22.48737, 0	6.75693, 0.00090
1 Gyr ($\sigma = 0.3$)	(0.93,80,2.5)	0.19556, 0.58666	0.17778, 0.7049	0.4135	4.70011, 0.00469	-0.36637, 0.4371
2 Gyr ($\sigma = 0.3$)	(0.68,90,2.5)	0.15333, 0.85484	0.16222, 0.80396	0.6873	1.44098 0.08312	-0.69955, 0.53852
3 Gyr ($\sigma = 0.3$)	(0.42,30,2.5)	0.11556, 0.98491	0.15333, 0.85484	0.8419	2.67700, 0.02534	-0.61568, 0.51296
4 Gyr ($\sigma = 0.3$)	(0.35,50,2.5)	0.12889, 0.957	0.14444, 0.89924	0.8606	1.97297, 0.04921	0.25168, 0.26728
5 Gyr ($\sigma = 0.3$)	(0.35,50,2.5)	0.28, 0.17119	0.23333, 0.3608	0.0618	7.91458, 0.00036	5.38114, 0.00272
Population synthesis	(0.19,80,2.5)	0.14, 0.91849	0.12667, 0.96301	0.8845	45.97288, 0	3.72465, 0.01033
Logarithmic	(0.08,80,2.5)	0.15333, 0.85484	0.16444, 0.79044	0.6757	55.10492, 0	6.01050, 0.00164
No delay	(1.15,80,2.5)	0.19556, 0.58666	0.24667, 0.29602	0.17367	19.71989, 0	2.00273, 0.04781
Twin	(0.14,30,2.5)	0.20889 , 0.50096	0.19111, 0.61609	0.30864	2.45747, 0.03102	-0.37388, 0.43936
Mix 20 (PS)[b]	(0.24,80,2.5)	0.16667, 0.77666	0.14, 0.91849	0.71336	32.62143, 0	3.77945, 0.00978
Mix 50 (PS)	(0.2,90,2.5)	0.15556, 0.84266	0.15111 , 0.86662	0.7302	31.48321, 0	4.03421, 0.00798
Mix 75 (PS)	(0.07,30,2.5)	0.14444, 0.89924	0.12444, 0.96845	0.8709	29.94587, 0	3.41307, 0.01332
	(0.62,80,2.5)	0.19333 , 0.60134	0.17556, 0.71954	0.4327	20.85024, 0	1.46488, 0.08117
Mix 85 (PS)	(0.2,30,2.5)	0.19556, 0.58666	0.11333, 0.98782	0.5795	17.84703, 0	1.30219, 0.09546
Mix 90 (PS)	(0.1,30,2.5)	0.273333, 0.192129	0.215556, 0.460233	0.0884	13.68442, 0	1.14002, 0.11223
Mix 10 (Twin)	(0.61,90,2.5)	0.11333, 0.98782	0.14, 0.91849	0.9073	1.70715, 0.06384	3.43719, 0.01305
Mix 20 (Twin)	(0.56,60,2.5)	0.10889, 0.99239	0.10889, 0.99239	0.9848	2.56935, 0.02796	-0.41484, 0.45173
Mix 30 (Twin)	(0.33,20,2.5)	0.16667, 0.77666	0.13556, 0.93559	0.7266	1.85675, 0.05511	-0.32577, 0.42493
Mix 40 (Twin)	(0.5,40,2.5)	0.24667, 0.29602	0.19111, 0.61609	0.1824	1.60761, 0.07044	-0.14547, 0.37216

Table 10 A summary of relevant merger delay models and the associated statistical tests with their test statistics and P-values. Models that have not passed the L and z constraints are not included. Our criteria for passing is at the 95% level. [a]Comparison with the *Swift* short GRB sample with a truncation of 1.5 ph cm^{-2} s^{-1}. [b] Mixing with the population synthesis model (PS).

CHAPTER 6

CONCLUSIONS

Utilizing Monte Carlo simulations and the available observed luminosity, redshift and peak flux data, I have provided robust constraints to three different problems relating to gamma-ray burst populations.

- High-luminosity v. low-luminosity

  Low-luminosity GRBs are likely of a different origin from the population of high-luminosity core-collapse GRBs. A two-component luminosity function model is able to reproduce the observed distributions, including low-luminosity detections, that single-component models fail to do. In addition to rate considerations, this implies that these outlier events are not a simple extrapolation of the HL GRB rate and luminosity function.

- High-z GRBs

  The updated sample of GRBs with known redshift, which includes various events with a $z > 4$, gives interesting constraints to the rate of GRBs at high redshift. This analysis supports the idea of an enhancement of the GRB rate with redshift, although the form still seems unclear. Models with mild luminosity function break evolution are able to accommodate the observations, while models with no enhancement, rate evolution, and simplistic metallicity considerations are not. Metallicity may play a roll, but the underlying assumptions, such as galactic IMF evolution, need to be carefully analyzed before firm conclusions can be drawn.

- Type I v. Type II

  I test the validity of the hypothesis that all observed short-hard GRBs are consistent with a merger model by testing the luminosity function and various

merger time scale distributions. I find that the merger model alone cannot account for all of the observations and that the population of observed GRBs is likely a superposition of Type II (related to massive stars) and Type I (related to compact object merger) bursts. Utilizing models from population synthesis analyses and the luminosity function of HL Type II GRBs, we constrain the mixing to be $\sim 30 - 40\%$ Type II to Type I bursts. Further observations of short-hard bursts are necessary to firmly distinguish these populations, but the current sample supports the idea that determining the intrinsic progenitor of a GRB system relies on much more than just a simplistic analysis of one or two observed quantities.

REFERENCES

[1] Klebesadel, R. W., Strong, I. B., Olson, R. A. *Astrophys. J. Lett.* **182**, 85 (1973).

[2] Halzen, F., Klein, S. *Rev. Scientific Inst.* **81**, 081101 (2010).

[3] LeBohec, S. *et al. J. Phys.: Conf. Ser.* **47**, 232 (2006).

[4] CTA Consortium, arXiv:1008.3703 (2010).

[5] Preece, R. D., Briggs, M. S., Mallozzi, R. S., Pendleton, G. N., Paciesas, W. S., *et al. Astrophys. J. Suppl. Ser.* **126**, 19 (2000).

[6] Ruderman, M. *Ann. N.Y. Acad. Sci.* **262**, 164 (1975).

[7] Cavallo, G., Rees, M. J. *Mon. Not. R. Astron. Soc.* **183**, 359 (1978).

[8] Rybicki, G. B., Lightman, A. P. *Radiative Processes in Astrophysics*. John Wiley & Sons, Inc. (1979). ISBN: 978-0-471-82759-7 (1979) and 0-471-82759-2 (2004).

[9] Blandford, R., McKee, C. *Phys. Fluids* **19**, 1130 (1976).

[10] Paczyński, B. *Astrophys. J.* **308**, L43 (1986).

[11] Goodman, J. *Astrophys. J.* **308**, L47 (1986).

[12] van der Bergh, S. *Ap. Space Sci.* **97**, 385 (1983).

[13] Gehrels, N., *et al. Astrophys. J.* **611**, 1005 (2004).

[14] Atwood, W. B., *et al. Astrophys. J.* **697**, 1071 (2009).

[15] Rees, M. J., Mészáros, P. *Mon. Not. R. Astron. Soc.* **258**, 41P (1992).

[16] Mészáros, P., Rees, M. J. *Astrophys. J.* **405**, 278 (1993).

[17] Shu, F. *The Physics of Astrophysics Volume II: Gas Dynamics*. University of Science Books (1992). ISBN 0-935702-65-2.

[18] Achterberg, A., Gallant, Y. A., Kirk, J. G. *Mon. Not. R. Astron. Soc.* **328**, 393 (2001).

[19] Blandford, R., Eichler, D. *Phys. Rep.* **154**, 1 (1987).

[20] Zhang, B., Yan, H. *Astrophys. J.* **727**, 109 (2011).

[21] Liang, E.-W., Noguchi, K. *Astrophys. J.* **705**, 1473 (2009).

[22] Meegan, C., Fishman, G., Wilson, R., Paciesas, W., Pendleton, G., *et al. Nature.* **355**, 143 (1992).

[23] Boella, G., Butler, R. C., Perola, G. C., Piro, L., Scarsi, L., Bleeker, J. A. M. *Astron. Astrophys. Suppl.* **122**, 299 (1997).

[24] Costa, E., Frontera, F., Heise, J., Feroci, M., in't Zand, J., *et al. Nature.* **387**, 783 (1997).

[25] van Paradijs, J., Groot, P., Kouveliotou, C., Strom, R., *et al. Nature.* **386**, 686 (1997).

[26] Frail, D., Kulkarni, S. R., Nicastro, L., Feroci, M., Taylor, G. B. *Nature.* **389**, 261 (1997).

[27] Metzger, M., Djorgovski, S. G., Kulkarni, S., Steidel, C., Adelberger, K., *et al. Nature.* **387**, 878 (1997).

[28] Kulkarni, S., Berger, E., Bloom, J., Chaffee, F., Diercks, A., *et al.* In *Gamma-ray Bursts. AIP Conf. Proc.*, **526**, ed M. Kippen, R. Mallozzi, G. Fishman, p. 277. New York: AIP.

[29] Lamb, D. Q. *Publ. Astron. Soc. Pac.* **107**, 1152 (1995).

[30] Paczyński, B. *Publ. Astron. Soc. Pac.* **107**, 1167 (1995).

[31] BATSE position map. URL http://f64.nsstc.nasa.gov/batse/grb/skymap/

[32] Eichler, D., Livio, M., Piran, T., Schramm, D. *Nature.* **340**, 126 (1989).

[33] Narayan, T., Paczyński, B., Piran, T. *Astrophys. J.* **395**, L8 (1992).

[34] Clark, J. P. A., Eardley, D. M. *Astrophys. J.* **215**, 311 (1977).

[35] Usov, V. V. *Nature.* **357**, 472 (1992).

[36] Duncan, R. C., Thompson, C. *Astrophys. J.* **392**, L9 (1992).

[37] Woosley, S. E. *Astrophys. J.* **405**, 273 (1993).

[38] Rees, M. J., Mészáros, P. *Astrophys. J. Lett.* **430**, L93 (1994).

[39] Paczyński, B., Xu, G. *Astrophys. J.* **427**, 708 (1994).

[40] Thompson, C., *Mon. Not. R. Astron. Soc.* **270**, 480 (1994).

[41] Mészáros, P., Rees, M. J. *Mon. Not. R. Astron. Soc.* **269**, L41 (1994).

[42] Mészáros, P., Rees, M. J. *Astrophys. J.* **476**, 232 (1997).

[43] Sari, R., Piran, T., Narayan, R. *Astrophys. J.* **497**, L17 (1998).

[44] Mészáros, P. *Annu. Rev. Astron. Astrophys.* **40**, 137 (2002).

[45] Mészáros, P., Laguna, P., Rees, M. J. *Astrophys. J.* **415**, 181 (1993).

[46] Piran, T., Shemi, A., Narayan, R. *Mon. Not. R. Astron. Soc.* **263**, 861 (1993).

[47] Kobayashi, S., Piran, T., Sari, R. *Astrophys. J.* **513**, 669 (1999).

[48] Mészáros, P., Rees, M. J. *Astrophys. J.* **530**, 292 (2000).

[49] Rees, M. J., Mészáros, P. *Astrophys. J.* **628**, 847 (2005).

[50] Pe'er, A., Ryde, F. arXiv:1008.4590 (2010).

[51] Ryde, F., *et al. Astrophys. J.* **709**, L172 (2010).

[52] Pe'er, A., Mészáros, P., Rees, M. J., *Astrophys. J.* **635**, 476 (2005).

[53] Pe'er, A., Mészáros, P., Rees, M. J. *Astrophys. J.* **642**, 995 (2006).

[54] Lazzati, D., Begelman, M. C. *Astrophys. J.* **725**, 1137 (2010).

[55] Beloborodov, A M. *Mon. Not. R. Astron. Soc.* **407**, 1033 (2010).

[56] Abdo, A. A., *et al. Science.* **323**, 1688 (2009).

[57] Fishman, G. J., Meegan, C. A. *Annu. Rev. Astron. Astrophys.* **33**, 415 (1995).

[58] Kumar, P. *Astrophys. J.* **523**, L113 (1999).

[59] Panaitescu, A., Spada, M., Mészáros, P. *Astrophys. J.* **522**, L105 (1999).

[60] Piran, T., Sari, R. In *Gamma-Ray Bursts. AIP Conf. Proc. 428*, ed. C. Meegan, R. Preece, T. Koshut, p. 662. New York: AIP (1998).

[61] Paczyński, B., Rhoads, J. E. *Astrophys. J.* **418**, L5 (1993).

[62] Katz, J. *Astrophys. J.* **432**, L107 (1994).

[63] Akerlof, C., *et al. Nature.* **398**, 400 (1999).

[64] Mészáros, P., Rees, M. J., Papathanassiou, H. *Astrophys. J.* **432**, 181 (1994).

[65] Tavani, M. *Astrophys. J.* **466**, 768 (1996).

[66] Chevalier, R. A., Li, Z.-Y. *Astrophys. J.* **536**, 195 (2000).

[67] Li, Z.-Y., Chevalier, R. A. arXiv:astro-ph/0110002 (2001).

[68] Li, Z.-Y., Chevalier, R. A. *Astrophys. J.* **589**, L69 (2003).

[69] Kumar, R., Panaitescu, A. *Astrophys. J.* **541**, L9 (2000).

[70] Gou, L. J., Dai, Z. G., Huang, Y. F., Lu, T. *Astron. Astrophys.* **368**, 464 (2001).

[71] Zhang, B., Mészáros, P. *Internat. J. Modern Phys. A.* **19**, No. 15, 2385 (2004).

[72] Ghisellini, A., Celotti, A., Lazzati, D. *Mon. Not. R. Astron. Soc.* **313**, L1 (2000).

[73] Preece, R. D., *et al. Astrophys. J.* **506**, L23 (1998).

[74] Mevedev, M. V. *Astrophys. J.* **540**, 704 (2000).

[75] Bykov, A. M., Mészáros, P. *Astrophys. J.* **461**, L37 (1996).

[76] Daigne, F., Mochkovitch, R. *Mon. Not. R. Astron. Soc.* **296**, 275 (1998).

[77] Panaitescu, A., Mészáros, P. *Astrophys. J.* **554**, L17 (2000).

[78] Racusin, J. L., *et al. Nature.* **455**, 183, (2008).

[79] Resmi, L., Zhang, B. *Mon. Not. R. Astron. Soc.* Submitted (2010).

[80] Derishev, E. V., Kocharovsky, V. V., Kocharovsky, Vl. V. *Astron. Astrophys.* **372**, 1071 (2001).

[81] Zou, Y.-C., Piran, T., Sari, R. *Astrophys. J.* **692**, L92 (2009).

[82] Piran, T., Sari, R., Zou, Y.-C. *Mon. Not. R. Astron. Soc.* **393**, 1107 (2009).

[83] Nousek, J. A., *et al. Astrophys. J.* **642**, 389 (2006).

[84] O'Brien, P. T. *et al. Astrophys. J.* **647**, 1213 (2006).

[85] Chincarini, G. *et al.* arXiv:astro-ph/0506453 (2005).

[86] Rhoads, J. E., *Astrophys. J.* **487**, L1 (1997).

[87] Rhoads, J. E., *Astrophys. J.* **525**, 737 (1999).

[88] Sari, R., Piran, T., Halpern, J. P. *Astrophys. J.* **591**, L17 (1999).

[89] Frail, D. A., Kulkarni, S. R., Sari, R. *et al. Astrophys. J. Lett.* **562**, 55 (2001).

[90] Panaitescu, A., *et al. Mon. Not. R. Astron. Soc.* **369**, 2059 (2006).

[91] Liang, E.-W., *et al. Astrophys. J.* **653**, L81 (2006).

[92] Burrows, D. N., Racusin, J. *Il Nuovo Cimento B* **121**, 1273 (2007).

[93] Liang, E.-W., Racusin, J. L., Zhang, B., Zhang, B.-B., Burrows, D. N. *Astrophys. J.* **675**, 528 (2008).

[94] Willingale, R., *et al. Astrophys. J.* **662**, 1093 (2007).

[95] Kocevski, D., Butler, N. *Astrophys. J.* **680**, 531 (2008).

[96] Evans, P. A., *et al. Mon. Not. R. Astron. Soc.* **397**, 1177 (2009).

[97] Zhang, B., Mészáros, P. *Astrophys. J.* **571**, 876 (2002).

[98] Rossi, E., Lazzati, D., Rees, M. J., *Mon. Not. R. Astron. Soc.* **332**, 945 (2002).

[99] Tagliaferri, G., *et al. Nature.* **436**, 985 (2005).

[100] Zhang, B., *et al.* **642**, 354 (2006).

[101] Barthelmy, S., *et al. Nature.* **438**, 994 (2005).

[102] Liang, E.-W., *et al. Astrophys. J.* **646**, 351 (2006).

[103] Liang, E.-W., Zhang, B.-B., Zhang, B. *Astrophys. J.* **670**, 565 (2007).

[104] Zhang, B.-B., Liang, E.-W., Zhang, B. *Astrophys. J.* **666**, 1002 (2007).

[105] Butler, N. R., Kocevski, D. *Astrophys. J.* **668**, 400 (2007).

[106] Starling, R. L. C., *et al. Mon. Not. R. Astron. Soc.* **384**, 504 (2008).

[107] Zhang, B.-B., Zhang, B., Liang, E.-W., Wang, X.-Y., *Astrophys. J.* **690**, L10 (2009).

[108] Fenimore, E. E., Madras, C. D., Nayakshin, S. *Astrophys. J.* **473**, 998 (1996).

[109] Kumar, P., Panaitescu, A. *Astrophys. J.* **541**, L51 (2000).

[110] Dermer, C. D. *Astrophys. J.* **614**, 284 (2004).

[111] Dyks, J., Zhang, B., Fan, Y. Z. arXiv:astro-ph/0511699 (2005).

[112] Qin, Y.-P. *Astrophys. J.* **683**, 900 (2008).

[113] Wu, Z. F. *et al. 36th COSPAR Sci. Ass. #731*, arXiv:astro-ph/0512555 (2006).

[114] Yamazaki, R., Toma, K., Ioka, K., Nakamura, T. *Mon. Not. R. Astron. Soc.* **369**, 311 (2006).

[115] Ghisellini, G., *et al. Astrophys. J.* **658**, L75 (2007).

[116] Kumar, P., Narayan, R., Johnson, J. L. *Mon. Not. R. Astron. Soc.* **388**, 1729 (2008).

[117] Cannizzo, J. K., Gehrels, N. *Astrophys. J.* **700**, 1047 (2009).

[118] Lindner, C. C., *et al. Astrophys. J.* **713**, 800 (2010).

[119] Burrows, D. N., *et al. Science.* **309**, 1833 (2005).

[120] Fan, Y.-Z., Wei, D. M. *Mon. Not. R. Astron. Soc.* **364**, L42 (2005).

[121] Lazzati, D., Perna, R. *Mon. Not. R. Astron. Soc.* **375**, L46 (2007).

[122] Maxham, A., Zhang, B. *Astrophys. J.* **707**, 1623 (2009).

[123] Chincarini, G., *et al. Astrophys. J.* **671**, 1903 (2007).

[124] Falcone, A. D., *et al. Astrophys. J.* **671**, 1921 (2007).

[125] Ioka, K., Kobayashi, S., Zhang, B. *Astrophys. J.* **631**, 429 (2005).

[126] Jakobsson, P., *et al. Astrophys. J.* **617**, L21 (2004).

[127] Rol, E. *et al. Astrophys. J.* **624**, 868 (2005).

[128] Zhang, B., Kobayashi, S., Mészáros, P. *Astrophys. J.* **595**, 950 (2003).

[129] Bloom, J. S., *et al. Nature.* **401**, 453 (1999).

[130] Waxman, E. *Nature.* **423**, 388 (2003).

[131] Lyutikov, M., Pariev, R. D., Blandford, R. D. *Astrophys. J.* **597**, 998 (2003).

[132] Granot, J. *Astrophys. J.* **596**, L17 (2003).

[133] Toma, K., *et al. Astrophys. J.* **698**, 1042 (2009).

[134] Coburn, W., Boggs, S. E. *Nature.* **423**, 415 (2003).

[135] Willis, D. R. *et al. Astron. Astrophys.* **439**, 245 (2005).

[136] Rutledge, R. E., Fox, D. B. *Mon. Not. R. Astron. Soc.* **350**, 1288 (2004).

[137] Zhang, B., Pe'er, A. *Astrophys. J.* **700**, L65 (2009).

[138] Fan, Y.-Z. *Mon. Not. R. Astron. Soc.* **403**, 483 (2010).

[139] Galama, T. J., *et al. Nature.* **395**, 670 (1998).

[140] Kulkarni, S. R. *et al. Nature.* **395**, 663 (1998).

[141] Pian, E., *et al. Astrophys. J.* **536**, 778 (2000).

[142] Soderberg, A. M., *et al. Astrophys. J.* **627**, 877 (2005).

[143] Groot, P. J., *et al. IAU Circ. 6584* (1997).

[144] Chandra, P., Cenko, S. B., Frail, D. A., Chevalier, R. A., Macquart, J.-P., *et al. Astrophys. J.* **683**, 924 (2008).

[145] Taylor, G. B., Momjian, E., Pihlström, Y., Ghosh, T., Salter, C. *Astrophys. J.* **622**, 986 (2005).

[146] Oren, Y., Nakar, E., Piran, T. *Mon. Not. R. Astron. Soc.* **353**, L35 (2004).

[147] Granot, J., Ramirez-Ruiz, E., Loeb, A. *Astrophys. J.* **618**, 413 (2005).

[148] Kaneko, Y., Ramirez-Ruiz, E., Granot, J., Kouveliotou, C., Woosley, S. E., *et al. Astrophys. J.* **654**, 385 (2007).

[149] Frail, D. A., *et al. Astrophys. J.* **646**, L99 (2006).

[150] Guo, J.-J., Fox, D. B., Mészáros, P. *Astrophys. J.* **668**, 1083 (2007).

[151] Soderberg, A. M., *et al. Nature.* **442**, 1014 (2006).

[152] Cenko, S. B., Kasliwal, M., Harrison, F. A., Pal'shin V., Frail, D. A., *et al. Astrophys. J.* **652**, 490 (2006).

[153] Soderberg, A. M., *et al. Nature.* **463**, 513 (2010).

[154] Cusumano, G., *et al. Nature.* **440**, 164 (2006).

[155] Haislip, J. B., *et al. Nature.* **440**, 181 (2006).

[156] Kawai, N. *et al. Nature.* **440**, 183 (2006).

[157] Greiner, J. *et al. Astrophys. J.* **693**, 1610 (2009).

[158] Salvaterra, R. *et al. Nature.* **461**, 1258 (2009).

[159] Tanvir, N., *et al. Nature.* **461**, 1254 (2009).

[160] Kouveliotou, C. *et al. Astrophys. J.* **558**, L47 (1993).

[161] Nakar, E. *Phys. Rep. 442*, 166 (2007).

[162] Zhang, B. *Chin. J. Astron. Astrophys.* **7**, 1 (2007).

[163] Zhang, B., Zhang, B.-B., Liang, E.-W., Gehrels, N., Burrows, D., Mészáros, P. *Astrophys. J.* **655**, L25 (2007).

[164] Zhang, B. *et al. Astrophys. J.* **703**, 1696 (2009).

[165] Bloom, J. S., Frail, D. A., Sari, R. *Astron. J.* **121**, 2879 (2001).

[166] Band, D., *et al. Astrophys. J.* **413**, 281 (2001).

[167] Sakamoto, T., *et al. Astrophys. J. Suppl. Ser.* **175**, 179 (2008).

[168] Briggs, M. S., *et al. Astrophys. J.* **524**, 82 (1999).

[169] Sakamoto, T., *et al. Astrophys. J.* **693**, 922 (2009).

[170] Liang, E.-W., Dai, Z. G., Wu, X. F. *Astrophys. J.* **606**, L29 (2004).

[171] Colgate, S. A. *Astrophys. J.* **187**, 333 (1974).

[172] Hjorth, J., *et al. Nature.* **423**, 847 (2003).

[173] Stanek, K. Z., *et al. Astrophys. J.* **591**, L17 (2003).

[174] Campana, S., *et al. Nature.* **442**, 1008 (2006).

[175] Tinney C., *International Astronomical Union Circulars.* **6896**, 1 (1998).

[176] Mazzali, P. A., *et al. Nature.* **442**, 1018 (2006).

[177] Toma, K., Ioka, K., Sakamoto, T., Nakamura, T., *Astrophys. J.* **659**, 1420 (2007).

[178] Virgili, F. J., Liang, E.-W., Zhang, B. *Mon. Not. R. Astron. Soc.* **392**, 91 (2009).

[179] Schmidt, M., *Astrophys. J.* **552**, 36 (2001).

[180] Guetta, D., Perna, R., Stella, L., Vietri, M. *Astrophys. J.* **615**, L73 (2004).

[181] Guetta, D., Piran, T., Waxman, E. *Astrophys. J.* **619**, 412 (2005).

[182] Guetta, D., Della Valle, M. *Astrophys. J.* **657**, L76 (2007).

[183] Coward, D. M. *Mon. Not. R. Astron. Soc.* **360**, 77 (2005).

[184] Le, T., Dermer, C. D. *Astrophys. J.* **661**, 394 (2007).

[185] Liang, E.-W., Zhang, B., Virgili, F. J., Dai, Z. G. *Astrophys. J.* **662**, 1111 (2007).

[186] Rowan-Robinson, M. *Astrophys. Space Sci.* **266**, 291 (1999).

[187] Porciani, C., Madau, P. *Astrophys. J.* **548**, 522 (2001).

[188] Sakamoto T., *et al. Astrophys. J.* **669**, 1115 (2007).

[189] Sakamoto, T. Private communication.

[190] Norris, J. P., *et al. Astrophys. J.* **627**, 324 (2005).

[191] Bloom, J. S., *et al. Astron. J.* **121**, 2879 (2001).

[192] Butler, N., Kocevski, D., Bloom, J. S., Curtis, J. L. *Astrophys. J.* **671**, 656 (2007).

[193] Stern, B. E. *et al. Astrophys. J.* **563**, 80 (2001).

[194] Paciesas, W. S., *et al. Astrophys. J. Suppl. Ser.* **122**, 465 (1999).

[195] Schmidt, M., *Astrophys. J.* **616**, 1072 (2004).

[196] Press, W. H., *et al. Numerical Recipes in Fortran.* Cambridge Univ. Press, Cambridge (1999).

[197] Cobb, B. E., *et al. Astrophys. J.* **645**, L113 (2006).

[198] Pian, E., *et al. Nature.* **442**, 1011 (2006).

[199] Chapman, R., *et al. Mon. Not. R. Astron. Soc.* **382**, 21 (2007).

[200] Daigne, F., Rossi, E., Mochkowitch, R. *Mon. Not. R. Astron. Soc.* **372**, 1034 (2006).

[201] Cen, R., Fang, T. arXiv:0710.4370 (2007).

[202] Kistler M. D., Yüksel H., Beacom J. F., Stanek K. Z. *Astrophys. J.* **673**, 119 (2008).

[203] Kistler M. D., Yüksel H., Beacom J. F., Hopkins, A. M., Wyithe, J., Stuart B. *Astrophys. J.* **705**, 104 (2009).

[204] Li, L.-X., *Mon. Not. R. Astron. Soc.* **388**, 1487 (2008).

[205] Qin, S. F., Liang, E.-W., Lu, R. J., Wei, J. Y., Zhang, S. N. *Mon. Not. R. Astron. Soc.* **406**, 558 (2010).

[206] Wanderman, D., Piran, T. *Mon. Not. R. Astron. Soc.* **406**, 1944 (2010).

[207] Dai, X., Zhang, B. *Astrophys. J.* **621**, 875 (2005).

[208] Soderberg, A. M., *et al. Nature.* **453**, 469 (2008).

[209] Li, L.-X., *Mon. Not. R. Astron. Soc.* **388**, 603 (2008).

[210] Xu, D., Watson, D., Fynbo, J., Fan, Y.-Z., Zou, Y.-C., Hjorth, J. *37th COSPAR Scientific Assembly.* **37**, 3512 (2008).

[211] Amati, L. *Mon. Not. R. Astron. Soc.* **372**, 233 (2006).

[212] Abel, T., Bryan, G. L., Norman, M. L. *Science.* **295**, 92 (2002).

[213] Bromm, V., Loeb, A. *Astrophys. J.* **575**, 111 (2002).

[214] Wijers, R. A. M., *et al. Mon. Not. R. Astron. Soc.* **294**, L13 (1998).

[215] Totani, T. *Astrophys. J.* **511**, 41 (1999).

[216] Lamb, D. Q., Reichart, D. E. *Astrophys. J.* **536**, 1 (2000).

[217] Blain, A. W., Natarayan, P. *Mon. Not. R. Astron. Soc.* **312**, L35 (2000).

[218] Guetta, D., Piran, T. *J. Cosmol. Astropart. Phys.* **7**, 3 (2007).

[219] Langer, N., Norman, C. A. *Astrophys. J.* **638**, L66 (2006).

[220] Choi, J. H., Nagamine, K. *Mon. Not. R. Astron. Soc.* **407**, 1464 (2010).

[221] Galassi, M. *et al. GNU Scientific Library Reference Manual (3rd Ed.)*, ISBN 0954612078.

[222] Saito, M., Matsumoto, M. *SIMD-oriented Fast Mersenne Twister: a 128-bit Pseudorandom Number Generator, Monte Carlo and Quasi-Monte Carlo Methods 2006* (Berlin: Springer), 607 (2008).

[223] Butler, N., *et al. Astrophys. J.* **711**, 495 (2010).

[224] Scholz, F. W., Stephens, M. A. *J. Am. Stat. Assoc.* **82**, 918 (1987).

[225] Loredo, T. J., Wasserman, I. M. *Astrophys. J.* **502**, 75 (1998).

[226] Band, D. *Astrophys. J.* **644**, 378 (2006).

[227] Hopkins, A. M., Beacom, J. F. *Astrophys. J.* **651**, 142 (2006).

[228] Bromm, V., Loeb, A. *Astrophys. J.* **642**, 382 (2006).

[229] Springel, V. *Mon. Not. R. Astron. Soc.* **364**, 1105 (2005).

[230] Choi, J., Nagamine, K. *Mon. Not. R. Astron. Soc.* **393**, 1595 (2009).

[231] Haardt, F., Madau, P. *Astrophys. J.* **461**, 20 (1996).

[232] Katz, N., Weinberg, D. H., Hernquist, L. *Astrophys. J. Suppl. Ser.* **105**, 19 (1996).

[233] Davé, R., Hernquist, L., Katz, N., Weinberg, D. H. *Astrophys. J.* **511**, 521 (1999).

[234] Springel, V., Hernquist, L. *Mon. Not. R. Astron. Soc.* **339**, 289 (2003).

[235] Schaye, J., *et al. Mon. Not. R. Astron. Soc.* **402**, 1536 (2010).

[236] Choi, J., Nagamine K. *Mon. Not. R. Astron. Soc.* **410**, 2579 (2011).

[237] Komatsu, E., *et al. Astrophys. J. Suppl. Ser.* **192**, 18 (2011).

[238] Tremonti, C. A., *et al. Astrophys. J.* **613**, 898 (2004).

[239] Savaglio, S., *et al. Astrophys. J.* **635**, 260 (2005).

[240] Kewley, L., Kobulnicky, H. A. In *Starbursts: From 30 Doradus to Lyman Break Galaxies*, ed. R. de Grijs & R. M. González Delgado (Dordrecht: Springer), 307 (2005).

[241] Kennicutt, R. C. *Annu. Rev. Astron. Astrophys.* **36**, 189 (1998).

[242] Niino Y., Choi J. H., Masakazu A. R., Nagamine K., Totani T., Zhang B. *Astrophys. J.* **726**, 88 (2011).

[243] Bouwens, R. J., *et al.* arXiv:1006.4360 (2010).

[244] Laskar, T., Berger, E., Chary, R.-R. arXiv:1102.1019 (2011).

[245] Mazets, E. P., *et al.* P.S. 2004 In *Astronomical Society of the Pacific Conference Series*, ed. M. Feroci, F. Frontera, N. Masett, and L. Piro, 102 (1981).

[246] Norris, J. P., Cline., T. L., Desai, U. D., Teegarden, B. J. *Nature.* **308**, 434 (1984).

[247] Virgili, F. J., Zhang, B., O'Brien, P. T., Troja, E. *Astrophys. J.* **727**, 109 (2011).

[248] Mukherjee, S. *et al. Astrophys. J.* **508**, 314 (1998).

[249] Horváth, I. *Astrophys. J.* **508**, 757 (1998).

[250] Hakkila, J., *et al. Astrophys. J.* **538**, 165 (2000).

[251] Gehrels, N., *et al. Nature.* **437**, 851 (2005).

[252] Fox, D. B., *et al. Nature.* **437**, 845 (2006).

[253] Villasenor, J. S., *et al. Nature.* **437**, 855 (2005).

[254] Hjorth, J. *et al. Nature.* **437**, 859 (2005).

[255] Berger, E., *et al. Astrophys. J.* **634**, 501 (2005).

[256] Bloom, J. S., *et al. Astrophys. J.* **638**, 354 (2006).

[257] Berger, E., *et al. Astrophys. J.* **664**, 1000 (2007).

[258] Berger, E., *et al. Astrophys. J.* **690**, 231 (2009).

[259] Norris, J. P., Bonnell, J. T. *Astrophys. J.* **643**, 266 (2006).

[260] Troja, E., *et al. Mon. Not. R. Astron. Soc.* **385**, L10 (2008).

[261] Gehrels, N., *et al. Nature.* **444**, 1044 (2006).

[262] Mangano, V., *et al. Astron. Astrophys.* **470**, 105 (2007).

[263] Bloom, J. S., Butler, N. R., Perley, D. A. **AIP Conference Series, Vol. 1000**, (eds. M. Galassi, D. Palmer, E. Fenimore), 11-15 (2008).

[264] MacFayden, A. I., Woosley, S. E. *Astrophys. J.* **524**, 262 (1999).

[265] Bloom, J. S., Sigurdsson, S., Pols, O. R. *Mon. Not. R. Astron. Soc.* **305**, 763 (1999).

[266] Rosswog, S., Ramirez-Ruiz, E., Davies, M. B. *Mon. Not. R. Astron. Soc.* **345**, 1077 (2003).

[267] Zhang, B., Mészáros, P. *Astrophys. J.* **581**, 1236 (2002).

[268] Heger, A. *et al. Astrophys. J.* **591**, 288 (2003).

[269] Nagataki, S., *et al. Astrophys. J.* **596**, 401 (2003)

[270] Tominaga, N., *et al. Astrophys. J.* **657**, L77 (2007).

[271] Kann, D. A., *et al.* arXiv:0804.1959.

[272] Barthelmy, S. D., *et al. Spa. Sci. Rev.* **120**, 143 (2005).

[273] Belczynski, K., Perna, R., Bulik, T., Kalogera, V., Ivanova, N., Lamb, D. *Astrophys. J.* **648**, 1110 (2006).

[274] Zheng, Z., Ramirez-Ruiz, E. *Astrophys. J.* **665**, 1220 (2007).

[275] O'Shaughnessy, R., Belczynski, K., Kalogera, V. *Astrophys. J.* **675**, 566 (2008).

[276] Fong, W., Berger, E., Fox, D. B. *Astrophys. J.* **708**, 9 (2010).

[277] Cui, X.-H., Aoi, J., Nagataki, S., Xu, R.-X. in *AIP Conf. Proc. 1279, Deciphering the Ancient Universe with Gamma-ray Bursts*, ed. Nobuyuki Kawai, Shigehiro Nagataki (Melville, NY: AIP), 136 (2010).

[278] Norris, J. P., Marani, G. F., Bonnell, J. T. *Astrophys. J.* **534**, 248 (2000).

[279] Yi, T., Liang, E.-W., Qin, Y., Lu, R. *Mon. Not. R. Astron. Soc.* **367**, 1751 (2006).

[280] Salmonson, J. D., *Astrophys. J.* **544**, L115 (2000).

[281] Ioka, K., Nakamura, T. *Astrophys. J.* **554**, L163 (2001).

[282] Shen, R.-F., Song, L.-M., Li, Z. *Mon. Not. R. Astron. Soc.* **362**, 59 (2005).

[283] Lu, R.-J., Qin, Y.-P., Zhang, Z.-B., Yi, T.-F. *Mon. Not. R. Astron. Soc.* **367**, 275 (2006).

[284] Ando, S. *J. Cosmol. Astropart. Phys.* JCAP06(2004)007 (2004).

[285] Guetta, D., Piran, T. *Astron. Astrophys.* **435**, 421 (2005).

[286] Nakar, E., Gal-Yam, A., Fox, D. B. *Astrophys. J.* **650**, 281 (2006).

[287] Guetta, D., Piran, T. *Astron. Astrophys.* **453**, 823 (2006).

[288] Graham, J. F., *et al. Astrophys. J.* **698**, 1620 (2009).

[289] Belczynski, K., Kalogera, V. *Astrophys. J.* **571**, 394 (2001).

[290] Belczynski, K., Bulik, T., Kalogera, V. *Astrophys. J.* **571**, 147 (2002).

[291] Belczynski, K., Stanek, K. Z., Fryer, C. L. arXiv:0712.3309 (2007).

[292] Belczynski, K., Hartmann, D. H., Fryer, C. L., Holz, D. E., O'Shea, B. *Astrophys. J.* **708**, 117 (2010).

[293] Ivanova, N., Belczynski, K., Kalogera, V., Rasio, F., Taam, R. E. *Astrophys. J.* **592**, 475 (2003).

[294] Dewi, J., Pols, O. *Mon. Not. R. Astron. Soc.* **344**, 629 (2003).

[295] Bhattacharya, D., van den Heuvel, E. P. J. *Phys. Rep.* **203**, 1 (1991).

[296] Grindlay, J., Portegies, Zwart, S., McMillan, S. *Nature Phys.* **2**, 116 (2006).

[297] Tanvir, N. R., Chapman, R., Leva, A. J., Priddey, R. S. *Nature.* **438**, 991 (2005).

[298] Chapman, R., Priddey, R. S., Tanvir, N. R. *Mon. Not. R. Astron. Soc.* **395**, 1515 (2009).

[299] Salvaterra, R., Cerutti, A., Chincarini, G., Colpi, M., Guidorzi, C., Romano, P. *Mon. Not. R. Astron. Soc.* **388**, L6 (2008).

[300] Nakar, E., Gal-Yam, A., Piran, T., Fox, D. B. *Astrophys. J.* **640**, 849 (2006).

[301] Cobb, B. E., Bailyn, C. D. *Astrophys. J.* **677**, 1157 (2008).

[302] Castro-Tirado, A. J., *et al. Astron. Astrophys.* **439**, L15 (2005).

[303] Covino, S., *et al. Astron. Astrophys.* **447**, 5 (2006).

[304] Prochaska, J. X., *et al. Astrophys. J.* **642**, 989 (2006).

[305] Berger, E., *et al. Nature.* **438**, 988 (2005).

[306] Della Valle, M., *et al. Nature.* **444**, 1050 (2006).

[307] Soderberg, A. M., *et al. Astrophys. J.* **650**, 261 (2006).

[308] Levan, A. J. *et al. Astrophys. J.* **648**, L9 (2006).

[309] de Ugarte Postigo, A., *et al. Astrophys. J.* **648**, L83 (2006).

[310] Bloom, J. S., *et al. Astrophys. J.* **654**, 878 (2007).

[311] Cucchiara, A., Fox, D. B., Berger, E., Price, P. A. *GCN Circ.*, **5470**, 1 (2006).

[312] Cenko, S. B., *et al.* arXiv:0802.0874 (2008).

[313] Cucchiara, A., Fox, D. B., Cenko, S. B., Berger, E., Price, P. A., Radomski, J. *GCN Circ.*, **6665**, 1 (2007).

[314] Kocevski, D., *et al. Mon. Not. R. Astron. Soc.* **404**, 963 (2010).

[315] D'Avanzo, P., *et al. Astron. Astrophys.* **498**, 711 (2009).

[316] Levesque, E. M., *et al. Mon. Not. R. Astron. Soc.* **401**, 963 (2010).

[317] Rau, A., McBreen, S., Kruehler, T., Greiner, J. *GCN Circ.* **9353**, 1 (2009).

[318] McBreen, S., *et al. Astron. Astrophys.* **516**, 71 (2010).

[319] Palmer, D. *et al. GCN Circ.* **5076**, 1 (2006).

[320] Hullinger, D., *et al. GCN Circ.* **5142**, 1 (2006).

[321] Fong, W., Berger, E., Fox, D. B. *Astrophys. J.* **708**, 9 (2010).

[322] Leibler, C. N., Berger, E. *Astrophys. J.* **725**, 1202 (2010).

[323] Lazzati, D., Morsony, B. J., Begelman, M. C. *Astrophys. J.* **717**, 239 (2009).

[324] Panaitescu, A. arXiv:1005.1051 (2010).

VITA

Graduate College
University of Nevada, Las Vegas

Francisco Javier Virgili

Degrees:

Bachelor of Science, Astrophysics, 2004
Michigan State University

Master of Science, Physics, 2007
University of Nevada, Las Vegas

Special Honors and Awards:

Fall 2008-2009: NASA Nevada Space Grant Fellow

April 2008: UNLV Alumni Outstanding Thesis Award (both College and University level)

2007: Graduate Student and Professional Association Research Grant

Summer 2007: National Science Foundation East Asia and Pacific Summer Institutes Fellow (Advisor: Dr. Zuhui Fan, Peking University, China)

Spring 2007: NASAs Nevada Space Grant Fellow

Publications:

Racusin, J., Oates, S. R., Virgili, F. J., Wanderman, D. *Astrophys. J.* Submitted. (2011).

Virgili, F. J., Zhang, B., OBrien, P., Troja, E. *Astrophys. J.* **727**, 109 (2011).

Virgili, F. J., Zhang, B., OBrien, P., Troja, E. Accepted, *Italian Physical Society* (Conference proceedings from Venice 2009 conference) (2010).

Zhang, B., Zhang, B.-B., Virgili, F. J., et al. *Astrophys. J.* **703**, 1696 (2009).

Virgili, F. J., Zhang, B., OBrien, P., Troja, E. *AIPC.* 1133, 118 (2009).

Virgili, F. J., Liang, E. W., Zhang, B. *Mon. Not. R. Astron. Soc.* **392**, 91(2009).

Liang, E. W., Zhang, B., Virgili, F. J., Dai, Z. G. *Astrophys. J.* **662**, 1111 (2007).

Zhang, B., Liang, E. W., Gupta, N., Zhang B. B., Virgili, F. J., Dai, Z. G. *Philosophical Transactions of the Royal Society A: Mathematical and Engineering Sciences.* **365**, 1257 (2007).

Dissertation Title:

Gamma-ray Burst Populations

Dissertation Examination Committee:

Chairperson, Bing Zhang, Ph.D.
Committee Member, Stephen Lepp, Ph.D.
Committee Member, Kentaro Nagamine, Ph.D.
Graduate Faculty Representative, Balakrishnan Naduvalath, Ph.D.